# Search for MSSM Higgs decaying to tau pairs in $p\bar{p}$ collision at $\sqrt{s} = 1.96$ TeV at CDF

**by Dongwook Jang**

**A dissertation submitted to the**

**Graduate School—New Brunswick**

**Rutgers, The State University of New Jersey**

**in partial fulfillment of the requirements**

**for the degree of**

**Doctor of Philosophy**

**Graduate Program in Physics and Astronomy**

**Written under the direction of**

**Professor Amit Lath**

**and approved by**

_____

_____

_____

_____

_____

**New Brunswick, New Jersey**

**May, 2006**

© 2006

Dongwook Jang

ALL RIGHTS RESERVED

## ABSTRACT OF THE DISSERTATION

# Search for MSSM Higgs decaying to tau pairs in $p\bar{p}$ collision at $\sqrt{s} = 1.96$ TeV at CDF

**by Dongwook Jang**

**Dissertation Director: Professor Amit Lath**

This thesis presents the search for neutral Minimal Supersymmetric extension of Standard Model(MSSM) Higgs bosons decaying to tau pairs where one of the taus decays leptonically, and the other one hadronically. CDF Run II data with $\mathcal{L}_{int} = 310\, pb^{-1}$ are used. There is no evidence of MSSM Higgs existance, which results in the upper limits on $\sigma(p\bar{p} \rightarrow \phi) \times BR(\phi \rightarrow \tau\tau)$ in $m_A$ range between 115 and 250 GeV. These limits exclude some area in $\tan\beta$ vs. $m_A$ parameter space.

# Acknowledgements

I would like to first thank my advisor, Amit Lath. He guided me with the deep knowledge of particle physics and kept me on the right track with confidence.

Also I would like to thank Anton Anastassov who worked with me from the beginning of this analysis to the end and provided smart ideas, sophisticated methods.

I would like to give a credit to my previous advisor in Yonsei University, Youngjoon Kwon who showed me the beauty of particle physics world.

I deeply appreciate people directly involved in this analysis: John Conway who gave me valuable suggestions and provided me his fitting program, Zongru Wan who spent much time with conversation about ideas and techniques, Fedor Ratnikov who gave me various technical supports and helped me whenever I encountered problems.

I extend my gratitude to the following colleagues who gave me constant suggestions and encouragements: Tom Devlin, Terry Watts, Sunil Somalwar, John Zhou, Paul Di Turo, Jared Yamaoka, Sourabh Dube.

Many thanks should go to the members of Tau group, especially Alexei Safonov who made valuable comments on this analysis.

I would like to give my appreciation to the thesis committee members who reviewed my thesis carefully. I would also like to acknowledge the CDF collaboration and Fermilab that made this analysis possible.

It is great pleasure to me having such good friends, Sungmin Park, Kihyun Park, Yoonho Moon, Jangyeon Park, Seungsik Shin who encouraged me a lot.

Special thanks go to my family in Korea for their solid believing.

Finally I dedicate this thesis to my wife and son. Nothing is possible without them.

# Table of Contents

**Abstract** . . . . . ii

**Acknowledgements** . . . . . iii

**List of Tables** . . . . . vi

**List of Figures** . . . . . viii

**1. Introduction** . . . . . 1

1.1. The Higgs mechanism and Limitation of the Standard Model . . . . . 1

1.2. Supersymmetry and Minimal Supersymmetric SM . . . . . 5

**2. Experimental apparatus** . . . . . 12

2.1. Accelerators . . . . . 12

2.2. Collider Detector at Fermilab(CDF) . . . . . 14

2.2.1. Detector Coordinates . . . . . 16

2.2.2. Momentum measurement . . . . . 17

2.2.3. Energy measurement . . . . . 18

2.2.4. Muon detection . . . . . 21

2.3. Trigger and Data Acquisition . . . . . 24

**3. Event Selection** . . . . . 27

3.1. Event Topology . . . . . 27

3.2. Samples . . . . . 29

3.2.1. Data samples . . . . . 29

3.2.2. Signal Monte Carlo Samples . . . . . 31

3.2.3. Background Samples . . . . . 31

3.3. Particle identification . . . . . 32
3.3.1. Electrons . . . . . 32
3.3.2. Muons . . . . . 34
3.3.3. Taus . . . . . 36
3.4. Event cuts . . . . . 41
3.4.1. $\not\!\!E_T$ corrections . . . . . 41
3.4.2. Anti $Z \to ll$ cuts ($l = e, \mu$) . . . . . 42
3.4.3. QCD suppression cuts . . . . . 42
3.4.4. $\zeta$ cut . . . . . 43
3.4.5. Charge Requirements . . . . . 45

**4. Efficiency and Fake rate** . . . . . 47
4.1. Electron/Muon Efficiency . . . . . 48
4.2. Tau Efficiency and Fake rate . . . . . 49
4.2.1. Tau Efficiency . . . . . 50
4.2.2. $jet \to \tau$ Fake rate . . . . . 51

**5. Background Estimation** . . . . . 57
5.1. Background sources . . . . . 57
5.1.1. $Z \to \tau\tau$ . . . . . 57
5.1.2. $Z \to ee$, $Z \to \mu\mu$ . . . . . 58
5.1.3. Di-boson and $t\bar{t}$ . . . . . 58
5.1.4. Backgrounds with $jet \to \tau$ fakes . . . . . 58
5.2. Fake Rate Measurement and Consistency Checks . . . . . 60

**6. Systematic Uncertainty** . . . . . 69
6.1. Tau energy scale . . . . . 71
6.2. Parton distribution function . . . . . 74
6.3. XFT rescale . . . . . 78

**7. Observed Events** . . . . . 79

**8. Results & Interpretations** . . . . . 90

8.1. Results . . . . . 90

8.1.1. Likelihood . . . . . 91

8.1.2. Treatment of Systematic Errors . . . . . 92

8.1.3. Upper Limits on Higgs Cross section . . . . . 95

8.2. Interpretation of the Limits . . . . . 95

8.3. Conclusions . . . . . 100

**Appendix A. Glossary** . . . . . 103

**References** . . . . . 105

**Curriculum Vita** . . . . . 107

# List of Tables


1.1. Quark and leptons in the Standard Model. The quarks are denoted as: $u$—up, $d$—down, $c$—charm, $s$—strange, $t$—top, $b$—bottom. The leptons are denoted as: $e$—electron, $\mu$—muon, $\tau$—tau and their corresponding neutrinos. The numbers in the parentheses are electric charge (in units of proton charge) and mass or mass limit (in GeV). Each particle has its anti-particle, which has equal mass and equal physical properties but opposite charge. . . . . 2

1.2. Particles that carry forces in the Standard Model. The numbers in the parentheses are electric charge (in units of proton charge) and mass (in GeV). The gluon is responsible for mediating strong interaction between the quarks. . . . . 2

1.3. Chiral supermultiplets in the MSSM . . . . . 6

1.4. Gauge supermultiplets in MSSM . . . . . 7

2.1. *Run IIa performance.* . . . . . 14

2.2. *The design parameters of tracking systems.* . . . . . 19

2.3. *The characteristics of EM and HAD calorimeters.* . . . . . 22

2.4. *The characteristics of muon chambers.* . . . . . 25

3.1. *The tau decay branching fractions in terms of "leptonic" and "hadronic" category.* . . . . . 27

3.2. *Trigger efficiencies at plateau. The first three rows are for electron triggers. The fourth and fifth rows are for muon ($|\eta| < 0.6$) triggers. The sixth and seventh rows are for muon ($0.6|\eta| < 1$) triggers. The last two rows are for isolated track triggers which are targeted at taus.* . . . . . 30

3.3. Summary of electron cuts . . . . . 34

3.4. Summary of muon cuts . . . . . 36

3.5. *The top five most important topological final states of hadronic tau decays. $\mathcal{B}_i \equiv \mathcal{B}(\tau \to X_i \nu_\tau)$ are the tau branching fractions for the respective decay modes; $h^-$ stands for $\pi^-$ or $K^-$. Charge conjugate states are implied.* 36

3.6. Summary of tau cuts . . . . . 41

4.1. List of loose cuts for tau selection . . . . . 49

4.2. *Effect of individual cut on tau selection efficiency for $p_T > 15$ GeV, $E_T^{\tau\ cl} > 15$ GeV. Marginal efficiency is obtained by applying all cuts except the one interesting.* . . . . . 51

6.1. *Systematic uncertainties by source.* . . . . . 70

6.2. *Difference in acceptance between CTEQ5L and CTEQ6M (%).* . . . . . 76

7.1. *Predicted backgrounds and observed events in the $\tau_e\tau_h$ and $\tau_\mu\tau_h$ after applying all selection cuts.* . . . . . 89

7.2. *Predicted backgrounds and observed events in $\tau_e\tau_h + \tau_\mu\tau_h$ after applying all selection cuts.* . . . . . 89

8.1. *Upper limits at 95% CL on MSSM Higgs cross section times branching ratio to tau pairs as a function of Higgs mass.* . . . . . 97

8.2. *Production cross-sections (pb) for $b\bar{b} \to \phi$ and $gg \to \phi$ (no mixing scenario, $\tan\beta = 60$).* . . . . . 99

# List of Figures


1.1. Spontaneously broken Higgs potential. The minimum occurs not at zero but at $-\mu^2/(2\lambda)$. . . . . 3

1.2. *The fermions (a) and supersymmetric particles (b) contribution to the Higgs (mass)*$^2$ . . . . . 4

1.3. *Lowest order diagram contributing to* $gg \rightarrow \phi$ *and* $b\bar{b} \rightarrow \phi$. . . . . 8

1.4. *(a) shows the MSSM pseudo scalar Higgs production cross-sections in* $p\bar{p}$ *collision with* $\sqrt{s} = 2\ TeV$ *as a function of Higgs mass at* $tan\beta = 30$. *(b) shows the branching fraction of various MSSM pseudo scalar Higgs decays as a function of Higgs mass at* $tan\beta = 30$. . . . . 9

1.5. *The current understanding of MSSM parameters from LEP experiments. (a) shows constraints in* $tan\beta$ *vs.* $m_A$ *space with negative* $\mu$ *scenario. (b) shows exclusion in* $tan\beta$ *vs.* $m_A$ *space with positive* $\mu$ *scenario.* . . . 11

2.1. Delivered and stored luminosity as a function of store number(bottom axis) or year(top axis). The integrated luminosity shows rapidly increasing. 13

2.2. Fermilab accelerator chain. There are eight accelerators. They consist of linear accelerator and synchrotrons. . . . . 13

2.3. a quarter open view of CDF II detector. . . . . 15

2.4. an elevation view of CDF II detector. . . . . 16

2.5. CDF II tracking volume . . . . . 18

2.6. Silicon system . . . . . 20

2.7. COT superlayers . . . . . 20

2.8. The CES detectors are embedded in the EM calorimeters . . . . . 21

2.9. The strips and wires of the CES detector . . . . . 21

2.10. Muon coverage in $\eta$ and $\phi$ . . . . . 23

2.11. A matching example between a stub and a track . . . . . 24

2.12. Data flow of "deadtimeless" trigger and data acquisition . . . . . 26

3.1. *The event topology in this analysis. Higgs decays two taus. We look for the events that have a lepton from one tau and hadrons from another tau in the final states.* . . . . . 28

3.2. *Tau signal cone and isolation annulus for tracks and $\pi^0$'s.* . . . . . 38

3.3. *EM fraction vs. $E/P$ for MC $e$, $\mu$, and $\tau$. The $\xi$ ($\xi'$) cuts reject tau candidates above the respective lines.* . . . . . 40

3.4. *Effect of the $\tilde{H}_T$ cut on $Z$, $\phi(140)$, and QCD-dominated data sample. All distributions are normalized to unit area.* . . . . . 43

3.5. *Illustration of the definition of parameters used in the $\zeta$ cut.* . . . . . 44

3.6. *Effect of the $\zeta$ cut. (a) shows the acceptance of this cut on the signal $A \to \tau\tau$ MC. (b) shows the rejection of this cut against the $W$ background.* 46

4.1. *Comparison Fake rates from different samples with different trigger paths* 54

4.2. *The fake rate comparison among samples regardless of trigger paths.* . . 55

4.3. *Relative efficiency used in correction of QCD estimation.* . . . . . 56

4.4. *Relative fake rate used in QCD estimation* . . . . . 56

5.1. *Illustration of the control region to select $W + jet$ events in the $\zeta$ plane.* 62

5.2. *Consistency checks of jet $\to \tau$ fake predictions using the $\gamma + jet$ sample. The upper and lower bounds come from using the fake rates from the highest and second-highest $E_T$ jet in the event.* . . . . . 64

5.3. *Consistency checks of jet $\to \tau$ fake predictions using the non-isolated lepton sample. The upper and lower bounds come from using the fake rates from the highest and second-highest $E_T$ jet in the event.* . . . . . 65

5.4. *Consistency checks of jet $\to \tau$ fake predictions using region dominated by $W + jet(s)$. The upper and lower bounds come from using the fake rates from the highest and second-highest $E_T$ jet in the event.* . . . . . 66

5.5. *Consistency checks of jet $\rightarrow \tau$ fake predictions using $W \rightarrow l\nu$ MC sample for the same region used by the data $W + jet(s)$ (shown in Figure 5.4). The MC is not scaled to luminosity. The upper and lower bounds come from using the fake rates from the highest and second-highest $E_T$ jet in the event.* . . . . . 67

5.6. *Consistency checks of jet $\rightarrow \tau$ fake predictions using $W \rightarrow l\nu$ MC sample. The events pass* **all** *the event selection cuts (signal region). The MC is not scaled to luminosity. The upper and lower bounds come from using the fake rates from the highest and second-highest $E_T$ jet in the event.* . 68

6.1. *Efficiency of isolation requirements for data and MC vs number of primary vertexes in the event.* . . . . . 72

6.2. *Track multiplicity and $m(trks + \pi^0$'s) for tau candidates. Contributions from $W \rightarrow \tau\nu$ and various backgrounds are included as shown in the Legend.* . . . . . 73

6.3. *$p_T$ spectrum of taus from W decays.* . . . . . 74

6.4. *Kolmogorov-Smirnov tests of the observed tau $p_T$ spectrum and simulated shifts in the MC.* . . . . . 75

6.5. *Distributions of most probable shifts determined from 10k pseudo-experiments.* 76

6.6. *Acceptance variations comparing for the 41 CTEQ6 eigenvectors.The events are $A \rightarrow \tau\tau$ mass=140 GeV/$c^2$ with a $\tan\beta$ = 30. Bins 35,36 correspond to CTEQ6 eigenvectors $\pm$ 15, which control the gluon content.* 77

7.1. *Track multiplicity for tau candidates in the $\tau_\mu\tau_h$ and $\tau_e\tau_h$ channels.* . . . 80

7.2. *Seed track$p_T$ for tau candidates in the $\tau_\mu\tau_h$ and $\tau_e\tau_h$ channels.* . . . . . 81

7.3. *Hadronic system mass for tau candidates in the $\tau_\mu\tau_h$ and $\tau_e\tau_h$ channels.* 82

7.4. *Tau cluster energy for tau candidates in the $\tau_\mu\tau_h$ and $\tau_e\tau_h$ channels.* . . 83

7.5. *Transverse momentum of tau candidates in the $\tau_\mu\tau_h$ and $\tau_e\tau_h$ channels.* 84

7.6. *Transverse momentum of the lepton (e or $\mu$) candidates in the $\tau_\mu\tau_h$ and $\tau_e\tau_h$ channels.* . . . . . 85

7.7. *Missing transverse energy in the event in the $\tau_\mu\tau_h$ and $\tau_e\tau_h$ channels.* . . . 86

7.8. *$\tilde{H}_T$ in the $\tau_\mu\tau_h$ and $\tau_e\tau_h$ channels.* . . . . . 87

7.9. *$m_{vis}$ in the $\tau_\mu\tau_h$ and $\tau_e\tau_h$ channels.* . . . . . 88

8.1. *Visible mass distributions for Z and Higgs bosons (normalized to the same area).* . . . . . 91

8.2. *Acceptance for $\phi \to \tau\tau$* . . . . . 91

8.3. *Average shift in apparent Higgs cross section due to shifted templates, as a function of true Higgs cross section. This is the shift for a Higgs mass of 125 GeV/$c^2$ and shows that energy scale mismatches between data and MC could lead to a shift of 2 pb in the measured cross section. So if a 10 pb Higgs with mass 125 GeV/$c^2$ existed in our data, energy scale mismatches could cause us to measure a 12 pb cross section.* . . . . 94

8.4. *Example fit for $m_A$=140 GeV. Signal and all background contributions are set to levels corresponding to the 95% CL upper limit.* . . . . . 96

8.5. *Expected and observed limits for neutral MSSM Higgs production.* . . . . 97

8.6. $\tan\beta$ *vs $m_A$ exclusion contours for the no-mixing and $m_h^{max}$ scenarios with negative $\mu$ (a) and positive $\mu$ (b).* . . . . . 101

# Chapter 1

# Introduction

In this chapter, we discuss the motivation of Higgs particles in the Standard Model (SM) and their limitations. Then we extend our discussion to an extension, called Supersymmetry (SUSY). Even in SUSY models, there are many scenarios. We look at one of the simplest and most realistic ones, the Minimal Supersymmetric Standard Model (MSSM) and describe the Higgs sector in MSSM.

## 1.1 The Higgs mechanism and Limitation of the Standard Model

The Standard Model (SM) is a theory of fundamental particles and their interactions. It is the combination of electroweak theory (electromagnetic and weak interactions) and a theory of strong interactions. In the SM, fermions are responsible for matter while bosons are responsible for their interactions (forces). Fermions are particles with half integer spin and include 6 leptons, 6 quarks, and their anti-particles. Bosons are particles with integer spin and include the $\gamma, Z^0, W^{\pm}$, and 8 gluons. The photon ($\gamma$) is responsible for electromagnetic interactions. The $Z^0, W^{\pm}$ bosons are responsible for weak interactions. Gluons are responsible for the strong interactions (colored forces). Table 1.1, 1.2 shows the fundamental particles in the SM and their properties.

The SM is basically a gauge theory with $\mathrm{SU}(3)_C \times \mathrm{SU}(2)_L \times \mathrm{U}(1)_Y$. According to the gauge theory, all gauge bosons are massless, but in reality, the $W, Z$ bosons are massive. In order to give them mass while keeping the $\gamma$ and gluons massless, the Higgs mechanism was introduced [1]. It adds to the basic electroweak Lagrangian a doublet of scalar fields as Eq. 1.1.

$$\phi = \begin{pmatrix} \phi^+ \\ \phi^0 \end{pmatrix} \tag{1.1}$$

| Names | Family 1 | Family 2 | Family 3 |
|---|---|---|---|
| quarks | $u$ ($\frac{2}{3}$, 0.003)<br>$d$ ($-\frac{1}{3}$, 0.006) | $c$ ($\frac{2}{3}$, 1.3)<br>$s$ ($-\frac{1}{3}$, 0.1) | $t$ ($\frac{2}{3}$, 175)<br>$b$ ($-\frac{1}{3}$, 4.3) |
| leptons | $e$ ($-1$, 0.000511)<br>$\nu_e$ (0, $< 3 \times 10^{-9}$) | $\mu$ ($-1$, 0/106)<br>$\nu_\mu$ (0, $< 0.00019$) | $\tau$ ($-1$, 1.777)<br>$\nu_\tau$ (0, $< 0.0182$) |

Table 1.1: Quark and leptons in the Standard Model. The quarks are denoted as: $u$—up, $d$—down, $c$—charm, $s$—strange, $t$—top, $b$—bottom. The leptons are denoted as: $e$—electron, $\mu$—muon, $\tau$—tau and their corresponding neutrinos. The numbers in the parentheses are electric charge (in units of proton charge) and mass or mass limit (in GeV). Each particle has its anti-particle, which has equal mass and equal physical properties but opposite charge.

| bosons | charge | mass (GeV) |
|---|---|---|
| $\gamma$ | 0 | 0 |
| $W^\pm$ | $\pm 1$ | 80.4 |
| $Z$ | 0 | 90.187 |
| $g$ | 0 | 0 |

Table 1.2: Particles that carry forces in the Standard Model. The numbers in the parentheses are electric charge (in units of proton charge) and mass (in GeV). The gluon is responsible for mediating strong interaction between the quarks.

where $\phi^+$ and $\phi^0$ are complex fields defined as

$$\phi^+ = \frac{\phi_1 + i\phi_2}{\sqrt{2}} \tag{1.2}$$

$$\phi^0 = \frac{\phi_3 + i\phi_4}{\sqrt{2}} \tag{1.3}$$

Then the Lagrangian for the scalar field becomes

$$L_\phi = (D_\mu \phi)^\dagger (D^\mu \phi) - V(\phi) \tag{1.4}$$

and

$$D_\mu = \delta_\mu + igT^i W^i_\mu + \frac{i}{2} g' Y B_\mu \tag{1.5}$$

where $g, g'$ are gauge couplings related by $e = g \sin\theta_W = g' \cos\theta_W$. $T, Y$ are the SU(2), U(1) generators, respectively.

$$V(\phi) = \mu^2 \phi^\dagger \phi + \lambda (\phi^\dagger \phi)^2 \tag{1.6}$$

$$\phi^\dagger \phi = \phi^{+*}\phi^+ + \phi^{0*}\phi^0 = \frac{\phi_1^2 + \phi_2^2 + \phi_3^2 + \phi_4^2}{2} \tag{1.7}$$

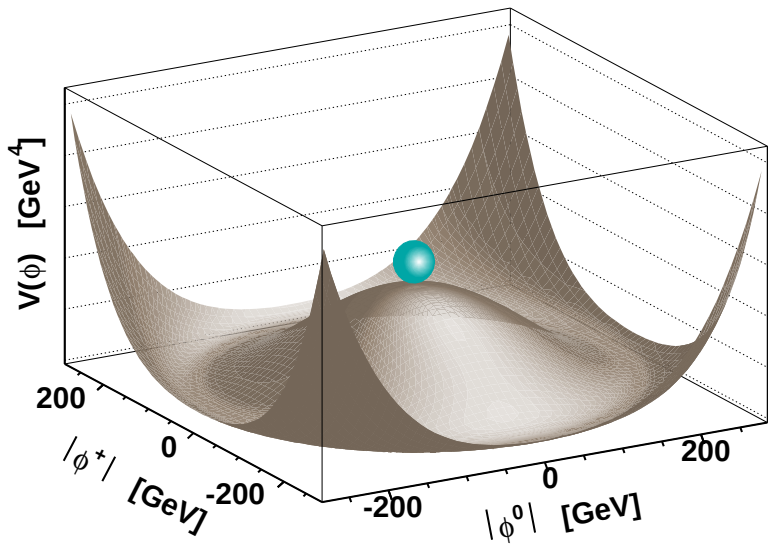


Figure 1.1: Spontaneously broken Higgs potential. The minimum occurs not at zero but at $-\mu^2/(2\lambda)$.

where $\mu$ and $\lambda$ are constants used in parametrization. The scalar potential $V(\phi)$ shown in Fig. 1.1 is invariant under the local gauge transformation.

$$\phi(x) \rightarrow \phi'(x) = e^{i\alpha^j(x)\tau^j/2}\phi(x) \tag{1.8}$$

where $\tau^j$ are the Pauli matrices and $\alpha^j$ are parameters. For $\lambda > 0$ and $\mu^2 < 0$, the minimum of $V(\phi)$ is not at zero, but at $\frac{-\mu^2}{2\lambda} \equiv \frac{v^2}{2}$. We can choose $\phi_3 = v$, $\phi_1 = \phi_2 = \phi_4 = 0$ without loosing generality. Now we can rewrite the scalar field as

$$\phi(x) = \frac{1}{\sqrt{2}}\begin{pmatrix} 0 \\ v + H(x) \end{pmatrix} \qquad with \;\; \phi_0 = \frac{1}{\sqrt{2}}\begin{pmatrix} 0 \\ v \end{pmatrix} \tag{1.9}$$

where $\phi_0$ is the vacuum expectation value of the field.

Now let's plug Eq. 1.9 into Eq. 1.4 and after doing some math, we can get

$$L_\phi = -\frac{1}{2}(2\lambda v^2)H^2 + (gv/2)^2 W_\mu^+ W_\mu^- + (v/2)^2(gW_\mu^3 - g'B_\mu)(gW^{3\mu} - g'B^\mu) + \cdots \tag{1.10}$$

and

$$W_\mu^\pm = \frac{1}{\sqrt{2}}(W_\mu^1 \mp W_\mu^2) \tag{1.11}$$

$$\begin{pmatrix} Z_\mu \\ A_\mu \end{pmatrix} = \begin{pmatrix} \cos\theta_W & -\sin\theta_W \\ \sin\theta_W & \cos\theta_W \end{pmatrix}\begin{pmatrix} W_\mu^3 \\ B_\mu \end{pmatrix} \tag{1.12}$$

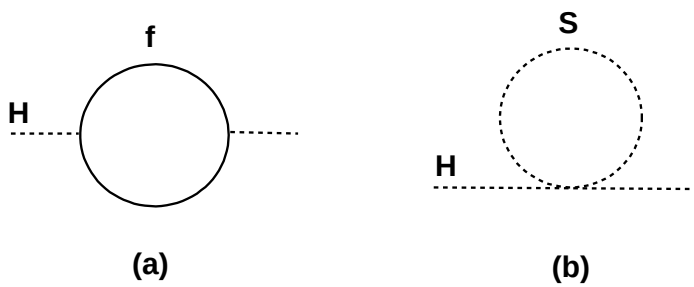


Figure 1.2: *The fermions (a) and supersymmetric particles (b) contribution to the Higgs (mass)*$^2$

where $\theta_W$ is the weak mixing angle. We can see that mass terms appear. If we don't consider higher order terms, we can determine each boson mass as

$$m_W = gv/2 \tag{1.13}$$

$$m_Z = gv/(2\cos\theta_W) \tag{1.14}$$

$$m_\gamma = 0 \tag{1.15}$$

with $m_H = v\sqrt{2\lambda}$. $v$ is about 246 GeV. So the only unknown parameter is $\lambda$ or $m_H$ which needs to be determined by experiment. The fermion masses are determined by Yukawa coupling terms.

There is no experimental result showing deviation from the SM so far. Many experimental results have confirmed every feature of the theory to a high precision. However, there are many unsolved issues. First, the SM doesn't incorporate gravity which is important at the Planck scale ($\sim 10^{19}$ GeV). Also the Higgs scalar field is very special, and is considered a fundamental field, but the model does not explain why this scalar field should have non zero vacuum expectation value (VEV).

When we consider the self-couplings in the Higgs field with fermionic loops shown in Fig 1.2a, the correction to the Higgs mass can be written as [4]

$$\Delta m_H^2 \sim \frac{|k_f|^2}{16\pi^2}[-2\Lambda_{UV}^2 + 6m_f^2 ln(\Lambda_{UV}/m_f) + \cdots] \tag{1.16}$$

where, $k_f$ is the coupling constant, and $\Lambda_{UV}$, the ultraviolet cutoff which might be

considered as the energy scale at which new physics occurs and keeps the integral convergent. If one would include a theory of gravity at the Planck scale, Eq. 1.16 becomes very large compared to the expected Higgs mass scale. There is a reason to believe that the Higgs mass is not larger than the order of 1 TeV[2]. If $\Lambda$ is really of the order of the Planck scale, then the correction should compensate for the huge contribution of the radiative correction term in a way that the Higgs mass stays around 1 TeV. This compensation should be very precise in order to cancel higher orders in perturbation theory. This fine-tuning cancellation is considered unnatural. This is known as "fine tuning problem". Also, electroweak symmetry breaking occurs at low energy ($\sim 10^2$ GeV) which is many orders below the Planck scale. There is no easy way to explain this "hierarchy problem". Due to these problems, we do not consider the SM to be the theory of everything. At most it is a low energy effective theory. We need a new theory or an extension of the SM. There is a most attractive theory that can solve many of the above problems in an elegant way, called Supersymmetry (SUSY).

## 1.2 Supersymmetry and Minimal Supersymmetric SM

SUSY is motivated by a hope of unifying strong and electroweak forces with gravity and a further hope that the Higgs mechanism can be derived without any postulates. Additionally, the theory provides a good candidate of dark matter: the Lightest Supersymmetric Particle (LSP). However, there is no experimental evidence as yet supporting SUSY.

Supersymmetry is basically a symmetry of fermions and bosons. The basic postulate is the existence of operators which change fermions into bosons or vice versa,

$$Q|boson>=|fermion>, \qquad Q^{\dagger}|fermion>=|boson> \tag{1.17}$$

The operator Q leaves all quantum numbers unchanged except for spin. Every fermion and boson has a partner satisfying Eq. 1.17. Supersymmetric partners are denoted by a "$\sim$" on top of letters. For example, the super partner of the down quark(u) is $\widetilde{u}$. The supersymmetric partners of gauge bosons are named by attaching -ino and s- for the bosons and fermions respectively. For example, the supersymmetric partner of the

| Names | | spin 0 | spin 1/2 |
|---|---|---|---|
| squarks, quarks | Q | $(\widetilde{u}_L \widetilde{d}_L)$ | $(u_L d_L)$ |
| ($\times$3 families) | $\bar{u}$ | $\widetilde{u}_R^*$ | $u_R^\dagger$ |
| | $\bar{d}$ | $\widetilde{d}_R^*$ | $d_R^\dagger$ |
| sleptions, leptons | L | $(\widetilde{\nu}\widetilde{e}_L)$ | $(\nu e_L)$ |
| ($\times$3 families) | $\bar{e}$ | $\widetilde{e}_R^*$ | $e_R^\dagger$ |
| Higgs, higgsinos | $H_u$ | $(H_u^+ H_u^0)$ | $(\widetilde{H}_u^+ \widetilde{H}_u^0)$ |
| | $H_d$ | $(H_u^0 H_u^-)$ | $(\widetilde{H}_u^0 \widetilde{H}_u^-)$ |

Table 1.3: Chiral supermultiplets in the MSSM

electron is the selectron, and that of the photon is the photino. If we consider the radiative Higgs mass correction as in Eq. 1.16, the effect of the super partners shown in Fig. 1.2b should be also added to the correction such that the supersymmetric part of corrections can be written as

$$\Delta m^2_{H,\mathrm{SUSY}} \sim \frac{|k_S|^2}{16\pi^2}[\Lambda^2_{UV} + 2m_S^2 ln(\Lambda_{UV}/m_S) + \cdots] \tag{1.18}$$

where the subscript $S$ stands for the supterpartner so that $k_S = |k_f|^2$ and $m_S = m_f$. The relative sign of $\Lambda_{UV}$ quadratic terms in Eq. 1.16 and Eq. 1.18 are opposite. If each of fermions in the SM is accompanied by two complex scalars (superpartners), the contributions from $\Lambda^2_{UV}$ will cancel. This shows the power of SUSY that the hierarchy problem in the SM is resolved without fine tuning.

Among the many extensions of the SM, the one which adds the least number of model parameters is called the Minimal Supersymmetric SM (MSSM). The minimum particle content required in MSSM is listed in Table 1.3, and 1.4. Note that there are two Higgs doublets while the SM requires only one. This is the minimal Higgs structure needed for an anomaly-free theory. None of these particles have been observed in experiments yet.

If we introduce a Higgs potential with non-zero vacuum expectation values(VEV) analogous to spontaneous symmetry breaking in electroweak theory, we can write down the components of the Higgs field as shown in Eq. 1.19 at tree level.

| Names | spin 1/2 | spin 1 |
|---|---|---|
| gluino, gluon | $\widetilde{g}$ | g |
| winos, W bosons | $\widetilde{W}^{\pm}\widetilde{W}^{0}$ | $W^{\pm}W^{0}$ |
| bino, B boson | $\widetilde{B}^{0}$ | $B^{0}$ |

Table 1.4: Gauge supermultiplets in MSSM

$$< \phi_1 >= \frac{1}{\sqrt{2}} \begin{pmatrix} v_1 \\ 0 \end{pmatrix}, \qquad < \phi_2 >= \frac{1}{\sqrt{2}} \begin{pmatrix} 0 \\ v_2 \end{pmatrix} \tag{1.19}$$

where $v_i$ is the minimum in Higgs potential which satisfies Eq. 1.20. In this parameterization, $v_1(v_2)$ controls the coupling to down(up) type quarks.

$$v^2 = v_1^2 \ + \ v_2^2 = \frac{4M_W^2}{g^2} = (246\ GeV)^2 \tag{1.20}$$

Now we can define a convenient and common parameter, $tan\beta$.

$$tan\beta = \frac{v_2}{v_1} \tag{1.21}$$

The two doublet Higgs sector contains eight scalar degrees of freedom. Spontaneous symmetry breaking generates three Goldstone bosons which become the longitudinal components of the $W^{\pm}, Z$. So the remaining five degrees of freedom become the physical Higgs particles: two $CP$-even neutrals($h^0, H^0$), one $CP$-odd neutral $A^0$,two charged $H^{\pm}$.

Two $CP$-even neutrals($h^0, H^0$) are shown in Eq. 1.22 which are obtained from the real part of the mass matrix.

$$\begin{pmatrix} h^0 \\ H^0 \end{pmatrix} = \sqrt{2} \begin{pmatrix} cos\alpha & sin\alpha \\ -sin\alpha & cos\alpha \end{pmatrix} \begin{pmatrix} Re\phi_1^{0*} - v_1 \\ Re\phi_2^{0*} - v_2 \end{pmatrix} \tag{1.22}$$

where $\alpha$ is the mixing angle.

One $CP$-odd neutral($A^0$) is shown in Eq. 1.23 which is obtained from the imaginary part.

$$A^0 = \sqrt{2}(-Im\phi_1^{0*}sin\beta + Im\phi_2^{0*}cos\beta \tag{1.23}$$

The two charged Higgs states are

$$H^{\pm} = -\phi_1^{\pm} sin\beta + \phi_2^{\pm} cos\beta \tag{1.24}$$

We have six free parameters: the four Higgs masses[1], $\tan\beta$, and $\alpha$. At the tree level, these parameters can be reduced to two, $m_A, tan\beta$. The others can be derived from Eq. 1.25, 1.26, 1.27.

$$m_{H^{\pm}}^2 = m_{A^0}^2 + m_W^2 \tag{1.25}$$

$$m_{h^0,H^0}^2 = \frac{1}{2}\left[m_{A^0}^2 + m_Z^2 \pm \sqrt{(m_{A^0}^2 + m_Z^2)^2 - 4m_Z^2 m_{A^0}^2 cos^2 2\beta}\right] \tag{1.26}$$

$$tan2\alpha = tan2\beta \left(\frac{m_{A^0}^2 + m_Z^2}{m_{A^0}^2 - m_Z^2}\right) \tag{1.27}$$

At hadron colliders the production cross-section for $A$ and either $h$ or $H$ is enhanced by $\sim \tan^2\beta$ compared to the SM. The remaining $CP$-even Higgs has SM-like couplings. We are going to concentrate on scenarios with large $\tan\beta$ ($\tan\beta > 20$). These are the relevant scenarios for the currently available data samples at the Tevatron.

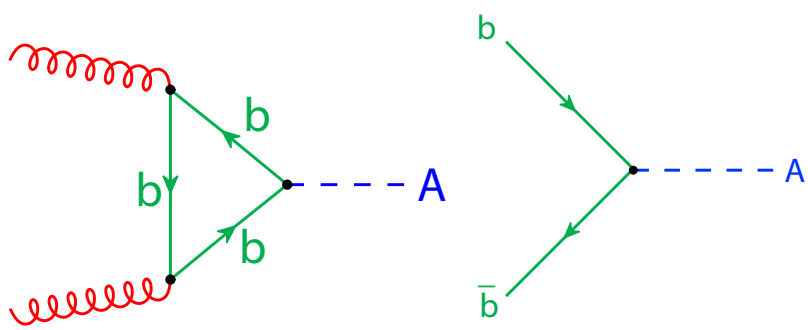


(a) Gluon fusion (b) Quark annihilation

Figure 1.3: *Lowest order diagram contributing to $gg \to \phi$ and $b\bar{b} \to \phi$.*

The dominant production mechanisms for neutral MSSM Higgs bosons at hadronic colliders are gluon fusion ($gg \to \phi$) and quark anti-quark annihilation ($q\bar{q} \to \phi$). The

[1]There are five Higgses, but the positive and negative charged Higgs have same mass.

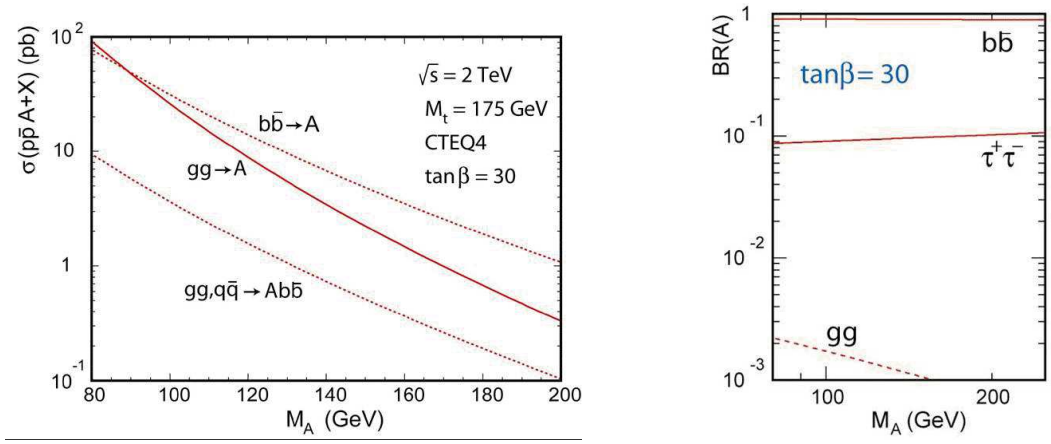


(a) Cross section of Higgs production

(b) Branching fraction of Higgs decays

Figure 1.4: *(a) shows the MSSM pseudo scalar Higgs production cross-sections in $p\bar{p}$ collision with $\sqrt{s} = 2\ TeV$ as a function of Higgs mass at $tan\beta = 30$. (b) shows the branching fraction of various MSSM pseudo scalar Higgs decays as a function of Higgs mass at $tan\beta = 30$.*

Feynman diagram for the former is shown in Figure 1.3(a). It is the same as the corresponding diagram in the SM, except for the replacement of $t \to b$ in the loop. The Higgs coupling to *down*-type quarks is proportional to $\tan\beta$ and the $b$-quark loop dominates the cross section despite the $m_b/m_t$ suppression factor. The quark annihilation is dominated by $b\bar{b} \to \phi$ shown in Figure 1.3(b). The cross section for the Higgs production in $p\bar{p}$ collision is shown in Figure 1.4.

There are higher order diagrams leading to the presence of one or two *observable* $b$-quarks in the final state. These are especially important for Higgs searches relying on the detection of three or four $b$-jets. In this analysis we do not require observation of associated $b$-quarks and therefore, do not consider each of these higher-order diagrams separately. More information on MSSM Higgs production can be found in [3].

The decays of the neutral MSSM Higgs bosons are governed by the couplings to *up*- and *down*-type particles through the $\tan\beta$ and $m_A$ parameters. The dominant decay modes are $\phi \to b\bar{b}$ and $\phi \to \tau^+\tau^-$ with branching fractions $\mathcal{B}(\phi \to b\bar{b}) \sim 90\%$ and $\mathcal{B}(\phi \to \tau^+\tau^-) \sim 8\%$ [2]. Figure 1.4 shows the branching fraction of some decays. Consequently, these are the relevant decay modes for neutral MSSM Higgs searches.

[2] We do not consider "bosophilic" Higgs scenarios.

Despite the large advantage in branching fraction of the $b\bar{b}$ mode, the $\tau\tau$ channel is still relevant. Due to large di-jet backgrounds the gluon fusion mechanism can not be probed using the $b\bar{b}$ channel (given the current state of di-jet mass resolution). One is then restricted to Higgs production in association with sufficiently high-$p_T$ $b$ quarks leading to considerable efficiency losses. On the other hand, the $\tau\tau$ mode allows the exploration of Higgs production through both gluon fusion and quark anti-quark annihilation The dominant background in this case is from $Z/\gamma^* \to \tau\tau$ events. This process is well modeled and has reliably measured cross-section from the $Z \to ee$, $Z \to \mu\mu$ channels, eliminating uncertainties in background normalization. This makes the $b\bar{b}$ and $\tau\tau$ channels equally useful tools for the searches. There was an attempt at the $\tau\tau$ channel in Run I [5], which however did not attain the sensitivity of this analysis.

In the search for the MSSM Higgs boson, there are two benchmark scenarios used at LEP and we are going to use these as well, which are $m_h^{max}$ and no-mixing. These scenarios were designed for the searches of the MSSM Higgs sector without assuming any soft SUSY breaking scenario. The parameters used in this scenario are the top quark mass, $m_t$; the gluino mass, $m_{\tilde{g}}$; the U(1) gaugino mass parameter, $M_2$; the soft SUSY breaking parameter, $M_{SUSY}$; $X_t \equiv A_t - \mu/\tan\beta$, $X_b \equiv A_b - \mu/\tan\beta$ where $A_t$, $A_b$ are the trilinear Higgs sfermion couplings and $\mu$ is the Higgs mixing parameter. The $m_h^{max}$ scenario intended to keep conservative $\tan\beta$ exclusion bounds. This scenario chose the parameters such that the maximum possible Higgs boson mass as a function of $\tan\beta$ is obtained. The no-mixing scenario is the same as the $m_h^{max}$ scenario, but assuming no mixing in the $\tilde{t}$ sector and the parameters are chosen to get a higher SUSY mass scale to avoid the LEP Higgs bounds. More information on benchmark scenarios can be found in [26]. The present constraints from LEP experiment on the MSSM parameters are shown in Fig. 1.5.

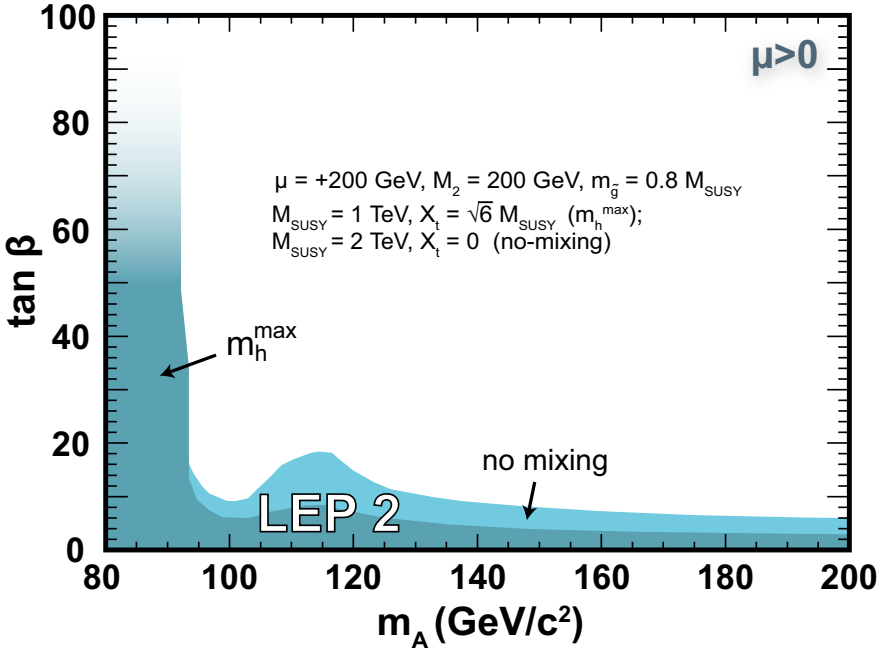


(a) negative $\mu$

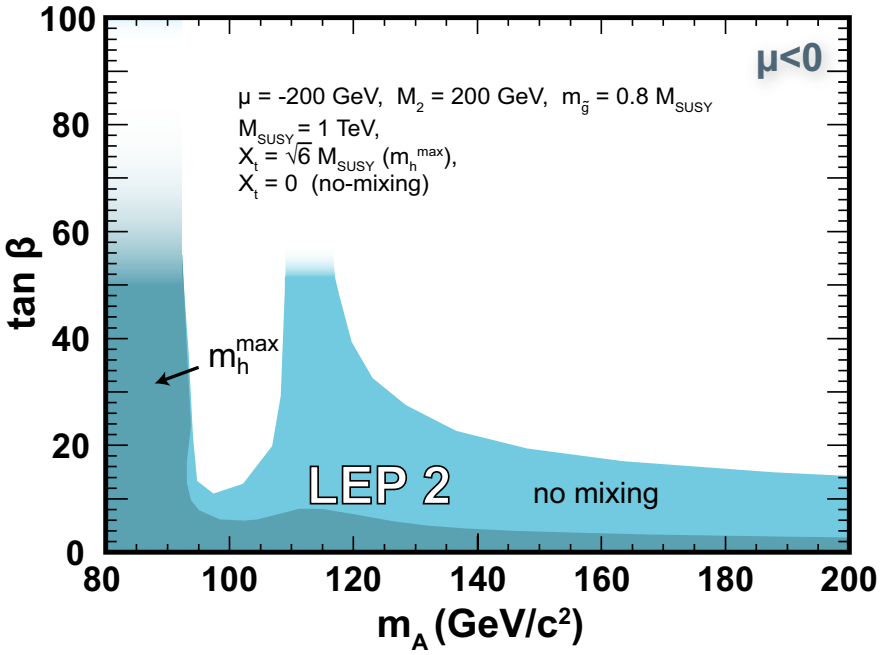


(b) positive $\mu$

Figure 1.5: *The current understanding of MSSM parameters from LEP experiments. (a) shows constraints in tan$\beta$ vs. $m_A$ space with negative $\mu$ scenario. (b) shows exclusion in tan$\beta$ vs. $m_A$ space with positive $\mu$ scenario.*

# Chapter 2

# Experimental apparatus

The experimental apparatus for this Higgs search consists of two components: the accelerator complex, and the detector. Accelerators create particle beams (protons and antiprotons in our case), propel them at high energies, and collide them at specific locations where we situate our detectors. These collisions generate several daughter particles which can then be observed and recorded by detectors. The collision rate is determined by the instantaneous luminosity($\mathcal{L}$) such as

$$\mathcal{L} = \frac{f_r n_{bunch} N_p N_{\bar{p}}}{A}$$

where $f_r$ is the bunch crossing rate, $n_{bunch}$ is the number of bunches of colliding particles, $N_p(N_{\bar{p}})$ is the number of protons (antiprotons), and A is the effective cross sectional area of the beam overlap. The collected data are often expressed by the integrated luminosity which is defined as $\int \mathcal{L} dt$ which for this analysis is 310 $pb^{-1}$. One can simply obtain the number of events($N$) expected from a process by the following relation.

$$N = \sigma \int \mathcal{L} dt$$

where, $\sigma$ is the total cross section for a given process.

## 2.1 Accelerators

There are two kinds of basic accelerators, linear and circular. Fermilab has both. The basic idea of accelerating particles is that a charged particle feels a force under an electric and/or magnetic field. Fermilab accelerators are complex combinations of devices which generate electric or magnetic fields. Fig. 2.2 shows the Fermilab accelerator chain with eight accelerators.

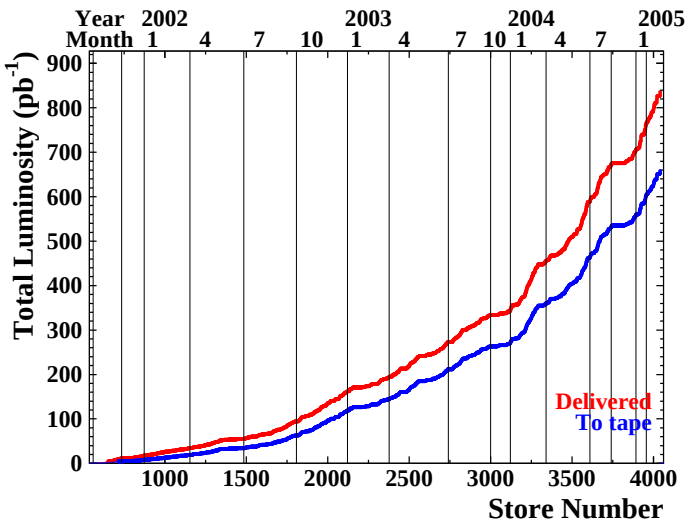


Figure 2.1: Delivered and stored luminosity as a function of store number(bottom axis) or year(top axis). The integrated luminosity shows rapidly increasing.

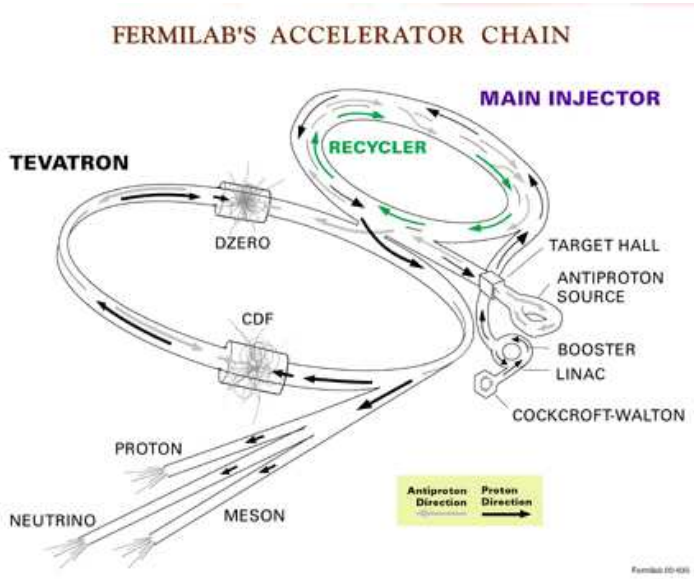


Figure 2.2: Fermilab accelerator chain. There are eight accelerators. They consist of linear accelerator and synchrotrons.

| | |
|---|---|
| Center of mass energy | 1.96 GeV |
| Instantaneous luminosity | 0.1-0.8 $\times$ $10^{32}$ |
| Number of bunches | 36$\times$36 |
| Bunch length | 0.37m |
| Bunch spacing | 396 ns |
| Protons per bunch | $2.7\times10^{11}$ |
| Anti-protons per bunch | $3.0\times10^{10}$ |
| Total anti-protons | $1.1\times10^{12}$ |
| Anti-proton production rate | $1.0\times10^{11} hr^{-1}$ |

Table 2.1: *Run IIa performance.*

The accelerator chain starts with a Cockcroft-Walton accelerator, a 750 kV DC voltage source which accelerates protons. The protons are then injected into a linear accelerator (the Linac) where proton beams are accelerated to 400 MeV. The first synchrotron in the Fermilab accelerator chain, the Booster, then accelerates the proton beams to 8 GeV and injects them into a larger synchrotron, the Main Injector. Booster protons also create antiprotons by hitting a nickel target. The antiprotons created by the collision are collected and injected into a small synchrotron called the Debuncher to reduce the beam spread and collected in another synchrotron called the Accumulator before being inserted into the Main Injector. The Main Injector accelerates the protons and antiprotons from 8 GeV to 120 GeV (150 GeV for antiprotons) and inserts them into the Tevatron, the world's first superconducting synchrotron. The circumference of the Tevatron ring is about 4 miles and the magnetic field is about 4.2 Tesla. Protons(antiprotons) are accelerated here to 980 GeV before being brought into collision.

Table 2.1 summarizes the performance of RunIIa accelerator.

## 2.2 Collider Detector at Fermilab(CDF)

The basic function of particle detectors is to measure the momentum and energy of the collision products. If we know the momentum and energy of the particles, then we can form their four momentum. This is the final goal of the detectors. A particle generates electric signal in detectors. The electric signal is converted to human readable form such as digital numbers. We can divide the CDF detectors into the following

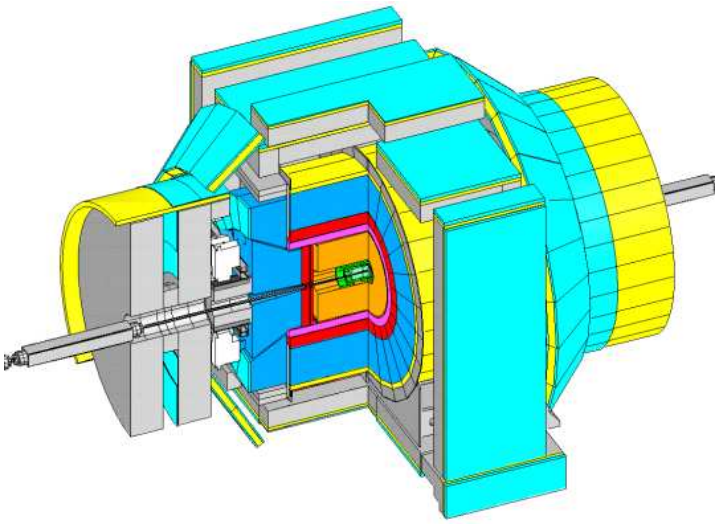

Figure 2.3: a quarter open view of CDF II detector.

functional categories: momentum measurement, energy measurement, muon detection, and luminosity measurement.

Momentum measurement is performed by the Silicon VerteX detector (SVX), Central Outer Tracker (COT), and Solenoid. The energy measurement is done by the Central ElectroMagnetic calorimeter (CEM), Central HAdronic calorimeter (CHA), endWall HAdronic calorimeter (WHA), Plug ElectroMagnetic calorimeter (PEM), and Plug HAdronic calorimeter (PHA). Muons need some special treatment because they leave hits in SVX and COT, but penetrate the calorimeters. Hence, we need some detectors outside of the calorimeters to catch muons. This is done by the following detectors: Central MUon detector (CMU), Central Muon uPgrade detector (CMP), Central Scintillation counter uPgrade (CSP), Central Muon eXtension detector (CMX), and Central Scintillation counter eXtension (CSX). There are some auxiliary detectors to help measure the radiation of charged particles or to identify photons in the calorimeters, which are Central Preshower Radiate detector (CPR), Central Electromagnetic Showermax detector (CES), and Plug Electromagnetic Showermax detector (PES). There also is the Cherenkov Luminosity Counter (CLC) which measures luminosity precisely.

In the following subsections, we discuss the above detectors in detail. We use the word "central" which means the region $|\eta| < 1$ in the detectors. This is particularly

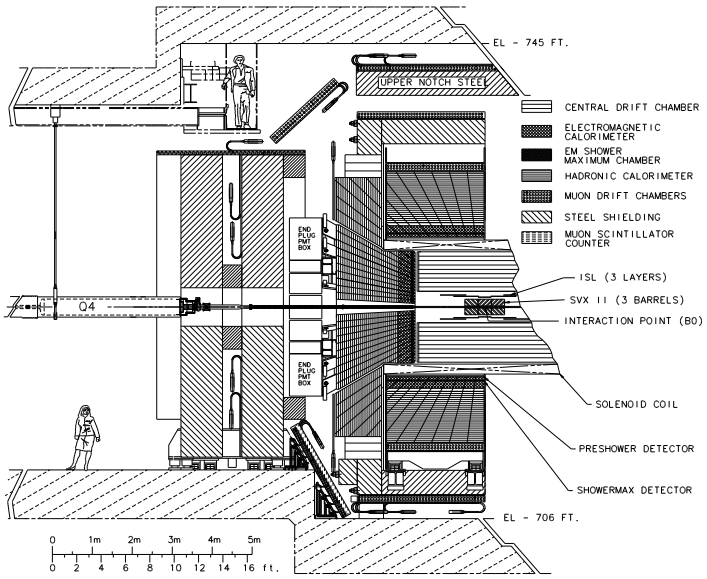


Figure 2.4: an elevation view of CDF II detector.

important because we have good calibrations on the detectors in this region, and this analysis corresponds to this region primarily.

### 2.2.1 Detector Coordinates

Due to the fact that the collisions occur along the beam line, the detector is designed as a cylindrical coordinate system. The origin of the coordinate is the center of the detector. The incoming proton direction is defined as the positive z axis. The upward direction is the positive y axis and the x axis is determined by the right-hand coordinate system which is the horizontal direction pointing out from the center of the ring. The polar angle($\theta$) can be expressed as the pseudo-rapidity($\eta$). Eq. 2.1 shows the relation between them.

$$\eta = -ln \tan \frac{\theta}{2} \quad or \quad \sinh \eta = \cot \theta \tag{2.1}$$

Many particles from the underlying event occur along the beam line from processes such as spectator quarks, beam halo, and initial radiation. For those particles, the transverse energies and momenta are small and are not very interesting to us. Hence, the

transverse components of an event are important at CDF. The transverse momentum, $p_T$ and the transverse energy, $E_T$ are defined as follows.

$$p_T \equiv p \sin\theta \tag{2.2}$$

$$E_T \equiv E \sin\theta \tag{2.3}$$

where $p$ is the magnitude of the momentum, $E$ is the energy, and $\theta$ is the angle between the positive z axis and the direction of a particle object.

### 2.2.2 Momentum measurement

A superconductor solenoid surrounds the COT and generates a 1.4 Tesla magnetic field. Charged particle trajectories are bent by the force due to the magnetic field. The COT is the main part of the tracking system and measures the momentum of charged particles based on the curvature. The COT extends from 44cm to 132cm in radius and $\pm 1$ in $\eta$. It is composed of 8 superlayers filled with Ar-Et(50:50) gas and with a drift velocity of about 200 $\mu$m/ns. Four layers out of 8 are tilted by 30° to the radial direction and are called "stereo" type superlayers. The regular ones are called "axial" superlayers. Each superlayer consists of 12 layers of sense wires so that a maximum of 96 measurements can be used to reconstruct tracks and measure their momenta. The COT is designed to measure momentum as low as 400 MeV/c. The momentum resolution depends on the momentum and is $\delta p_T/p_T^2 < 0.1\%/\text{GeV/c}$ when combined with the SVX which will be discussed in the next paragraph. So if we have 10 GeV measurement, the uncertainty of the measurement is $\pm 0.1$ GeV.

The innermost detector (SVX) provide additional information for tracking, curvature interpolations, and secondary vertices. It consists of Layer00, the Silicon VerteX detector II(SVX II), and the Intermediate Silicon Layer(ISL). Layer00 is the innermost detector. It is a single-sided silicon layer mounted on the beam pipe. SVX II consists of 5 double-sided silicon layers where one side is "axial" and the other "stereo". The axial side is used for $r$-$\phi$ measurements and the stereo is used for $r$-$z$ measurements. The ISL is placed just outside of the SVX II and has 2 double-sided silicon layers.

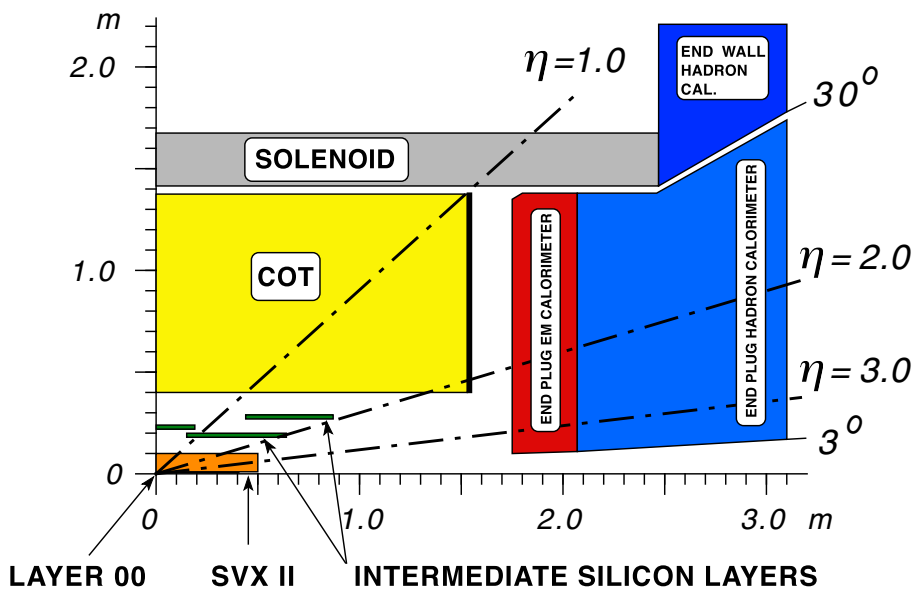


Figure 2.5: CDF II tracking volume.

The resolution of the impact parameter of SVX II + ISL is 40 $\mu$m including a 30 $\mu$m contribution from the beamline. The $z_0$ resolution of SVX II + ISL is 70 $\mu$m.

Table 2.2 summarizes the design parameters of the tracking systems.

### 2.2.3 Energy measurement

When an electron traverses material, it radiates a photon, which creates an electron-positron pair. Each particle of the pair in turn radiates photons. This showering process continues until the energy loss due to ionization exceeds the threshold of the pair production mechanism. This is called an EM shower. Photons from the EM shower are collected by Photo-Multiplier Tubes(PMT) and are used to determine the energy of the original electron.

The longitudinal size of the shower grows only logarithmically with energy. A very useful cascade parameter is the radiation length $X_0$, which is the mean distance for the $e^{\pm}$ to lose all but 1/e of its energy. For example, for a 10 GeV electron in lead glass, the maximum electromagnetic shower is at about $6X_0$ and the 95% containment depth is at about $16X_0$. Hadrons lose energy by nuclear interaction cascades which can have

| COT | |
|---|---|
| Number of superlayers | 8 |
| Radial coverage | 44-132cm |
| $\eta$ coverage | $\|\eta\| \leq 1.0$ |
| Number of channels | 30,240 |
| Resolution per measurement | 180 $\mu$m |
| Measurements per superlayers | 12 |
| Maximum drift distance | 0.88 cm |

| ISL | |
|---|---|
| Number of superlayers | 1 for $\|\eta\| \leq 1.0$ |
| | 2 for $1.0 \leq \|\eta\| \leq 2.0$ |
| Radial coverage | 20-28cm |
| $\eta$ coverage | $\|\eta\| \leq 1.9$ |
| Number of channels | 268,800 |
| Resolution per measurement | 16 $\mu$m |

| SVXII | |
|---|---|
| Number of superlayers | 5 |
| Radial coverage | 2.4-10.7cm |
| $\eta$ coverage | $\|\eta\| \leq 2.0$ |
| Number of channels | 405,504 |
| Resolution per measurement | 12 $\mu$m |

Table 2.2: *The design parameters of tracking systems.*

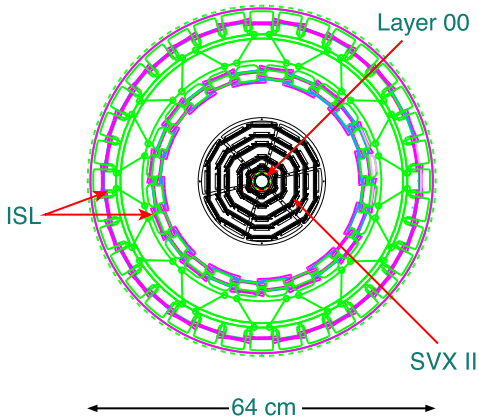


Figure 2.6: Silicon system.

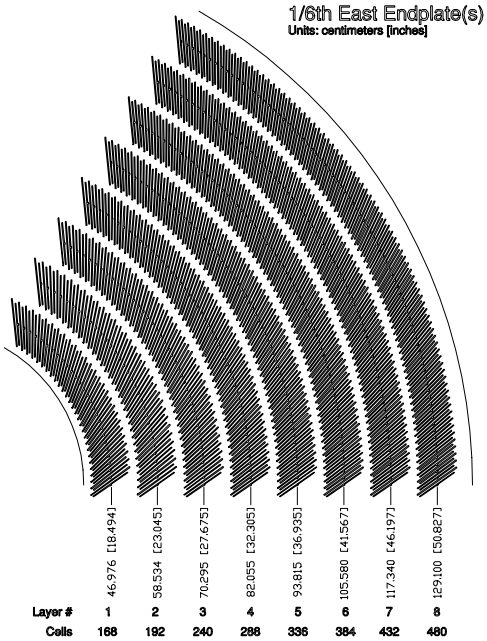


Figure 2.7: COT superlayers.

charged pions, protons, kaons, neutrons, neutral pions, neutrinos, soft photons, muons, etc. It is much more complicated than an electromagnetic cascade and thus results in a large fluctuation in energy measurement. In analogy to $X_0$, a hadronic interaction length $\lambda$ can be defined. Hadronic showers are much longer than the electromagnetic ones.

Central calorimeters(CEM and CHA) are segmented by 24 wedges(15° each) in $\phi$ and 10 towers($\sim 0.1$) over $|\eta| \lesssim 1.1$. Plug calorimeters(PEM and PHA) are segmented by 48 wedges(7.5° each) and 8 towers($\sim 0.1$) over $1.1 \lesssim |\eta| \lesssim 1.8$, and 24 wedges(15° each) and 4 towers($\sim 0.2$) over $2.1 \lesssim |\eta| \lesssim 3.6$. Endwall hadronic calorimeters (WHA) are located between the central and the plug hadronic calorimeters. The resolution of the EM calorimeter depends on the transverse energy and is $\delta E_T/\sqrt{E_T} < 14\% \cdot GeV^{1/2}$. Hence if we have 100 GeV measurement, its uncertainty is 1.4 GeV. The resolution of the HAD calorimeter is worse than that of the EM and it is $\delta E_T/\sqrt{E_T} < 75\% \cdot GeV^{1/2}$.

In addition to the calorimeters, there are showermax detectors to measure the position of EM showers. These consist of CES, CPR in the central region and PES in the plug region. The CES is a multi-wire(strip/wire) proportional chamber embedded

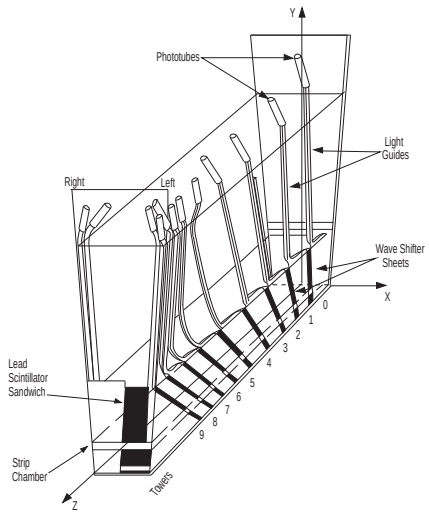


Figure 2.8: The CES detectors are embedded in the EM calorimeters

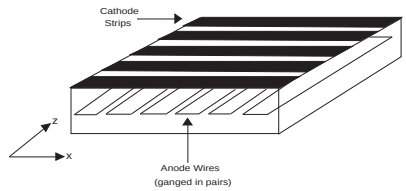


Figure 2.9: The strips and wires of the CES detector

approximately $6X_0$ in the CEM. The strip detector is perpendicular to the beamline and used to measure the z position of the shower. The wire detector is parallel to the beamline and used to measure the x position of the shower. Figure 2.8 illustrates the CES detector inside of the calorimeters and Figure **??** shows the strips and wires of the CES. The CPR is a preshower detector placed in front of the CEM. The PES is composed of two scintillator layers(called U and V) and embedded at approximately $X_0$ in the PEM. The U and V layers are aligned at $+22.5°$ and $-22.5°$ to the radial direction to provide two dimensional position measurement.

Table 2.3 shows the characteristics of EM and HAD calorimeters.

### 2.2.4 Muon detection

Muons are minimum ionizing particles(MIP) and deposit very little energy in calorimeters. Muon detectors are located just outside of calorimeters. The muon detectors consist of four systems of scintillators and proportional chambers in the region with $|\eta| \lesssim 2.0$. The magnet return yoke and additional steel walls are used to stop particles other than muons. Muons decay but they are considered stable in CDF detector because of their long lifetime.

| | Central and Endwall | Plug |
|---|---|---|
| EM | | |
| Thickness | $19X_0, 1\lambda$ | $21X_0, 1\lambda$ |
| Sample(Pb) | $0.6X_0$ | $0.8X_0$ |
| Sample(scintillator) | 5 mm | 4.5 mm |
| Sampling resolution | $11.6\%/\sqrt{E_T}$ | $14.0\%/\sqrt{E_T}$ |
| Stochastic resolution | $14.0\%/\sqrt{E_T}$ | $16.0\%/\sqrt{E_T}$ |
| HAD | | |
| Thickness | $4.5\lambda$ | $1\lambda$ |
| Sample(Pb) | 1 inch (central)<br>2 inch (endwall) | 2 inch |
| Sample(scintillator) | 10 mm | 6 mm |
| energy resolution | $75\%/\sqrt{E_T}$ | $80\%/\sqrt{E_T}$ |

Table 2.3: *The characteristics of EM and HAD calorimeters.*

The muon detection system consists of the Central MUon detector(CMU), the Central Muon uPgrade(CMP), the Central Muon eXtension(CMX), and the Intermediate MUon detector(IMU). Fig. 2.10 shows the coverage of each detector in $\eta - \phi$ space.

The CMU is a stacked array of single-wired drift tubes composed of 144 modules with 16 rectangular cells per modules and placed on just outside of the hadronic calorimeters(CHA).

The CMP is located behind an additional 60 cm of shielding steel outside the magnet return yoke. It consists of a second set of four layers with a fixed length in $z$, varied in $\eta$, and forms a box around the central detector. A layer of scintillation counters(CSP) is installed on the outside surface of the CMP. The CMU and CMP each covers $|\eta| < 0.6$.

The CMX has eight layers and covers $0.6 < |\eta| < 1.0$. Each layer of scintillation counters (the CSX) is installed on both the inside and the outside surfaces of the CMX. There is a 30° gap of the azimuthal coverage in CMX/CSX at the top of the detector for the solenoid refrigerator and Tevatron Main Ring used in Run I.

The IMU consists of barrel chambers(BMU) and scintillation counters(BSU), and is designed to cover the region $1.0 < |\eta| < 1.5$ in trigger and could identify muons in the $\eta$ region up to 2.0 in offline.

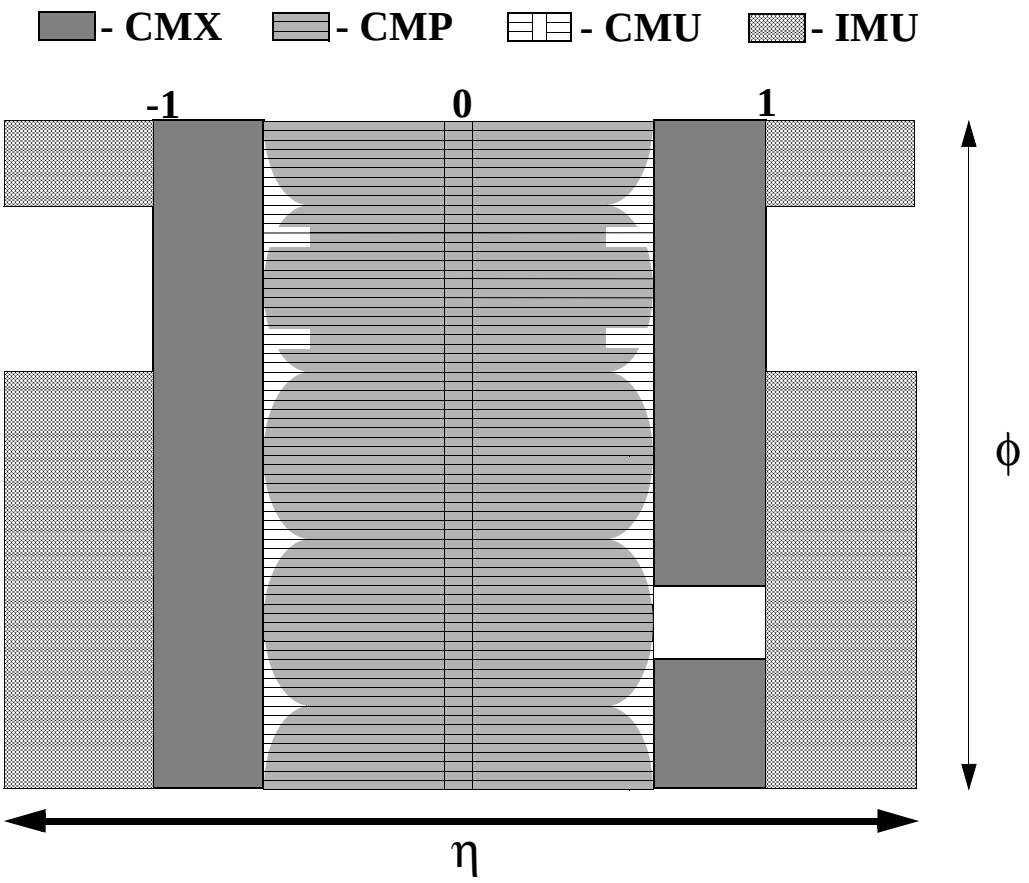


Figure 2.10: Muon coverage in $\eta$ and $\phi$.

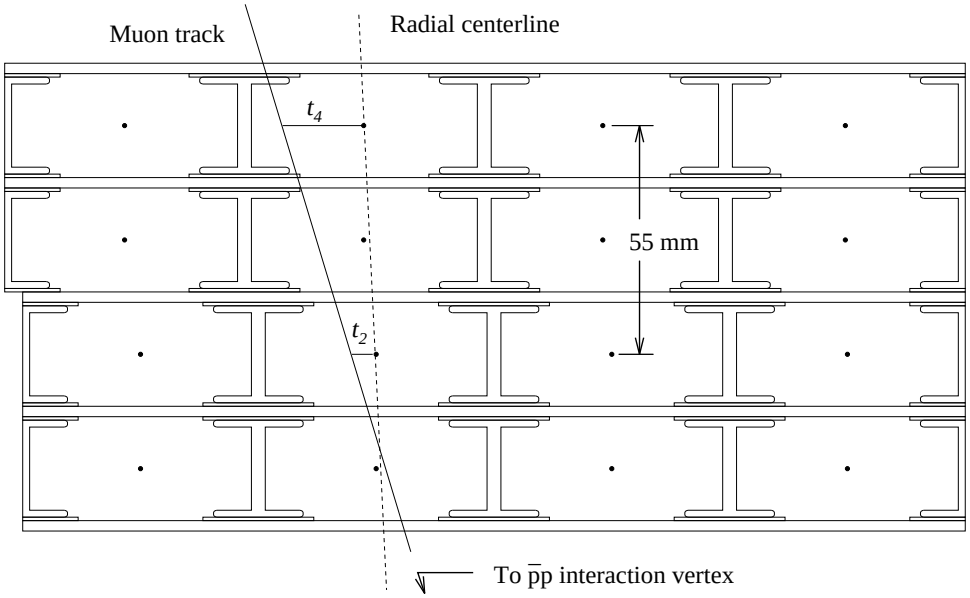


Figure 2.11: A matching example between a stub and a track

The hits in the muon chambers are linked to form a short track segment called a muon stub and this stub could be a good muon candidate if it is matched to an extrapolated track. Fig. 2.11 shows a matching example between a stub and a track.

The muons to be detected should have at least 1.4 GeV transverse momentum for CMU (2.2 for CMP, see Table 2.4 for the characteristics of each muon chambers) and trigger study shows the detection efficiency is above 99% for the muons of our interest (see Table 3.2.1).

## 2.3 Trigger and Data Acquisition

When a proton and anti-proton collide(we call it an event), various particles are produced. There could be interesting physics in the interaction. However, on average the digitized output of the detector is about 250 kB and an event comes every 396 ns(bunch-crossing rate). This will produce the huge amount of data. The purpose of trigger system is to reduce the data size by keeping as many interesting events as possible while rejecting uninteresting events. It consists of 3 levels called Level 1(L1), Level 2(L2), and Level 3(L3).

| | CMU | CMP/CSP | CMX/CSX | IMU |
|---|---|---|---|---|
| coverage | $\|\eta\| \lesssim 0.6$ | $\|\eta\| \lesssim 0.6$ | $0.6 \lesssim \|\eta\| \lesssim 1.0$ | $0.6 \lesssim \|\eta\| \lesssim 1.5$ |
| pion interaction length | $5.5\lambda$ | $7.8\lambda$ | $6.2\lambda$ | $6.2 - 20\lambda$ |
| minimum $p_T$(GeV) | 1.4 | 2.2 | 1.4-2.0 | |
| DRIFT TUBES | | | | |
| thickness(cm) | 2.68 | 2.5 | 2.5 | 2.5 |
| width(cm) | 6.35 | 15 | 15 | 8.4 |
| length(cm) | 226 | 640 | 180 | 363 |
| maximum drift time(ns) | 800 | 1400 | 1400 | 800 |
| total drift tubes | 2304 | 1076 | 2208 | 1728 |
| SCINTILLATORS | | | | |
| thickness(cm) | | 2.5 | 1.5 | 2.5 |
| width(cm) | | 30 | 30-40 | 17 |
| length(cm) | | 320 | 180 | 180 |
| total counters | | 269 | 324 | 864 |

Table 2.4: *The characteristics of muon chambers.*

Level 1 forms a set of requirement combined with energy information in calorimeter, track information by the eXtremely Fast Tracker(XFT), and muon information in muon chambers. Energy in calorimeter is collected by towers(HAD and/or EM). The XFT uses a two dimensional pattern recognition algorithm to perform a crude but fast track reconstruction, which allows us to trigger on electrons and muons at L1. The L1 trigger reduces the data rate from 2.5 MHz to 20 kHz or less.

Events accepted by L1 are processed by Level 2, a programmable processor. L2 trigger performs a primitive clustering of calorimeter towers which improves the electron/muon identification, and reconfirms/tightens L1 requirements. L2 reduces the trigger rate to 300 Hz which is a factor of 100 reduction.

Events passing L2 triggers are collected and formatted by a hardware processor called the Event Builder (EVB) and delivered to L3 trigger system, a PC farm with approximately 300 CPU's. L3 reconstructs high level Physics objects using essentially the same algorithms used in the final analysis. The L3 trigger contains approximately a hundred paths[1]. The maximum allowed rate at L3 is 75Hz. After passing L3 events are collected and stored on magnetic tapes.

[1]each trigger configuration in L3 has a special name called a path

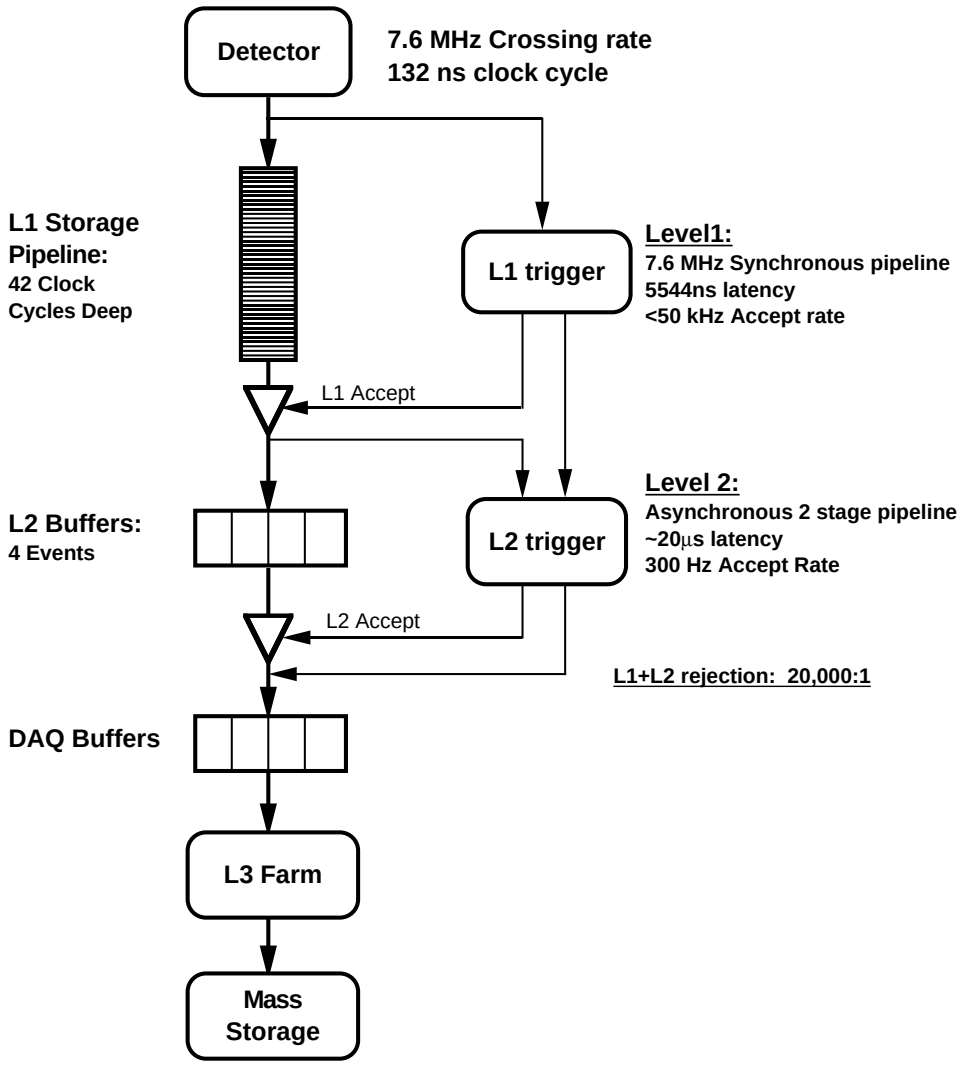


Figure 2.12: Data flow of "deadtimeless" trigger and data acquisition.

The data flow in the trigger system is shown in Fig. 2.12.

More information about detector specification and the idea of designing detectors can be found in [7] and [8].

# Chapter 3

# Event Selection

This chapter consists of four sections: Event Topology, Data samples, Particle Identification, and Event cuts. In the first section, the topology of the events in this analysis will be discussed. In the following section, we discuss the sample of data collected by the detector that we use for our search. These data come from several trigger paths, which will also be discussed. We also discuss the Monte Carlo (MC) samples used to determine the Higgs acceptance, as well as the background estimation. Then we discuss further purification of the data using improved particle identification criteria. Finally we discuss background suppression using event-topology requirements.

## 3.1 Event Topology

Although we are interested in Higgs, we can only see its decay products. We have already discussed the possible Higgs decay modes in Chapter 1, and we will focus on the ditau decay mode in this analysis. However, the tau particle is not the final state product because it decays. The tau decay modes can be categorized as "leptonic" and "hadronic", see Table 3.1[13]. The leptonic mode includes electron and muon final states.

| decay mode | branching fractions |
|---|---|
| $e\nu_e\nu_\tau$ | 17.84% |
| $\mu\nu_\mu\nu_\tau$ | 17.36% |
| hadrons | 64.80% |

Table 3.1: *The tau decay branching fractions in terms of "leptonic" and "hadronic" category.*

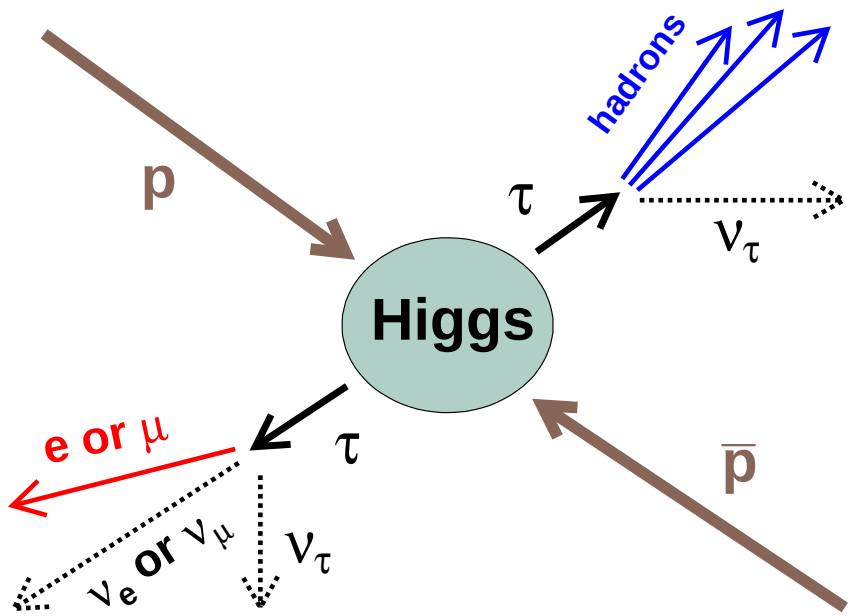


Figure 3.1: *The event topology in this analysis. Higgs decays two taus. We look for the events that have a lepton from one tau and hadrons from another tau in the final states.*

The hadronic decay mode is the largest. However, there is difficulty to look for both taus decaying hadronically because the $jet \rightarrow \tau$ mis-identification probability[1] is large as we will discuss later in Chapter 4. In this analysis, we will look for events that have a lepton from one tau and hadrons from the other tau shown in Fig. 3.1. Identifying a lepton from one tau has many advantages. First of all, it will reduce the $jet \rightarrow \tau$ mis-identification probability. The mis-identification probability of a lepton is extremely small ($< 10^{-4}$). The leptons in the detector, in general, are well understood. For both taus decaying by leptonic modes, the branching fraction is small and hard to distinguish from Drell-Yang events[2]. Consequently, looking for a leptonic mode for one tau and a hadronic mode for the other tau is a good compromise. Its branching fraction for the ditau system is relatively large and its fake probability is relatively small.

[1]the mis-identification probability will be often referred as "fake probability" or "fake rate" in this analysis.

[2]$Z/\gamma^*$ decays to di-leptons. Those events present in all energy range

## 3.2 Samples

Detector data from various trigger paths are searched for signal, while Monte Carlo data is used to model the Higgs signal and several major background processes, and calculate detector acceptances. An exception are backgrounds involving a QCD jet misidentified as a hadronic $\tau$ decay ($jet \rightarrow \tau$ mis-id), which we refer to as QCD background. This background requires special handling because we cannot simulate it properly. Hence, we need to estimate it by real jets collected by the detector (not MC).

### 3.2.1 Data samples

For this analysis, detector data are collected by a set of triggers called "LEPTON+TRACK". As discussed in 2.3, the "online" data refer to the reconstructed ones at Level 3, while the "offline" data refer to the same data processed by the the offline reconstruction software. The offline reconstruction includes more precise detector calibrations than is possible for the online. "Lepton+track" triggers include "electron+track", "muon($|\eta| < 0.6$)+track", and "muon($0.6 < |\eta| < 1.0$)+track". Here "track" requires that there is no track above 1.5 GeV in the region $0.175 < \Delta R < 0.524$ around a track of interest (called the "seed track"), where $\eta$ is the pseudorapidity of the muon track, and $\Delta R$ is defined as

$$\Delta R \equiv \sqrt{(\Delta\phi)^2 + (\Delta\eta)^2} \tag{3.1}$$

where $\Delta\phi$ is the difference in azimuth between the seed track and any other track, and $\Delta\eta$ is the equivalent difference in pseudorapidity. In practice, the quantities obtained from Level 3 (online) and "Production" (offline) are very similar, which gives us confidence in our triggering.

The "electron+track" trigger consists of Level 1, 2, and 3 requirements. Level 1 requires at least one CEM electron($E_T > 8\ GeV$ and $\frac{E_{HAD}}{E_{EM}} < 0.125$) matched with a XFT track ($p_T > 8\ GeV$) Level 2 reconfirms the L1 electron requirement and requires a second XFT track ($p_T > 5\ GeV$) with a separation of at least 10° between the electron

| Trigger name | Efficiency | CDF Note |
|---|---|---|
| L1_CEM8_PT8 | $0.98 \pm 0.01$ | 6257 |
| L2_CEM8_PT8_CES2 | $1.00 \pm 0.02$ | 6257 |
| L3_ELECTRON8 | $0.99 \pm 0.01$ | 6324 |
| L1_CMUP6_PT4 | $0.912 \pm 0.009$ | 7429 |
| L3_CMUP8 | $0.995 \pm 0.002$ | 7429 |
| L1_CMX6_PT8 | $0.969 \pm 0.008$ | 7429 |
| L3_CMX6_PT8 | $0.996 \pm 0.003$ | 7429 |
| L2_TRK5_DPHI10 | $0.98 \pm 0.01$ | 6510 |
| L3_TRACK5_ISO | $0.99 \pm 0.01$ | 6553 |

Table 3.2: *Trigger efficiencies at plateau. The first three rows are for electron triggers. The fourth and fifth rows are for muon ($|\eta| < 0.6$) triggers. The sixth and seventh rows are for muon ($0.6|\eta| < 1$) triggers. The last two rows are for isolated track triggers which are targeted at taus.*

and this track. Level 3 requires at least one electron candidate[3] with $E_T > 8\ GeV$, $p_T > 8\ GeV$ and $\chi^2_{CES} < 20$. $\chi^2_{CES}$ is the $\chi^2$ of the shower profile in CES detector. For the track side, it requires an isolated track with $p_T > 5\ GeV$ and $|\eta| < 1.5$.

The "muon+track" trigger consists only of Level 1 and Level 3 requirements. Level 1 requires hits in muon detector and a matching track with $p_T > 8\ GeV$ Level 3 requires at least one muon candidate with $p_T > 8\ GeV$, matching between the muon track and the hits in the muon detectors. For the track side, it requires an isolated track with $p_T > 5\ GeV$ and $|\eta| < 1.5$.

The trigger efficiencies and references are listed in Table 3.2.

We remove events from our detector data sample where the detector, online electronics or software was known to be malfunctioning. The resulting integrated luminosity of the sample is $310 \pm 19\ pb^{-1}$.

[3]In terms of algorithm how to reconstruct electrons, electron candidates at Level 3 are different from Level 1. First, the physical size of towers at Level 1 is larger than at Level 3. In the central region, two Physics towers (at Level 3) correspond to one L1 trigger tower, which affects clustering. Tracking is also different because XFT uses 2 dimensional information but Level 3 has access to 3 dimensional information.

### 3.2.2 Signal Monte Carlo Samples

Simulation of the signal, $p\bar{p} \rightarrow \phi \rightarrow \tau\tau$ is generated using Pythia 6.216 separately for the processes $bb \rightarrow \phi$ and $gg \rightarrow \phi$. These processes are expected to make the largest contribution to the MSSM Higgs production cross section. The event generation and subsequent simulation of the detector includes generation of additional underlying events and multiple interactions as run dependent detector conditions to reflect real data environment as closely as possible. The samples are generated for $\tan\beta$=30,50,80,100 in the mass region $90 < m_A < 200$ GeV. For the signal acceptances, the relative fraction between $gg \rightarrow A$ and $bb \rightarrow A$ is weighted according to the predicted cross sections dependent on $\tan\beta$ and $m_A$.

### 3.2.3 Background Samples

The possible backgrounds in this analysis are discussed in Chapter 5. Here we briefly list the types of data used for background estimation. Our biggest background, $p\bar{p} \rightarrow Z \rightarrow \tau\tau$ events, are generated by Pythia 6.216 and simulated using the same simulation software as the Higgs signal. The same is true for $p\bar{p} \rightarrow Z \rightarrow ee$, $p\bar{p} \rightarrow Z \rightarrow \mu\mu$, as well as $p\bar{p} \rightarrow t\bar{t}, WW, WZ, ZZ$.

In order to estimate the probability of a QCD jet faking a hadronic $\tau$ decay, we use real jets in the detector, collected by various triggers. These are the JET_20, JET_50, JET_70, JET_100, and JET_SINGLE_TOWER_5 triggers, where the numeral refers to the energy threshold applied to the jet at trigger level. An event which contains a QCD jet with 20 GeV of energy will fire the JET_20 trigger, while one which contains a 50 GeV jet will fire both the JET_20 and JET_50 triggers. The last trigger in the list requires an event to deposit at least 5 GeV of energy in a single tower. The rates of all these jet triggers are artificially attenuated (prescaled) to conform to the data acquisition trigger rate requirements.

## 3.3 Particle identification

The particles of interest in this analysis are electrons and muons from $\tau$ decays, as well as hadrons (mostly $\pi^{\pm}$'s,$\pi^{0}$'s) from hadronically decaying taus. Below we describe the selection criteria for identifying electrons, muons and $\tau$ in the data.

### 3.3.1 Electrons

Electron reconstruction starts with clusters in the EM calorimeter. Contiguous towers in the EM calorimeter exceeding a certain threshold are used to from an EM cluster, which contains 3 or fewer towers. After forming a cluster, the algorithm searches for a track pointing to the cluster. The transverse energy ($E_T$) of the EM cluster should be greater than 10 GeV and the transverse momentum ($p_T$) of the matched track should be greater than 8 GeV/c. Since electrons deposit most of their energy into the EM calorimeter, we also require the ratio of $E_{HAD}$ and $E_{EM}$ to be small, about 6%.

In the ideal case when an electron deposits all its energy in EM calorimeter, the ratio of the cluster energy and the matched track momentum (E/p) would be exactly 1. In this analysis, we require E/p to be less than 2 for the electrons (for electrons with $E_T < 50$ GeV). For electrons with $E_T > 50$ GeV, E/p distribution has large tail due to Bremsstrahlung. Therefore, we we do not require E/p $< 2$ for electrons with $E_T < 50$ GeV. Based on our knowledge of electron shower behavior in the EM calorimeter, we create a variable $L_{shr}$, which is a measure of the lateral profile of EM shower eq. 3.2. We require $L_{shr} < 0.2$.

$$L_{shr} = 0.14 \sum \frac{E_i^{adj} - E_i^{exp}}{0.14^2 E + (\Delta E_i^{exp})^2} \tag{3.2}$$

Here $E_i^{adj}$ is the measured energy in $i$th adjacent tower to the seed tower and $E_i^{exp}$ is the expected energy in $i$th tower (based on the test beam measurement of shower profiles). $\Delta E_i^{exp}$ is the error on the expectation.

Since a jet may on occasion contain an electron, we suppress this kind of jet background by requiring a track to be isolated such that $E_T^{iso,rel} < 0.1$.

$$E_T^{iso,rel} = \frac{\sum E_T^{iso}}{E_T^{cls}} \tag{3.3}$$

where $E_T^{cls}$ is the cluster energy and $E_T^{iso}$ is the sum of the energy towers within $\Delta R < 0.4$ around the center of cluster (with the cluster towers excluded). The additional isolation cuts ($p_T^{max,iso}$) require that there are no tracks with $p_T > 1$ GeV in an isolation cone $R < 0.4$ around the direction of the electron track.

The CES detector, described in Chapter 2 measures the lateral position of the EM showers. We requires the lateral position of showers measured by the CES to be close to the electron track. The CES detector measures positions in the x direction (from the wire plane ) and z (from the strip planes). The difference in x ($\Delta X$) between hit position in CES detector and the electron track extrapolated to the CES is required to be greater than -3 cm and less than 1.5 cm The absolute value of the difference in the z direction ($\Delta Z$) is required to be less than 3 cm. A $\chi^2_{CESstrip}$ of the electron candidates, calculated using the expected position measurement resolution is required to be less than 10. A possible background to electrons from $\tau$ decay are electrons from photon conversion. To eliminate photon conversions we compare all possible oppositely charged track pairs and reject electron tracks that are part of a pair that satisfies $|S_{XY}| < 0.2\ cm$, and $|\Delta cot\theta| < 0.04$, where $S_{XY}$ is the distance of the two tracks in the XY plane and $\theta$ is the polar angle of two tracks.

We also require electron candidates to be in the fiducial region of the tracking and calorimetry. This requires $|\eta| < 1$ and excludes nondetectable regions of the calorimeter.

Electrons (as well as muons and $\pi^{\pm}$ from $\tau$ decay are expected to form good tracks in the detector.

We now discuss criteria designed to select good tracks. Higgs particles are expected to have a very short lifetime compared to the tau leptons that the Higgses decay into.[4] We expect that all Higgs decay products come from the same vertex and very close to the beam line. We require the impact parameter ($d_0$) of tracks with respect to the beam line to be within $\pm 0.2$ cm. The events are distributed along the beam line with 95% of them located within $\pm 60$ cm, so we require the intersection ($z_0$) of tracks with the beam line be within $\pm 60$ cm of the detector's center. We also require tracks to

[4]Mean lifetime of the tau lepton is about $2.9 \times 10^{-17}$s or as $\sim$87 $\mu$m decay length.

| |
|---|
| $E_T > 10.0$ GeV |
| $p_T > 8.0$ GeV |
| $E_{HAD}/E_{EM} < 0.055 + 0.00045 * E$ |
| $L_{shr} < 0.2$ |
| $E_T^{iso,rel} < 0.1$ |
| $E/p < 2.0$ (no cut if $E_T > 50$ GeV) |
| $-3 < \|q\Delta X\| < 1.5$ cm |
| $\|\Delta Z\| < 3$ cm |
| $\chi^2_{CESstrip} < 10$ |
| $\|z_0\| < 60$ cm |
| $\|d_0^{corr}\| < 0.2$ cm |
| $\|z_{COT}\| < 155.0$ cm |
| $\geq 3$ *stereo*, 2 *axial* layers ($\geq 5$ hits) |
| fiduciality |
| conversion removal |
| $p_T^{max,iso} < 1$ GeV |

Table 3.3: Summary of electron cuts

traverse all the COT layers because the $\eta$ coverage of the COT is smaller than that of the calorimeters. We require the z position of the track extrapolation to the last COT superlayer ($z_{COT}$) be within $\pm 155$ cm. There are 8 superlayers in the COT. Four of them are axial and the rest are stereo. Each superlayer has 12 sense wires. The hits in the sense wires form a segment. The good segment requires at least 5 hits. The good quality tracks require at least 3 good segments in stereo type superlayers and 2 good segments in axial type superlayers. Table 3.3 summarizes the electron cuts.

### 3.3.2 Muons

This analysis uses central muons reconstructed in the CMU+CMP ($|\eta| < 0.6$) and CMX ($0.6 < |\eta| < 1.0$) detectors. Muon reconstruction starts from finding a set of hits (called a stub) in the muon detectors and tries to find a track that matches the stub. Muons are minimum ionizing particles (MIP) so that they do not deposit much energy in the calorimeters. We require the transverse momentum ($p_T$) of the muon track to be greater than 10 GeV. We require muon tracks to be isolated similar to the electrons. The isolation requirement is one of the most powerful cuts for removing jet

backgrounds like electrons. $E^{iso}_{T,rel}$ is defined as

$$E_T^{iso,rel} = \frac{\sum E_T^{iso}}{p_T} \tag{3.4}$$

where $p_T$ is the transverse momentum of the muon track and $E_T^{iso}$ is the energy sum of the towers (towers hit by the muon track are excluded) in $\Delta R < 0.4$ around the muon track. The high $p_T$ muons respond differently in the detectors compared to the low $p_T$ muons so those must satisfy the different requirements.

For muons with $p_T > 20$ GeV, we require the EM energy to be less than $2 + max(0, 0.0115 * (p - 100))$ GeV and the HAD energy to be less than $6 + max(0, 0.028 * (p - 100))$ GeV, where p is the momentum of the muon track. The difference between the x position of muon stubs in the muon detectors and the x position of the muon track extrapolated to the muon detector ($\Delta X$) is required to be less than 3 cm for the CMU detector, 5 cm for CMP detector, and 6 cm for the CMX detector.

For muons with $p_T < 20$ GeV, we require the EM energy to be less than 2 GeV and the HAD energy to be less than $3.5 + (p_T/8))$ GeV, where $p_T$ is the transverse momentum of the muon track. The $\chi^2$ of the x position of the muon stubs in the muon detectors and the x position of the muon track extrapolated to the muon detector is calculated using the expected scattering of the muon track in the detector. We require $\Delta X_{CMU}$ for the CMU detector to be within 3 cm or $\chi^2_{CMU} < 9.0$, $\Delta X_{CMP}$ for the CMP detector case to be within 5 cm or $\chi^2_{CMP} < 9.0$, and $\Delta X_{CMX}$ for the CMX detector case to be within 6 cm or $\chi^2_{CMX} < 9.0$ for the low $p_T$ muons.

We apply the generic track related cuts to the muon as we did to the electrons, regardless of muon $p_T$. We require the impact parameter ($d_0$) of the muon tracks with respect to the beam line to be within $\pm 0.2$ cm, the intersection ($z_0$) of tracks to the beam line to be within $\pm 60$ cm and the z position of the track extrapolation to the last COT superlayer ($z_{COT}$) to be within $\pm 155$ cm. The good quality muon tracks require at least 3 good segments in stereo type superlayers and 2 good segments in axial type superlayers. Table 3.4 summarizes the muon cuts.

| For all muons |
|---|
| $p_T > 10.0$ GeV |
| $\lvert z_0 \rvert < 60$ cm |
| $\lvert d_0^{corr} \rvert < 0.2$ cm |
| $E_{T,rel}^{iso} < 0.1$ |
| $\geq 3$ *stereo*, 2 *axial* layers ($\geq 5$ hits) |
| $z_{COT} < 155$ cm |
| **For $p_T > 20$ GeV muons** |
| $E_{EM} < 2 + max(0, 0.0115 * (p - 100))$ GeV |
| $E_{had} < 6 + max(0, 0.028 * (p - 100))$ GeV |
| $\lvert \Delta X_{CMU} \rvert < 3$ cm (CMU) |
| $\lvert \Delta X_{CMP} \rvert < 5$ cm (CMUP) |
| $\lvert \Delta X_{CMX} \rvert < 6$ cm (CMX) |
| **For $p_T < 20$ GeV muons** |
| $E_{EM} < 2$ GeV |
| $E_{had} < 3.5 + (p_T/8.0)$ GeV |
| $\lvert \Delta X_{CMU} \rvert < 3$ cm **or** $\chi^2_{CMU} < 9.0$ |
| $\lvert \Delta X_{CMP} \rvert < 5$ cm **or** $\chi^2_{CMP} < 9.0$ |
| $\lvert \Delta X_{CMX} \rvert < 6$ cm **or** $\chi^2_{CMX} < 9.0$ |

Table 3.4: Summary of muon cuts

### 3.3.3 Taus

Tau reconstruction refers to reconstruction of the visible decay products $X_h$ of tau leptons that undergo *semi-hadronic* decay: $\tau \to X_h \nu_\tau$. $X_h$ can be a $\pi^\pm/K^\pm$, or some short-lived intermediate resonance that decays directly (or through some intermediate states) to final states containing $\pi^{\pm,0}$, $K^{\pm,0}$. Table 3.5 lists the most important topological hadronic decay modes of tau leptons.

| $X_i$ | $\mathcal{B}_i$ (%) | $\mathcal{B}_i / \sum_j \mathcal{B}_j$ (%) |
|---|---|---|
| $h^-\pi^0$ | 25.86 | 40.4 |
| $h^-$ | 11.75 | 18.3 |
| $h^-h^+h^-$ | 10.01 | 15.6 |
| $h^-2\pi^0$ | 9.39 | 14.7 |
| $h^-h^+h^-\pi^0$ | 4.53 | 7.1 |

Table 3.5: *The top five most important topological final states of hadronic tau decays. $\mathcal{B}_i \equiv \mathcal{B}(\tau \to X_i \nu_\tau)$ are the tau branching fractions for the respective decay modes; $h^-$ stands for $\pi^-$ or $K^-$. Charge conjugate states are implied.*

Due to Cabbibo angle and phase-space suppression, the fraction of $K^{\pm}$ from $\tau$ decay is small compared to $\pi^{\pm}$. In tau reconstruction, we treat all charged tracks as pions. The $\pi^0$'s in the final state decay to $\gamma\gamma$ 98.8% of the time. Most of the time, the opening angle between the photons is not large enough for them to be individually resolved. In tau reconstruction we assume that the photons are merged. This has a small effect on the reconstructed mass (due to assigning the $\pi^0$ mass to photons in some small number of cases). Dalitz decays of $\pi^0$'s may lead to observation of additional tracks, but due to the small branching fraction ($\sim 1.2\%$) and low $\pi^0$ multiplicities in tau decays, we do not attempt to identify these decays.

Based on the major $\tau$ decay modes, hadronic tau decays are expected to produce characteristic track-multiplicity signature in the detector showing enhancements in the 1- and 3-track multiplicity bins. Sometimes leakage into the 2- and 4-track bins occur due to track reconstruction inefficiencies, and contributions of tracks from underlying event and conversions.

Besides track multiplicity, the mass of the hadronic system is used as a discriminating factor against QCD jets. The mass of the tau lepton is $m_\tau = 1.777$ GeV, and therefore, the invariant mass of the decay products is required to be less than this value.

Another implication of the tau lepton mass is that the decay products (for tau energies relevant for $Z, W$ and Higgs studies at CDF) form very narrow jets in the calorimeter.

Hadronic tau reconstruction starts with finding a seed calorimeter tower with transverse energy $E_T^{seed\ twr} > 6$ GeV. Adjacent shoulder towers with energies $E_T^{sh\ twr} > 1$ GeV are added to form a calorimeter cluster. Due to the narrowness of tau jets, the total number of towers contributing to the cluster $N^{twr}$ is required to be less than or equal to six.

The next step is to find a seed track for the hadronic tau candidate. This track must point to the calorimeter cluster and have momentum $p_T^{seed\ tr}$ exceeding some threshold. If several such tracks are found, the one with the highest $p_T$ is chosen. The direction of the seed track is then used as a *reference direction* for all following steps. Other COT tracks are associated with the tau based on their closeness to the selected seed track.

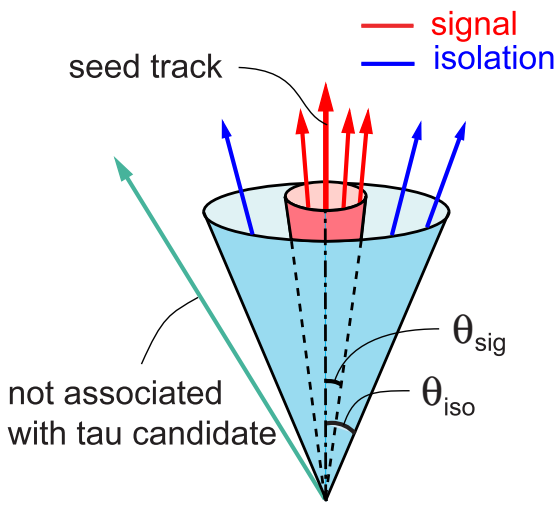


Figure 3.2: *Tau signal cone and isolation annulus for tracks and $\pi^0$'s.*

These shoulder tracks must have sufficiently high momentum $p_T^{sh\ trk}$, small separation $\Delta z^{sh\ trk}$ from the $z$-intercept of the seed track, and be within 3-D angle $\theta_{iso}$ with respect to the reference direction. Tracks within angle $\theta_{sig}$ are considered tau decay products, while ones with $\theta_{sig} < \theta < \theta_{iso}$ are treated as isolation tracks and used to veto tau candidates. Thus, the angles $\theta_{sig}$ and $\theta_{iso}$ define a signal cone and isolation annulus as shown in Figure 3.2. The signal cone size depends on the cluster energy $E^{\tau\ cl}$. A more detailed discussion of the dependence on cone size over cluster energy can be found in [15].

Neutral pions are associated with the tau candidate following the same procedure as for shoulder tracks. They are reconstructed using CES clusters to determine their position, and the CEM to assign energy. The $\pi^0$ reconstruction procedure is described in a separate note [18].

Tracks and $\pi^0$'s in the signal cone are used to construct the four-momentum of the hadronic system. The four-momentum is used in subsequent event cuts and for the determination of the mass of the system $M(\text{trks} + \pi^0 s)$. In a small fraction of cases there is a non-negligible energy loss due to $\pi^0$ reconstruction efficiency (mostly when they hit near the edges of the CES detectors). Therefore, in some cases one has to apply corrections to the tau energy. The need for energy corrections was discussed

in [17]. Here we define a single correction in the case when the calorimeter cluster energy is larger than the energy of the tracks+$\pi^0$'s ($E_T^{\tau cl} > p_T(trks + \pi^0 s)$) and $|E_T^{\tau cl} - p_T(trks + \pi^0 s)| \geq 3\sigma_{had}$. That latter condition ensures that the difference is not due to hadronic energy fluctuation. For tau candidates passing these two requirements we use $E_T^{\tau cl}$ instead of $p_T(trks + \pi^0 s)$.

Electrons and muons can sometimes resemble a hadronic tau decay to a single $\pi^{\pm}$. We now discuss selection criteria to suppress electrons and muons faking single charged pions. We define the variable $\xi'$ to suppress electrons and muons depositing a large amount of EM energy. It is a variation of the previously used $\xi$ cut[16] differing by the addition of a constant term to the EM fraction part.

The equations below demonstrate this difference.

$$\xi = \frac{E_{HAD}}{\sum |\overrightarrow{p}|} = \frac{E_{tot}}{\sum |\overrightarrow{p}|} \left(1 - \frac{E_{EM}}{E_{tot}}\right), \tag{3.5}$$

$$\xi' = \frac{E_{tot}}{\sum |\overrightarrow{p}|} \left(0.95 - \frac{E_{EM}}{E_{tot}}\right), \tag{3.6}$$

where $E_{tot}$, $E_{EM}$, $E_{HAD}$ are the total, electromagnetic and hadronic tau cluster energies, and $\overrightarrow{p}$ are the momenta of charged tracks associated with the tau. Figures 3.3 demonstrates the effect of the $\xi'$ cut. This cut is needed more for muon suppression, than electron removal[5] (when the electron removal procedure described below is used).

To further suppress electrons (possibly accompanied by bremsstrahlung), we reject 1-prong tau candidates if a CES cluster with $E_{CES} > 0.5 p_T^{trk}$ and $|\Delta z_{CES}| < 2.0$ cm of the projection of the track **and** in $\phi$ lies between the CES intersect of the track helix and its tangential. To account for CES position, and track extrapolation resolution, the veto region is extended by 0.01 rad beyond the points of the tangential intersect track hit in CES. Some of electrons not accompanied by bremsstrahlung are also suppressed.

Table 3.6 shows a summary of the tau reconstruction and ID cuts described above.

[5]We decided to use $\xi'$ for the $\tau_e\tau_h$ channel to have identical tau ID cuts, despite the small loss of efficiency.

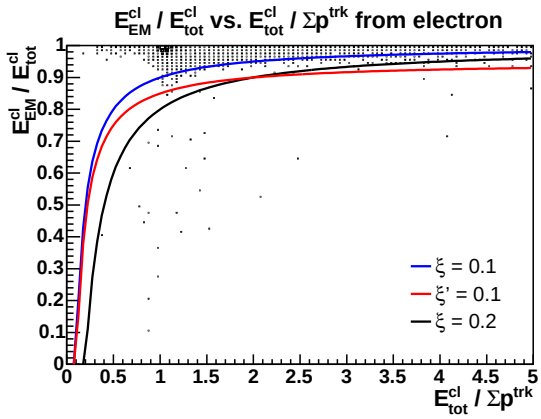


(a) Electrons

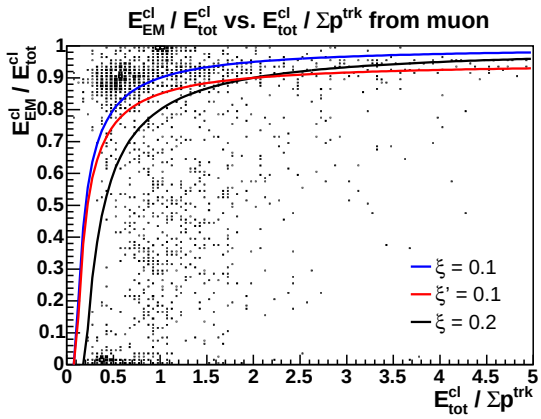


(b) Muons

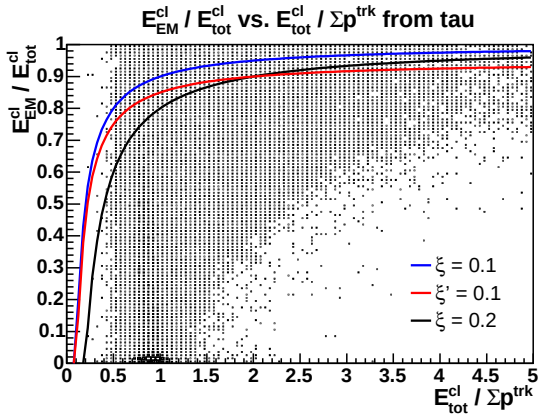


(c) Taus

Figure 3.3: *EM fraction vs. $E/P$ for MC $e$, $\mu$, and $\tau$. The $\xi$ ($\xi'$) cuts reject tau candidates above the respective lines.*

| |
|---|
| $E_T^{seed\ twr} > 6.0$ GeV |
| $E_T^{sh\ twr} > 1.0$ GeV |
| $N^{twr} \leq 6$ |
| $\theta_{sig} = min(0.17,\ \frac{5.0\ \text{rad/GeV}}{E^{\tau\ cl}})$ rad[6] |
| $\theta_{iso} = 0.52$ rad |
| $p_T^{seed\ trk} > 6.0$ GeV [7] |
| $p_T^{sh\ trk} > 1.0$ GeV |
| $E_T^{\tau cl} > 15.0$ GeV |
| $p_T(trks + \pi^0\text{'s}) > 15.0$ GeV |
| $\Delta z^{sh\ trk} < 5.0$ cm |
| $9.0 < \lvert z_{CES}^{seed\ trk} \rvert < 230.0$ cm |
| traverse all 4 axial SL's in COT |
| $\xi' > 0.1$ |
| Brem removal |
| $\sum p_{T,trk}^{iso} < 1$ GeV |
| $\sum E_{T,\pi^0}^{iso} < 1$ GeV |
| $N_{sig}^{trk} = 1, 3$ |
| $\lvert \sum Q^{trk} \rvert = 1$ |
| $M(\text{trks} + \pi^0 s) < 1.8$ GeV |

Table 3.6: Summary of tau cuts

## 3.4 Event cuts

Apart from the irreducible background from $Z/\gamma^* \to \tau\tau$ the other **major** backgrounds in this analysis are $Z/\gamma^* \to ll$, $W \to l\nu + jet(s)$ $(l = e\mu)$, and "QCD" $(p\bar{p} \to \text{n}jets)$. The event cuts are designed as a compromise between effective suppression of **these** backgrounds and maintaining sufficient signal efficiency. Other backgrounds, such as $t\bar{t}$, $WW$, $WZ$, and $ZZ$ are taken into account in the analysis but due to their small production cross sections, they play a limited role in designing the cuts.

### 3.4.1 $\not\!\!E_T$ corrections

$\not\!\!E_T$ is defined as follows.

$$\not\!\!E_T \equiv \sqrt{(\sum_{towers} E_X)^2 + (\sum_{towers} E_Y)^2} \tag{3.7}$$

The exact definition should be negative but we often use this without the minus

sign. In the analysis we do not place any direct requirements on $\not\!\!E_T$, however, it is used in combination with other variables. The "raw" $\not\!\!E_T$ in the event (a vector sum of the calorimeter towers) is corrected for the $z$-position of the interaction that produced the tau candidates. When the tracks of the taus are within 5 cm of the $z$-coordinate of a reconstructed primary vertex, $\not\!\!E_T$ is corrected with respect to the primary vertex. In all other cases the correction is applied using the $z_0$ of the tau seed track. We apply muon corrections when a track is determined to be a muon. Hadronically decaying taus are a very special kind of jet and the standard jet energy determination can not be used. We apply tau corrections to $\not\!\!E_T$ by removing the $E_T$ assigned to the tau cluster and the neighboring towers(to account for energy leakage) and replacing it with the $p_T$ of the tau candidate. Standard jet energy calibrations are used for all jets with raw $E_T > 8$ GeV if they are not identified as $e$, $\mu$, $\tau$, or $\gamma$.

### 3.4.2 Anti $Z \to ll$ cuts ($l = e, \mu$)

These cuts are directed at suppressing $Z \to ll$ events where an electron or a muon was misidentified as a hadronic tau decay.

In the muon case, we form the invariant mass $M_{test}$ of identified muons with reconstructed 1-prong taus, using track momenta. Events in the mass region $|M_{test} - M_Z| <$ 10 GeV are vetoed. In the case of $Z \to ee$ the requirements are relaxed since electron removal from hadronic tau decay candidates is already quite efficient in removing these events. Only hadronic tau decay candidates with a track projected outside of the fiducial CES region $|x^{loc}_{CES}| > 21$ cm are used to form the invariant mass ($m_e e$), and the Z region is removed as above.

### 3.4.3 QCD suppression cuts

Jets are suppressed to a significant degree by the hadronic tau ID cuts. However, at low $E_T$ their numbers are so large that further event cuts are needed to clean up the sample. We define

$$\tilde{H_T} = |P_T^{vis}(\tau_1)| + |P_T^{vis}(\tau_2)| + |\not\!\!E_T|.$$

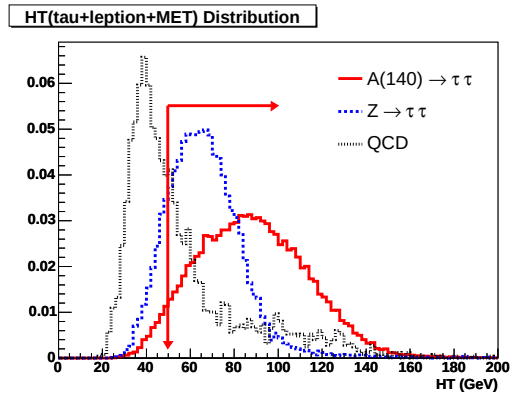


Figure 3.4: *Effect of the $\tilde{H}_T$ cut on $Z$, $\phi(140)$, and QCD-dominated data sample. All distributions are normalized to unit area.*

We have intentionally avoided inclusion of jets accompanying the $\phi/Z$ to avoid issues with MC modeling. However, at a later time including more complete information may prove beneficial. Figure 3.4 shows the expected distributions for $Z$, $\phi$, and from QCD events.

The QCD distributions are obtained from the detector data sample, but without applying tau ID cuts to the jets. While it contains some real taus, this sample is dominated by jets, especially at the low-$\tilde{H}_T$, which we wish to reject. The suggested cut $\tilde{H}_T > 50$ GeV leads to small loss of signal efficiency, while providing considerable QCD suppression. The impact of this cut on signal is further reduced when probing for higher-mass $\phi$.

### 3.4.4 $\zeta$ cut

The "$\zeta$ cut" is an attempt to discriminate events with $\not{E}_T$ that are not consistent with a particle decaying to two taus. It is mostly targeted at suppressing $W \rightarrow l\nu + jet(s)$ events were the jet fakes a hadronic tau decay. However, it also helps to suppress QCD, $t\bar{t}$ and di-boson events.

We define a bisection axis $\vec{\zeta}$ in the transverse plane for the directions of the visible tau decay products (see Figure 3.5). The transverse momentum of $\phi$ (or any other

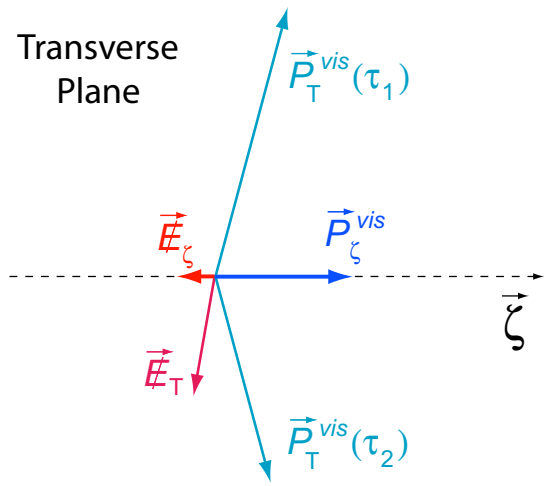


Figure 3.5: *Illustration of the definition of parameters used in the $\zeta$ cut.*

particle decaying to two taus) is

$$\vec{P}_T^{\phi} = \vec{P}_T^{vis}(\tau_1) + \vec{P}_T^{vis}(\tau_2) + \vec{\not{E}}_T,$$

where we assume that $\vec{\not{E}}_T$ is the sum of the transverse momenta of the neutrinos from tau decays. The transverse momentum of the tau visible products is

$$\vec{P}_T^{vis\ \tau} = \vec{P}_T^{vis}(\tau_1) + \vec{P}_T^{vis}(\tau_2).$$

The projections of $\vec{P}_T^{\phi}$ and $\vec{P}_T^{vis\ \tau}$ onto the defined $\vec{\zeta}$ axis are

$$P_\zeta^{\phi} = \vec{P}_T^{\phi}.\vec{\zeta}$$

and

$$P_\zeta^{vis\ \tau} = \vec{P}_T^{vis\ \tau}.\vec{\zeta},$$

respectively.

Figure 3.6 shows the $P_\zeta$ *vs* $P_\zeta^{vis\ \tau}$ distribution for $\phi \to \tau\tau$, and $W \to l\nu + jet(s)$ MC events. The distributions are plotted after applying the other event cuts. The graphical cut shown on these plots results in small efficiency loss and substantial background suppression.

The rationale behind this cut is simple: both the neutrinos and the visible decay products from tau decays go at small angles from the initial tau direction (at our energy

scale). Therefore, the sum of the neutrino's momenta should not go opposite to the direction of the sum of visible products. The defined acceptance region implicitly takes into account factors like direction and energy resolution of reconstructed taus, $\not{E}_T$ resolution, etc. The cut placement is determined by inspecting the predicted distributions and minimizing the signal losses. Figure 3.6 shows the effect of the cut on signal (Higgs) and $W + jet(s)$ background.

### 3.4.5 Charge Requirements

The lepton and the hadronic decay products of the tau pair are required to have opposite charge: $Q_l Q_{\tau_h} = -1$. This cut is mostly directed at suppressing multi-jet events. In these cases there is equal probability to get same/opposite sign candidates.

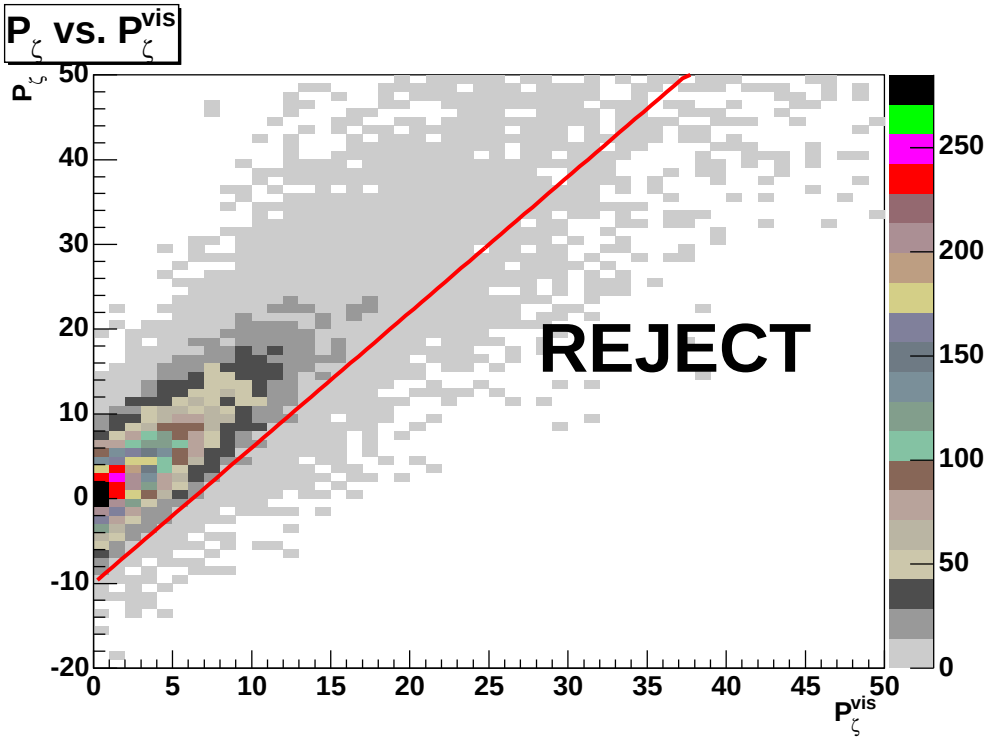


(a) $A \to \tau\tau$ MC

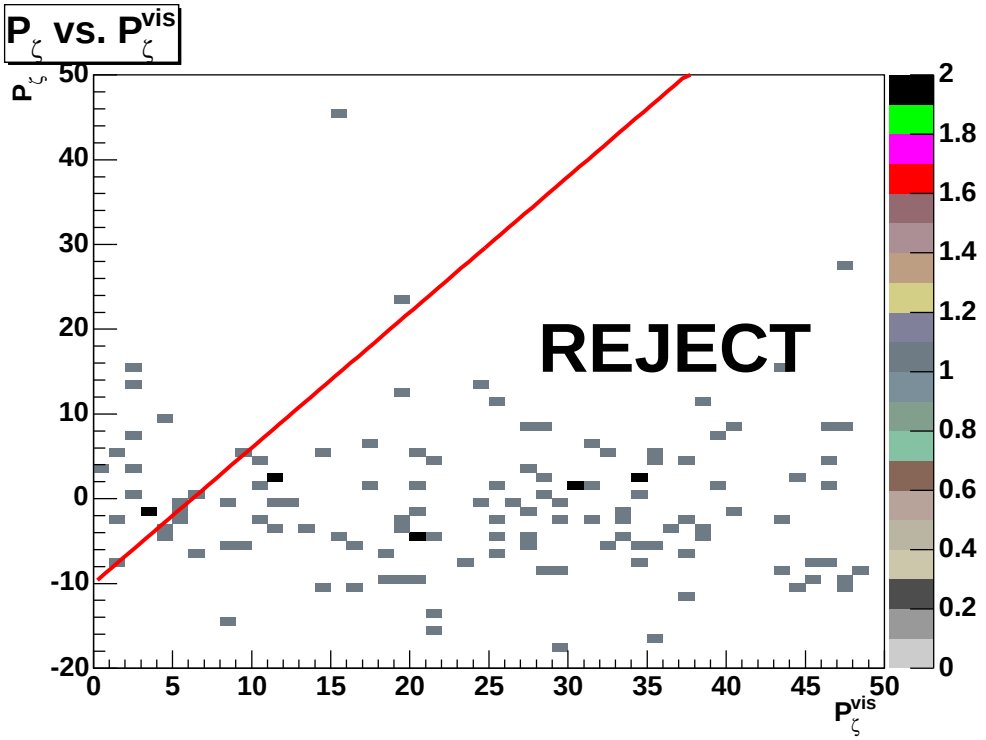


(b) $W \to e\nu$ MC

Figure 3.6: *Effect of the $\zeta$ cut. (a) shows the acceptance of this cut on the signal $A \to \tau\tau$ MC. (b) shows the rejection of this cut against the $W$ background.*

# Chapter 4

# Efficiency and Fake rate

The efficiency to reconstruct tau decays is defined as the ratio of such taus reconstructed by our analysis to the total number of taus in the sample. For instance, if the tau selection efficiency is known to be 90% and we reconstruct 900 taus from our data sample, then we may assume that there were 1000 taus in the data sample. The fake rate, or misidentification probability, is similar to the efficiency, but for a different initial data source. The generic term "fake rate" in our analysis denotes jets from QCD decays which somehow reconstruct as hadronic tau decays in our analysis. If we reconstruct 200 taus from a sample of 1000 jets (note: these jets must be pure jets and not contaminated with hadronic taus) then we can assume that the $jet \rightarrow \tau$ fake probability is 20%. Since we cannot use the simulation to estimate fakes due to QCD jets, we use the fake rate as in the background estimation method. At this point, we need to separate the statement of "fake rate" and "background from fake rate". The fake rate itself is the probability for a given background object to look like a signal object. The background contribution to our tau sample comes from generic jet events, dijet events, as well as jets accompanying semileptonic decays of W bosons. The event topologies and jet kinematics for these various types of events may be quite different. The beauty of using the fake rate is that we need not worry about the source of jets, since we can parametrize the fake rate in various quantities of interest. We will discuss more details about this in the separate Chapter 5.

In this chapter, we will first discuss electron and muon efficiency. These are well studied at CDF. Then we will discuss the efficiency of hadronic tau identification by using MC samples. We define the absolute and relative efficiencies and discuss the way to use them. The $jet \rightarrow \tau$ mis-identification is translated as $jet \rightarrow \tau$ fake probability

so that we can determine how many selected taus might be non-taus (jets). We will measure this probability by using data collected by jet triggers. The reason we use real data (not MC) is that we don't have precise knowledge of the PDF's. Sometimes, we will use the jargon "fake rate" instead of fake probability, but the meaning of two are the same in our context.

## 4.1 Electron/Muon Efficiency

.

We use the suggested electron [11] and muon [12] cuts so that we can use efficiencies and systematics determined by other CDF analyses. Fake rates[1] for electrons and muons are negligible compared to those of taus. We define two regions, low $p_T(p_T < 20GeV)$ and high $p_T(p_T > 20GeV)$. For the low $p_T$ electrons, the efficiency is about $80.8 \pm 0.9\%$. There is some difference between data and MC due to mis-modeling. This effect of imperfection in the MC propagates to every cut. Therefore we define a "Data/MC identification(ID) scale factor" or just "scale factor" to account for the discrepancy between data and MC. The electron scale factor is about $1.03 \pm 0.02$ for the low $p_T$ region. For the high $p_T$ electrons, the efficiency is about $81.3 \pm 0.5\%$. The ID scale factor is $0.999 \pm 0.006$. For the low $p_T$ CMUP muons, the reconstruction efficiency is about $93.2 \pm 0.8\%$ and the ID efficiency is $86.4 \pm 7.0\%$. The ID scale factor is $0.85 \pm 0.07$. For the high $p_T$ CMUP muons, the reconstruction efficiency is the same as for low $p_T$ and the ID efficiency is $87.1 \pm 0.6\%$. The ID scale factor is $0.88 \pm 0.01$. For the low $p_T$ CMX muons, the reconstruction efficiency is about $98.7 \pm 0.3\%$ and the ID efficiency is $87.8 \pm 7.0\%$. The ID scale factor is $0.96 \pm 0.08$. For the high $p_T$ CMX muons, the reconstruction efficiency is the same as for low $p_T$ and the ID efficiency is $93.2 \pm 0.6\%$. The ID scale factor is $0.997 \pm 0.007$. The details of scale factor determination can be found in [11],[12].

[1] In this analysis, when fake rate is mentioned, it refers the probability of jets faking interesting particles. For the fake rate of electrons/muons, it is negligible compared to that of taus. For taus, it's the probability of jets faking hadronically decaying taus

| |
|---|
| "TauObject" matched to the tau(for efficiency) or jet(for fake rate) |
| Pass the $\xi' > 0.1$ cut |
| Trigger isolation requirement |
| $\lvert z_0^{seed\ trk}\rvert < 60.0$ cm |
| $9.0 < \lvert z_{CES}^{seed\ trk}\rvert < 230.0$ cm |
| Seed track quality: $\geq 3$ stereo, $\geq 2$ axial layers ($\geq 5$ hits) |

Table 4.1: List of loose cuts for tau selection

## 4.2 Tau Efficiency and Fake rate

.

Efficiency and fake rate are similar in terms of their definitions. The main difference is the sample. Efficiency is defined as how many *real* taus are selected at a given condition, while $jet \rightarrow \tau$ fake rate is defined as how many jets that are *not taus* are selected using a given set of tau binding criteria. In this respect, the samples used to determine efficiency are MC[2], while for the $jet \rightarrow \tau$ fake rate measurement, we use jet triggered data as described in Section 4.2.2.

We define two kinds of efficiency(fake rate), *absolute* and *relative*. The difference between them is the denominator. The absolute efficiency illustrates how efficiently taus are identified under the CDF framework, while the absolute fake rate describes how efficiently jets are rejected. The denominator for absolute efficiency(fake rate) has the fiducial requirement defining the region within which particles can be detected. This analysis considers only the central region($|\eta| < 1$).

The relative efficiency and fake rate have common denominator. They are defined with respect to some prior requirements called **"loose cuts"** listed at Table 4.1.

The first requirement is important because it allows us to use the same parameters when defining efficiency and fake rate. Typically, about $\sim 50\%$ of generic jets are reconstructed as "TauObjects"[3]. The second requirement excludes small parameter space that is not relevant for fake estimation in our final sample and reduces electron

[2]We don't have good calibration data for taus. That's why the MC is used for efficiency. However, any possible discrepancies between data and MC are taken into account. See Chapter 6

[3]The formation of TauObject are described in Section 3.3.3

contamination. The third requirement ensures that we can use the same data sample for extracting the signal and determining $jet \rightarrow \tau$ fakes[4]. The rest of the requirements ensure geometrical and tracking quality consistency with the final sample. **"Tight cuts"** requires passing all cuts described in Section 3.3.3 including "loose cuts".

### 4.2.1 Tau Efficiency

Tau reconstruction efficiency is determined from the MC simulation due to the lack of calibration data. Absolute efficiency is estimated for taus that originate from the luminous region ($|Z_0| < 60.0cm$) and pass the fiduciality requirements (highest $p_T$ track projection to the CES detector $9.0 < |z^{trk}_{CES}| < 230.0$ cm). Absolute efficiency can be defined as a function of reconstructed or generated energy and is a true measure of reconstruction performance. It is implicitly included when event selection efficiency is estimated from the MC simulation. The overall absolute efficiency is about 50%. However, the value of the absolute efficiency is not used in this analysis. Here we list the efficiencies for individual tau ID cuts as estimated from $Z \rightarrow \tau\tau$ MC. Table 4.2 shows the marginal efficiency for individual cut which is the efficiency for applying all cuts[5] except for one cut of interest.

The consistency between data and MC for individual tau selection cuts is cross-checked using data samples and whenever applicable, scaling factors are derived. These comparisons are also used to determine the systematic uncertainty of tau ID. Details on how we perform these checks are given in Chapter 6. Here we give a summary of the systematic uncertainties in tau ID.

Relative efficiency is defined as

$$\epsilon_r = \frac{N^{\tau}_{tight}}{N^{\tau}_{loose}}$$

where $N^{\tau}_{loose}$ is the number of taus passing tight cuts and $N^{\tau}_{tight}$ is the number of taus

[4]As discussed in Section 3, the "LEPTON+TRACK" data have isolation cut in Level 3. In the assumption that offline and Level3 triggers are same, we can simulate the trigger level isolation effect on the jet triggered data.

[5]all cuts are listed in sec 3.3.3.

| *cut* | Marginal efficiency (%) |
|---|---|
| $\|z_0\| < 60$ | $96.34 \pm 0.08$ |
| $\|d_0\| < 0.2$ | $98.86 \pm 0.04$ |
| $9 < \|z_{CES}\| < 230$ | $95.07 \pm 0.09$ |
| Track Quality | $99.23 \pm 0.04$ |
| $\xi' > 0.1$ | $87.24 \pm 0.13$ |
| $E_T^{seed\ twr} > 6$ | $99.69 \pm 0.02$ |
| $p_T seed\ trk > 6$ | $96.66 \pm 0.07$ |
| Track iso L3 | $99.35 \pm 0.03$ |
| $\sum p_T^{trk\ iso} < 1$ | $77.37 \pm 0.15$ |
| $\sum p_T^{\pi^0\ iso} < 1$ | $97.18 \pm 0.07$ |
| $m_\tau < 1.8$ GeV | $95.34 \pm 0.09$ |

Table 4.2: *Effect of individual cut on tau selection efficiency for* $p_T > 15\ GeV$, $E_T^{\tau\ cl} > 15\ GeV$. *Marginal efficiency is obtained by applying all cuts except the one interesting.*

passing loose cuts. Due to the relative efficiency is determined with respect to loose taus, it is numerically higher than absolute efficiency. The relative efficiency is actually used to calculate QCD backgrounds as a correcting factor for tau contamination. It is parameterized in terms of *measured* quantities to match the parametrization used for jets : $E_T^{\tau\ cl}$, $E_T^{jet}$, and track multiplicity. $E_T^{jet}$ is the cluster energy of the jet matched with a tau candidate. One can wonder how a tau can be a jet. That's because every tau candidate is reconstructed as a jet object, as well.

The efficiency is determined from the ratio of number of tight to number of loose taus in bins (partitions) in the 3D parameter space. This parametrization of the efficiency and the corresponding distributions shown in Figure 4.3 are useful only in the procedure for estimating the $jet \rightarrow \tau$ fakes).

### 4.2.2 $jet \rightarrow \tau$ Fake rate

QCD background can be estimated by measuring the relative $jet \rightarrow \tau$ fakes. The procedure to estimate QCD is discussed in Section 5.1.4. The relative fake rate is defined with respect to the loose tau in analogy to the relative efficiency.

$$f_r = \frac{N_{tight}^{jet}}{N_{loose}^{jet}}$$

where $N_{loose}^{jet}$ is the number of jets passing tight cuts and $N_{tight}^{jet}$ is the number of jets passing loose cuts.

The $jet \rightarrow \tau$ fake rates are studied using the jet samples obtained by different trigger samples. The most important condition is Level 3 threshold. We select five different samples. "JET SINGLE TOWER 5" is characterized by selecting jets with $E_T > 5$ GeV. "JET 20" is the collection of events with at least one jet that is $E_T > 20$ GeV. "JET 50, 70, 100" has similar thresholds followed by the names.

Due to the samples passing different trigger paths, there are some threshold effect expected. For example, the data from JET_20 trigger have at least a jet with $E_T > 20\ GeV$ accompanying by soft jets. The jet responsible for triggering an event could have different probability to be reconstructed as a tau object compared to the other soft jets in the same event. To study this issue, we sample the following 8 categories:

**1. trigger jet:** If an event has a jet satisfying L1/L2/L3 trigger requirement and that jet is unique, then this jet is called "trigger jet".

**2. nontrigger jet:** If an event has a jet satisfying L1/L2/L3 trigger requirement then the other jets are called "nontrigger jet". If there are two trigger jets, then both are considered as nontrigger jets. In order to define nontrigger jet, an event should have at least one trigger jet.

**3. bias jet:** Jets above L3 trigger threshold are called "bias jet".

**4. unbias jet:** Jets below L3 trigger threshold are called "unbias jet".

**5. first jet:** The first highest $E_T$ jet in an event is called "first jet".

**6. second jet:** The second highest $E_T$ jet in an event is called "second jet".

**7. third jet:** The third highest $E_T$ jet in an event is called "third jet".

**8. fourth jet:** The fourth highest $E_T$ jet in an event is called "fourth jet".

The absolute/relative $jet \rightarrow \tau$ fake rate can be defined in the same way as tau efficiency. The important one is that there is a matching procedure between jet objects and the objects as reconstructed as tau. Usually the size of jet cluster is bigger than that of tau because there is a restriction on the number of towers(less than or equal to

6) for tau candidates. Hence, the matching procedure requires that the seed tower[6] of tau candidates should be contained in the jet cluster of interest. The other procedure to obtain $jet \rightarrow \tau$ fake rate is the same as efficiency.

Fig. 4.1 shows the fake rate comparison among the different trigger paths with various samples. The difference among the trigger paths is small(less than 20%) and considered as there are not much discrepancies due to the triggers. Now we can add up all triggered samples and compare the fake rate from the differenet samples. Fig. 4.2.2 shows this comparison.

The dominant background for $jet \rightarrow \tau$ misidentification comes from multi-jet events. In this analysis the most relevant candidate jets misidentified as taus are the highest- and second-highest energy jets in the event. Therefore, we use the average of the fake rates obtained from the two leading jets. The half-difference of the fake rates obtained from the first and second leading jet is assigned as systematic error. The fake rate is parameterized in terms of ${E_T^{\tau}}^{cl}$, $E_T^{jet}$, and track multiplicity. - Figure 4.4. In order for us to have confidence with respect to this fake rate, we need to check the performance of these fake rate by applying some jet dominant samples other than jet triggered ones which are used to derive fake rates. The consistency checks are performed in Section 5.1.4 using several samples to cover various possible backgrounds. $jet \rightarrow \tau$ fake rate is small compared to other backgrounds in this analysis and it is well understood based on this study.

[6]There is no special meaning on seed tower. It depends on the clustering algorithm. However, in the sense of matching, we can require just the tower with the highest $E_T$.

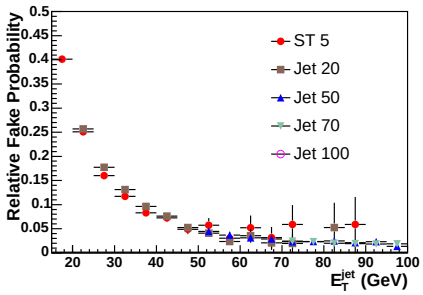


(a) trigger

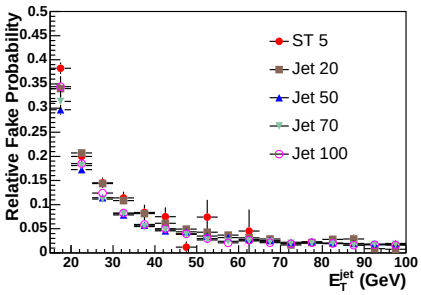


(b) nontrigger

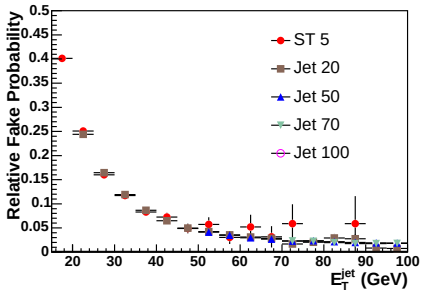


(c) bias

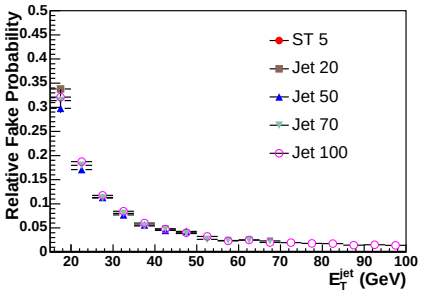


(d) unbias

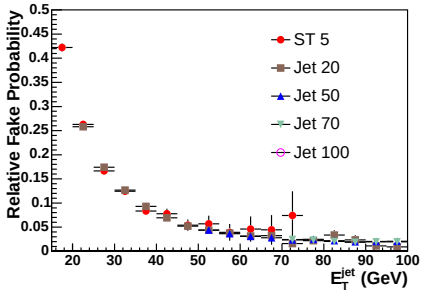


(e) first

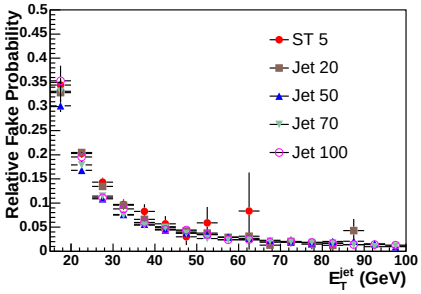


(f) second

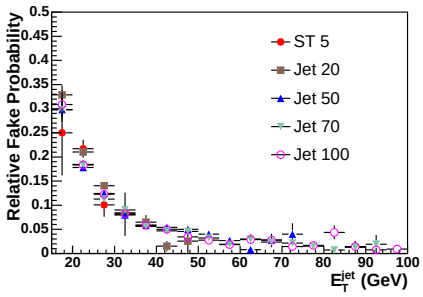


(g) third

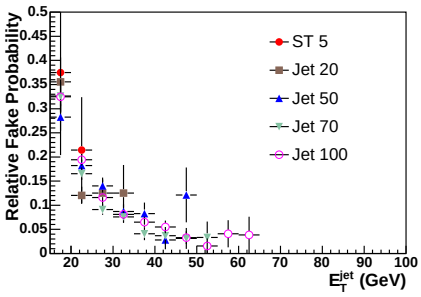


(h) fourth

Figure 4.1: *Comparison Fake rates from different samples with different trigger paths*

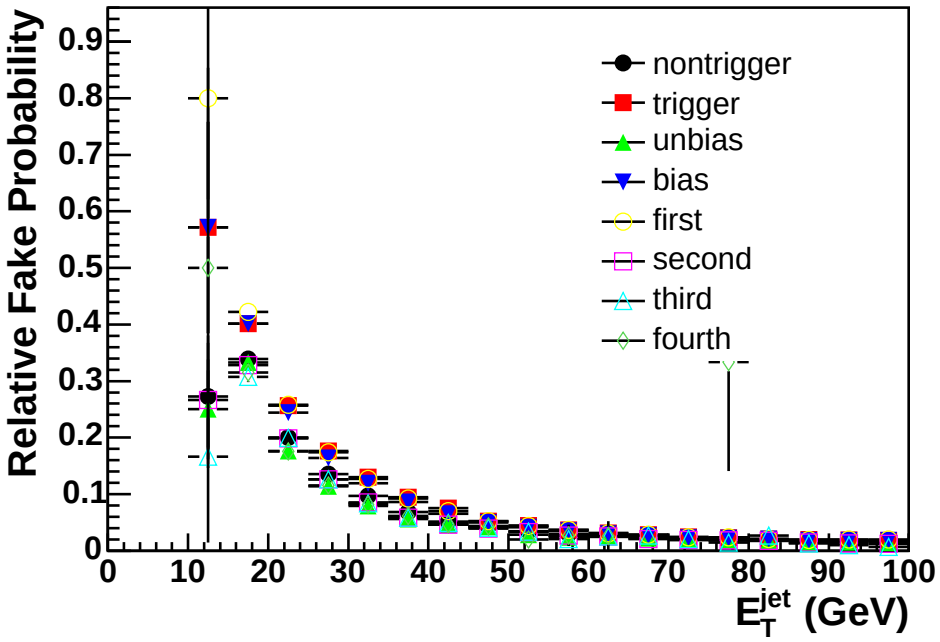


Figure 4.2: *The fake rate comparison among samples regardless of trigger paths.*

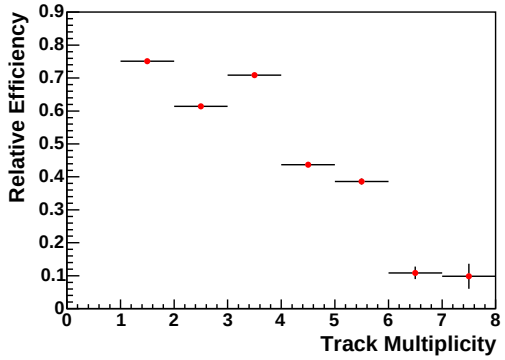


(a) Track multiplicity dependence

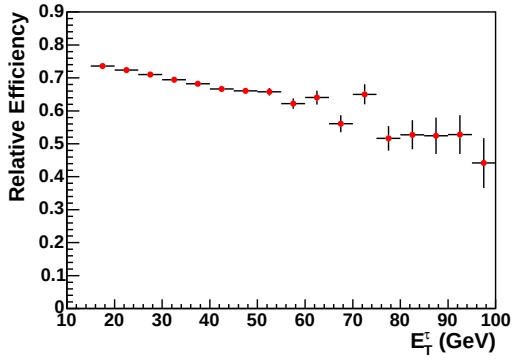


(b) Tau cluster $E_T$ dependence

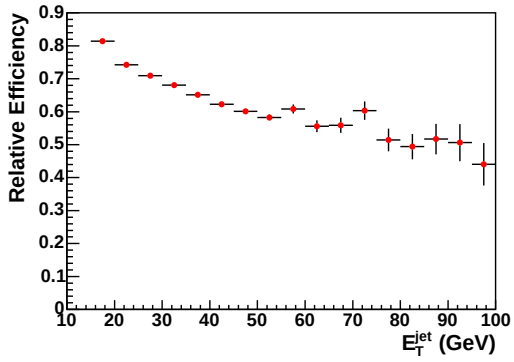


(c) Jet $E_T$ dependence

Figure 4.3: *Relative efficiency used in correction of QCD estimation.*

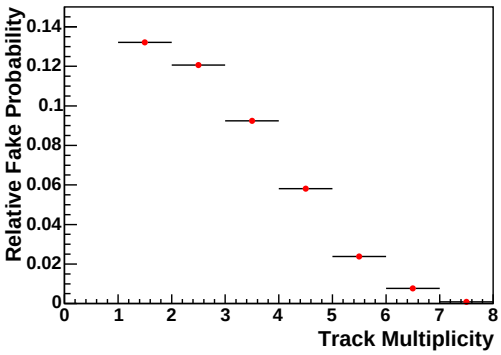


(a) Track multiplicity dependence

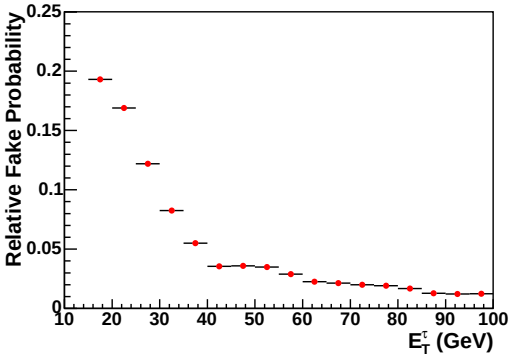


(b) Tau cluster $E_T$ dependence

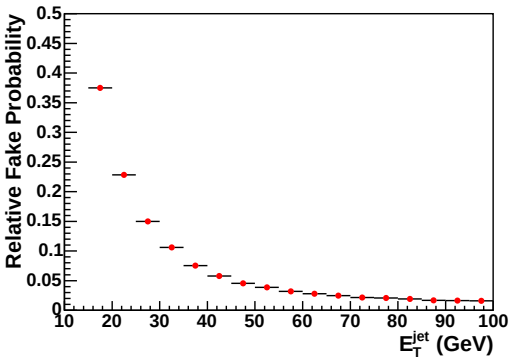


(c) Jet $E_T$ dependence

Figure 4.4: *Relative fake rate used in QCD estimation*

# Chapter 5

# Background Estimation

In this chapter, we will identify what kinds of processes could be the backgrounds of our Higgs signal and discuss the method of estimating such various backgrounds. Most of them are estimated using MC except for $jet \to \tau$ fakes (QCD backgrounds). We will especially focus on the method of QCD estimation and the verification of that method using several independent samples.

## 5.1 Background sources

The dominant backgrounds are $Z \to \tau\tau$ and estimated by MC. The second largest ones are $jet \to \tau$ fake backgrounds and estimated by "fake rate method". The backgrounds from $Z \to ee$ or $Z \to \mu\mu$ are small and estimated by MC. The others ($t\bar{t}$, Di-bosons) are negligible and also estimated by MC.

### 5.1.1 $Z \to \tau\tau$

Events containing $Z \to \tau\tau$ decays have the same final states as Higgs signal and are our irreducible source of background, even though the polarizations of the final states are different due to the boson spin being different[1]. The main separating power comes from the mass difference of $Z$ and Higgs. However, exact mass reconstruction of the ditau system is difficult due to neutrinos in the final state. We introduce a mass like variable which provides some discriminating power between $Z$ and $\phi$, (see Section 8.1). $Z \to \tau\tau$ is the largest expected background for this analysis. We do not make any attempt to suppress the $Z$ backgrounds. Any differences in di-tau mass related parameters are

[1] $\phi$ is a scalar particle with spin 0, but $Z$ is a vector particle with spin 1.

used at the time of signal extraction/ limit setting procedure. The contribution of this background is estimated using the MC simulation along with experimental results on the $Z$ production cross sections from $Z \to ll$ (lepton universality is assumed).

### 5.1.2 $Z \to ee$, $Z \to \mu\mu$

An electron or a muon can be misidentified as a hadronic tau. We use MC samples to estimate events that survive $Z \to ll$ removal event cuts. These background are highly suppressed by a further cut called $\xi'$ cut, (see Section 3.3.3).

### 5.1.3 Di-boson and $t\bar{t}$

These are small backgrounds due to small production cross sections. There are two mechanisms for these events to enter our sample: the decay state may contain the particles expected in our signal final state, e.g. $e\tau_h$, $\mu\tau_h$, etc., or an $e$ or $\mu$ could fake a hadronic tau. These backgrounds are substantially suppressed by the "$\zeta$ cut", (see Section 3.4.4). Although they are small, it is important to have them under control, because they could potentially be reconstructed as high-mass di-tau pairs. These backgrounds are estimated using MC samples and scaled to experimental production cross sections when available.

### 5.1.4 Backgrounds with $jet \to \tau$ fakes

There are three quite different processes that contribute to this group:

- $W \to l\nu + jet(s)$: where one of the jets fakes a hadronic tau
- $\gamma +$ jet: with subsequent conversion of the photon, $\gamma \to ee$ with one soft/undetected electron, resulting in reconstruction of an isolated electron; the jet fakes a hadronic tau
- $p\bar{p} \to n$ jets: one jet fakes a tau, another one fakes an $e/\mu$

There are two approaches that can be taken to estimate these backgrounds. The first is to try to estimate contributions from each source separately. The other, more

inclusive, is to apply jet $\rightarrow \tau$ fake probability to samples of events that pass event cuts but contain jets on the "tau side". We chose to use the second (so called "fake rate method") in this analysis. There is an advantage to use fake rate method which is that we don't need to identify each background source. In the fake rate method, we treat all jets as the fake candidates and apply the formula (described below) to them. This is the simplest way to treat them. Also we have performed the test to compare this fake rate method with the "estimating each source separately" method. This comparison is shown in Fig. 5.2, etc.

We use the signal sample to estimate the $jet \rightarrow \tau$ backgrounds. The relative fake rates are applied to loose tau candidates to predict the number (and distributions) of jets faking taus in the final sample.

Due to the relatively tight track isolation at trigger level and the power of our event selection cuts, the loose tau sample from which we attempt to predict $jet \rightarrow \tau$ fakes contains large fraction of real hadronic tau decays. We account for this mixture of jets and taus (even electrons and muons) through the procedure described below.

Let us start with a simplified case, and consider an initial sample passing loose tau cuts, and a final sample produced after applying the tight cuts. The number of real taus and $jet \rightarrow \tau$ fakes that survive this transition depend on the efficiency and fake rate.

Let $\hat{N}$ be the number of tau candidates passing the loose tau cuts, and $N$ the number of candidates passing the tight tau cuts. There are three sources that contribute to the observed events: real taus, leptons ($l = e, \mu$), and "jets". This is reflected in the following set of equations

$$\hat{N} = \hat{N}^{\tau} + \hat{N}^{jet} + \hat{N}^{l}$$

$$N = N^{\tau} + N^{jet} + N^{l}$$

$$N^{\tau} = \epsilon \hat{N}^{\tau}$$

$$N^{jet} = f \hat{N}^{jet},$$

where the last two expressions are the definitions of relative efficiency($\epsilon$) and fake rate($f$).

Then the number of jets faking taus can be written as

$$N^{jet} = \frac{f}{\epsilon - f}[\epsilon\hat{N} - N] - C_l,$$

where $C_l$ is a correction for $e, \mu$ contributions which is small for the considered processes and can be estimated reasonably well from MC.

If we take into account that efficiency and fake rate are actually functions of the parametrization variables (whatever they might be) and write the equations for infinitesimally small regions in parameter space, we get the same expressions for the fake tau density in terms of the event densities $\hat{n}$ and $n$ (instead of number of events)

$$n^{jet}(\Omega) = \frac{f(\Omega)}{\epsilon(\Omega) - f(\Omega)}[\epsilon(\Omega)\hat{n}(\Omega) - n(\Omega)] - c_l,$$

where $\Omega$ denotes a point in the efficiency/fake rate parametrization space. The densities $\hat{n}(\Omega)$ and $n(\Omega)$ are given by

$$\hat{n}(\Omega) = \sum_i^{\hat{N}} \delta(\Omega - \Omega_i)$$

$$n(\Omega) = \sum_i^{N} \delta(\Omega - \Omega_i).$$

To obtain the number of $jet \to \tau$ fakes in the final sample we substitute the above densities in the expression for $n^{jet}(\Omega)$ and integrate over the parameter space. The $jet \to \tau$ fake estimation reduces to sum over all loose taus which enter with weight

$$w_i^{\overline{ID}} = \frac{f(\Omega_i)\epsilon(\Omega_i)}{\epsilon(\Omega_i) - f(\Omega_i)}$$

if the candidate did not pass tight tau ID cuts, and

$$w_i^{ID} = \frac{f(\Omega_i)(\epsilon(\Omega_i) - 1)}{\epsilon(\Omega_i) - f(\Omega_i)}$$

if it did.

Using these weights we can obtain the distributions for various event variables.

## 5.2 Fake Rate Measurement and Consistency Checks

We measured the relative $jet \to \tau$ fake rate using various jet trigger samples. The relative $jet \to \tau$ fake rate is parameterized in terms of $E_T^{cl}$, $E_T^{jet}$, and track multiplicity.

We have 8 samples to determine fake rates as discussed in Section 4.2.2. Each could be good candidate for the $jet \rightarrow \tau$ background prediction. In most cases there is no clear indications on which prediction should be used. One usually takes the approach to use the average of all predictions as a central value and assign the differences with the individual predictions as systematic errors. In other cases, the highest-energy jet is not used (believed to be the source of trigger bias), and the fake rates are determined from the remaining jets. Generally, the current state of fake-rate estimation procedures (not just for taus) does not allow for a universal prescription.

In this analysis we use the highest- and second-highest energy jets in the event. The reasoning behind this choice is that the $jet \rightarrow \tau$ backgrounds in our sample are dominated by di-jet and multi-jet events. We take the average of the two estimates as central value and assign the half-difference as systematic uncertainty. The plots in Figure4.1 (e),(f) show that there is no discrepancy between the fake rates obtained with the different triggers.

The next important step is to verify that these fake rates provide adequate description of the backgrounds expected to pass our final selection. The sources contributing to the $jet \rightarrow \tau$ backgrounds were listed in Section 5.1.4. We identify three independent samples that allow testing of the fake rate predictions against the actual number of observed events. The source are examined separately to account for possible jet property differences.

We select four samples for the verification steps. The first samples contain $\gamma + jet(s)$ events. These are relevant only for $\tau_e\tau_h$ channel and represent the source of background events with an electron from non-removed conversion (probably accompanied with another very soft leg). All event cuts are applied as for signal, photon is used as replacement for the electron. The second samples contain multi-jet events and labeled as "non isolated lepton sample" because they are obtained by explicitly requiring tracks in the isolation cone around the lepton candidate $(e, \mu)$. All other cuts are applied for selecting this sample. The third and fourth samples contain $W + jet(s)$ events. These are selected from the control region indicated on Figure 5.1, which allow us to sample $W + jet(s)$ enriched events from data. Since we don't need to worry about sampling purification

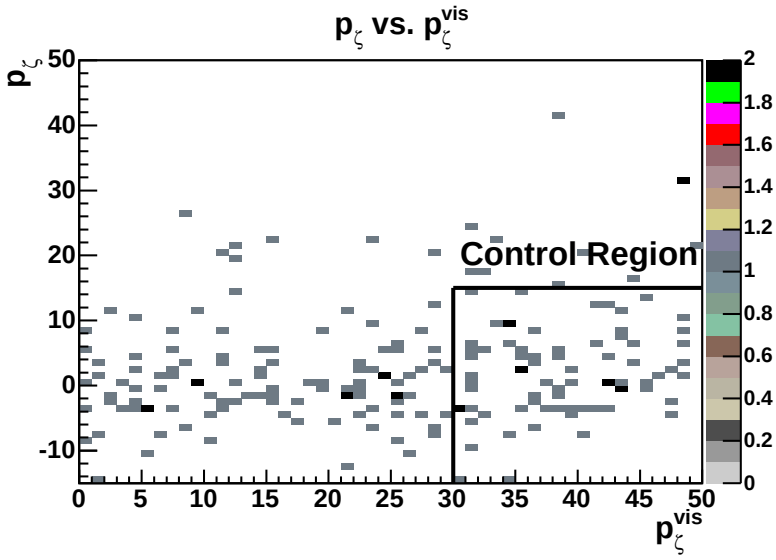


Figure 5.1: *Illustration of the control region to select $W + jet$ events in the $\zeta$ plane.*

for MC, we choose events from the signal region which is described in Section 3.4.4. Again, all event cuts are applied.

These control samples allow us to test the fake rate predictions in an environment that is compatible with the signal region. Tau contamination and backgrounds cross-contamination in these samples are minimal.

We compare the absolute prediction for number of events, the $p_T$ spectrum of observed and predicted fakes, the track multiplicity, and the the visible mass ($m_{vis}$ defined in Section 8.1) distributions as defined for signal extraction. In the latter case, $m_{vis}$ is formed using predicted (or observed) $jet \rightarrow \tau$ fake candidate, $\not{E}_T$, and the lepton (photon for the $\gamma + jet$ sample). The comparisons are presented in the following plots; Fig. 5.2, etc. We see a good agreement for all distributions and samples. As an additional test (mostly to satisfy our curiosity), we compare the predictions and observations when applying the fake rates to a MC sample of $W \rightarrow e\nu + jet(s)$. The benefit of using this MC sample is that we can get an idea about the effective mass shape in our signal region (however, $W \rightarrow e\nu + jet(s)$ is a small fraction of the fake tau backgrounds) . We were a little skeptical about the performance of the fake rate function for MC, but the

results turned out to be a pleasant surprise. The observed distributions give us confidence in the prediction of the effective mass shape for $jet \rightarrow \tau$ fakes. The predicted number of fakes taus is well contained between the upper and lower bands (of the order of 17%).

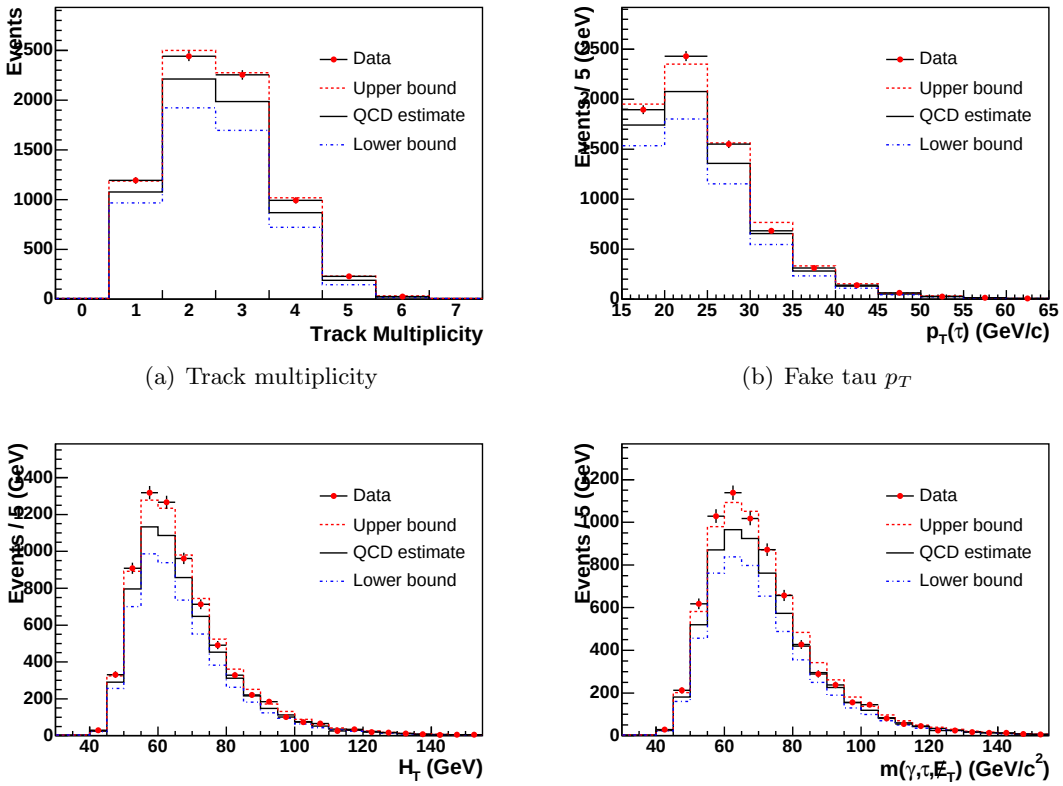


(a) Track multiplicity

(b) Fake tau $p_T$

(c) $\tilde{H}$

(d) $m_{vis}$

Figure 5.2: *Consistency checks of jet $\rightarrow \tau$ fake predictions using the $\gamma + jet$ sample. The upper and lower bounds come from using the fake rates from the highest and second-highest $E_T$ jet in the event.*

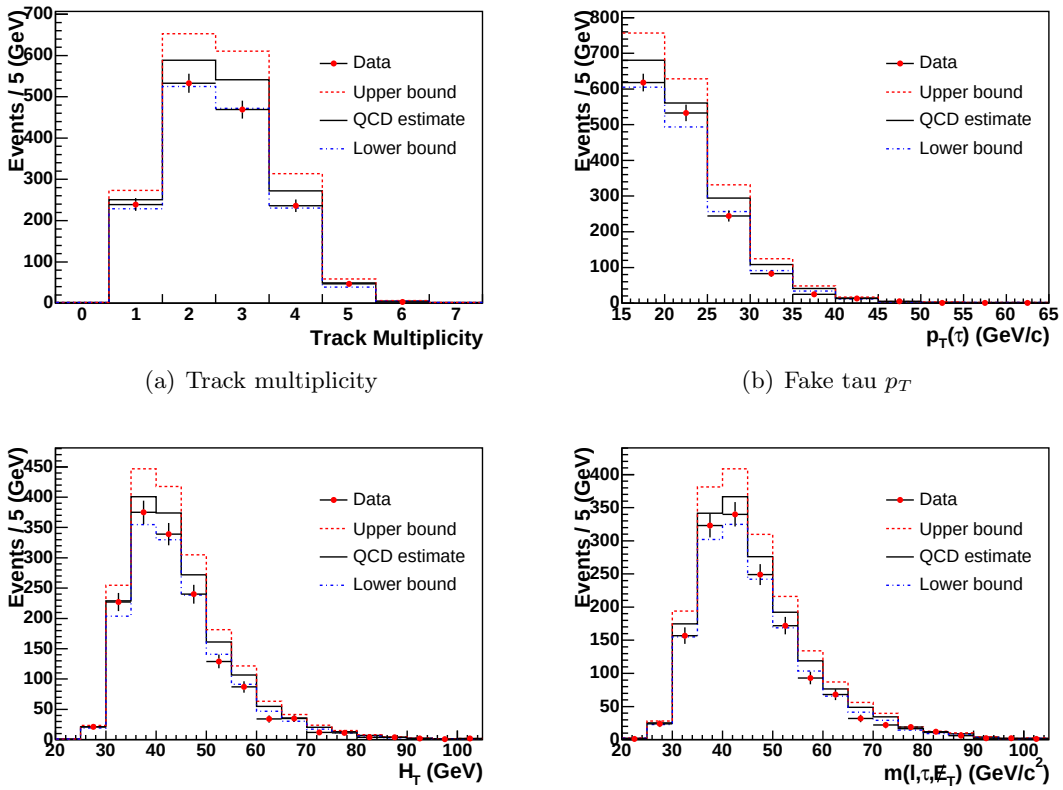


(a) Track multiplicity

(b) Fake tau $p_T$

(c) $\tilde{H}$

(d) $m_{vis}$

Figure 5.3: *Consistency checks of jet $\rightarrow \tau$ fake predictions using the non-isolated lepton sample. The upper and lower bounds come from using the fake rates from the highest and second-highest $E_T$ jet in the event.*

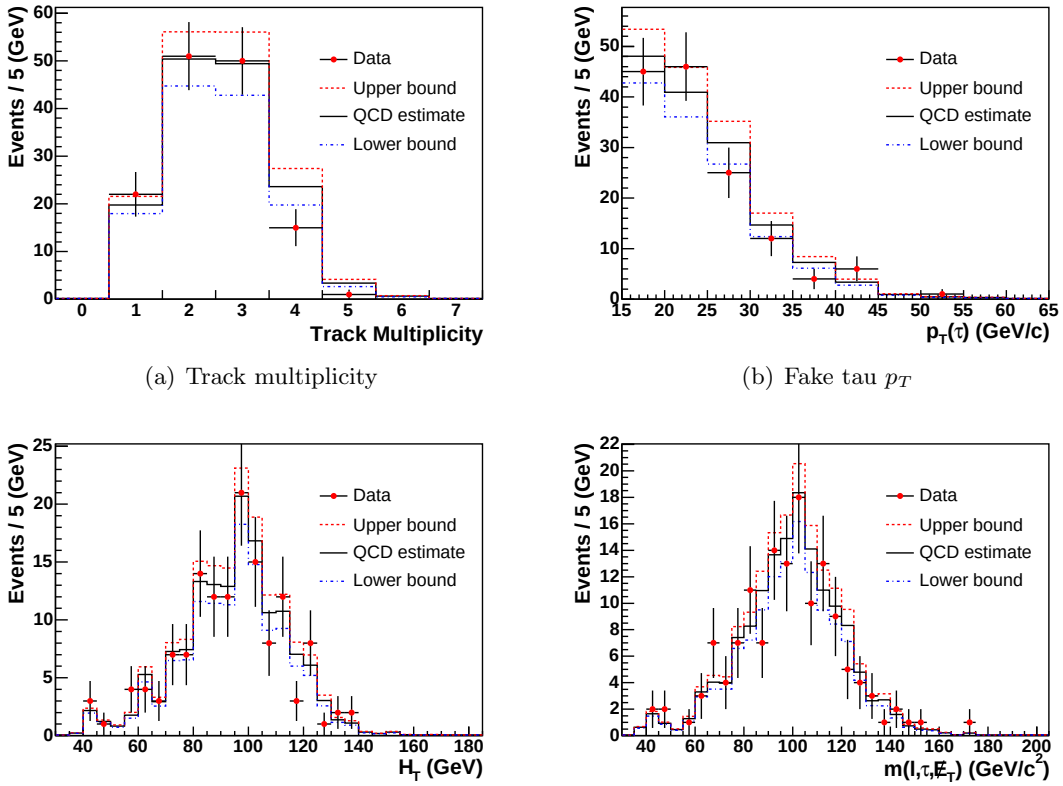


(a) Track multiplicity

(b) Fake tau $p_T$

(c) $\tilde{H}$

(d) $m_{vis}$

Figure 5.4: *Consistency checks of jet $\rightarrow \tau$ fake predictions using region dominated by $W$+jet(s). The upper and lower bounds come from using the fake rates from the highest and second-highest $E_T$ jet in the event.*

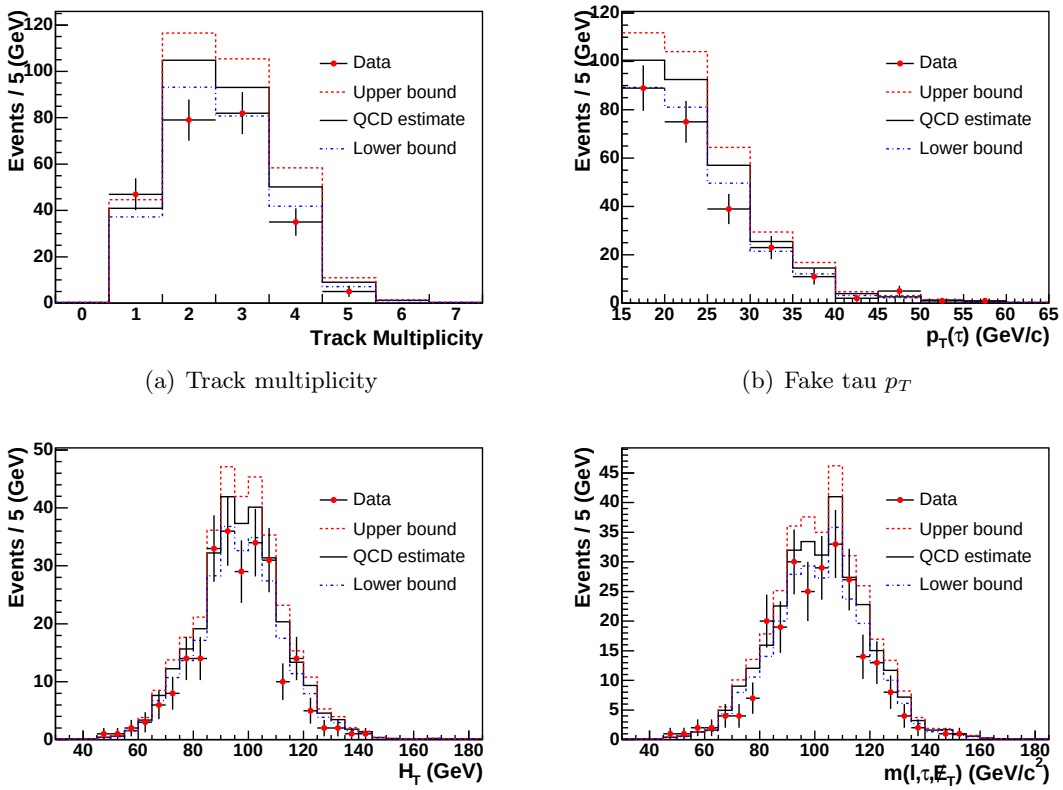


(a) Track multiplicity

(b) Fake tau $p_T$

(c) $\tilde{H}$

(d) $m_{vis}$

Figure 5.5: *Consistency checks of jet $\rightarrow \tau$ fake predictions using $W \rightarrow l\nu$ MC sample for the same region used by the data $W + jet(s)$ (shown in Figure 5.4). The MC is not scaled to luminosity. The upper and lower bounds come from using the fake rates from the highest and second-highest $E_T$ jet in the event.*

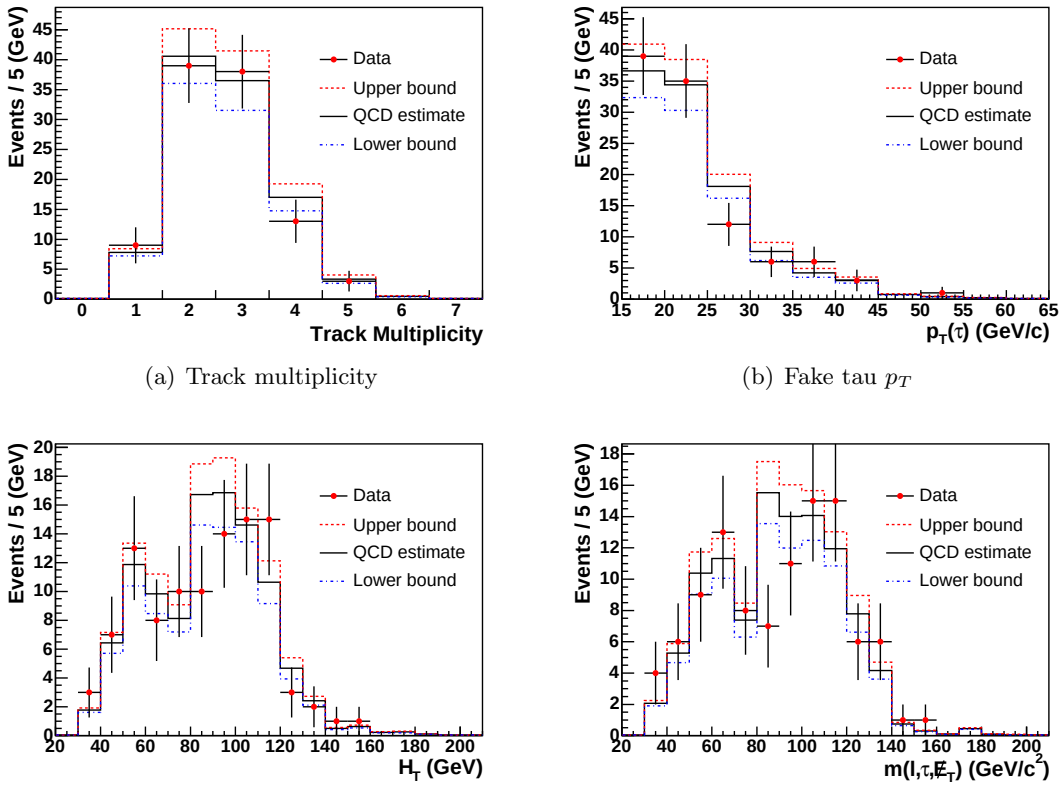


(a) Track multiplicity

(b) Fake tau $p_T$

(c) $\tilde{H}$

(d) $m_{vis}$

Figure 5.6: *Consistency checks of jet $\rightarrow \tau$ fake predictions using $W \rightarrow l\nu$ MC sample. The events pass* **all** *the event selection cuts (signal region). The MC is not scaled to luminosity. The upper and lower bounds come from using the fake rates from the highest and second-highest $E_T$ jet in the event.*

# Chapter 6

# Systematic Uncertainty

There are several sources of systematic uncertainties affecting this analysis: Trigger efficiency, Particle Identification, Background estimation, PDF's used in MC simulation, and Luminosity.

The systematics due to trigger efficiency is mostly related with sampling. For example, if we want to measure electron trigger efficiency, we have to make sure that samples should contain pure electrons. In this case, we may select an electron from $Z \rightarrow ee$. This is just a simple example. For tau case, the situation is worse. We don't have any pure samples for it. $W \rightarrow \tau\nu$ would be good candidate, but unfortunately its trigger condition is much tighter than that of our interesting trigger. Hence, we use generic pion track to measure tau trigger efficiency. The uncertainty due to trigger efficiency is summarized at Table 3.2.

We rely on MC simulation to model particle interactions in the detector and to estimate signal efficiency and most of the backgrounds except $jet \rightarrow \tau$ background. We account for possible differences between data and MC particle ID efficiencies through the introduction of scaling factors applied to MC. These scale factors account for residual deficiencies in modeling of the detectors. The uncertainties in determining these factors are assigned as systematic errors of particle reconstruction and ID efficiency. Tau ID uncertainties are discussed in Section 6.1. For muons and electrons we use the uncertainties suggested by CDF collaboration.

Deficiencies in the simulation of calorimeter response to jets lead to differences in measured $\not\!\!E_T$. These are accounted for by the MC-specific jet energy corrections. To estimate the systematic uncertainties in these corrections, we vary the jet corrections

| Parameter | Error(%) | applies to: |
|---|---|---|
| $e$ ID | 1.3 | $e$ |
| $\mu$ ID (CMUP) | 4.4 | $\mu$ |
| $\mu$ ID (CMX) | 4.6 | $\mu$ |
| $\tau$ ID | 3.5 | $\tau_h$ |
| event cuts | 1.8 | all |
| $jet \rightarrow \tau$ fake rate | 20.0 | QCD bg |
| $\sigma \times \mathcal{B}(Z \rightarrow ll)$ | 2.1 | Z bg's |
| PDFs ($Z$) | 3.0 | Z bg's |
| PDFs ($Higgs$) | 5.7 | signal |
| $e$ trig | 1.9 | $e$ |
| $\mu(CMU)$ trig | 1.0 | $\mu$ |
| $\mu(CMX)$ trig | 1.0 | $\mu$ |
| "track" (tau) trig | 1.0 | $\tau_h$ |
| Luminosity | 6.0 | all (-QCD) |

Table 6.1: *Systematic uncertainties by source.*

applied to the MC by reasonable amount and observe the effect on measured jet energies. Energy uncertainty for tau and electron (Section 6.1) also has a small effect on acceptance, 1.8%.

The systematics related to background estimation are determined by uncertainties in cross-sections for processes estimated using MC, and fake rates for $jet \rightarrow \tau$ fakes (plus statistical errors on the estimates).

The systematic uncertainties in acceptance associated with the lack of precise knowledge of the Parton Distribution Functions (PDFs) are different for the $Z$ backgrounds and the $Higgs$ signals. The former are estimated to be less than 3%, while the latter are substantially higher: of the order of 5.7%. Discussion of the effect of PDF uncertainties on Higgs acceptance is given in Section 6.2.

We use the standard luminosity uncertainty of 6%.

Trigger systematics are taken from the trigger studies notes listed in Table 3.2. Additional uncertainty due to the XFT efficiency adjustment of 0.9% is added in quadrature in the electron case (see Section 6.3).

Table 6.1 summarizes the systematic uncertainties. The correlations between these uncertainties are taken into account when extracting the limits.

## 6.1 Tau energy scale

Tau detection efficiency is affected by the requirements imposed on tracks and $\pi^0$'s in the isolation annulus. Possible difference between data and MC can appear due to deficiency in the simulation of the underlying event and multiple interactions. To compare data and MC we inspect the isolation of muons from $Z \to \mu\mu$ events with respect to reconstructed tracks and $\pi^0 s$ [1] .

For this comparison, one can simply randomly select regions in the detector and compare data and MC. We have chosen to use $Z$ events because they simulate the environment for our signal selection. Due to the small energy deposition by muons, $Z \to \mu\mu$ provides clean environment for $\pi^0$ isolation studies. We look at the efficiency of our track and $\pi^0$ isolation cuts in isolation annulus $10^o - 30^o$ (measured from the direction of the muon). Recall that in tau selection in trigger this annulus is used to reject jets. The ratio of the efficiency for data and MC was found to be $\epsilon^{iso}_{data}/\epsilon^{iso}_{MC} = 0.997 \pm 0.008$.

The tau side of the "lepton+track" triggers has a track isolation requirement at L3 that rejects candidates if there is a track with $p_T > 1.5$ GeV with $|z_0 - z_0^{seed}| < 15$ cm and $0.17 < \Delta R < 0.52$. Using the same sample, we find $\epsilon^{L3\ iso}_{data}/\epsilon^{L3\ iso}_{MC} = 0.999 \pm 0.012$.

In the past, the effect of multiple interactions was not explicitly taken into account. Parametrization of the efficiency in terms of vertex multiplicity is a flexible way of taking it into account. In calculating the data/MC efficiency ratios we used the observed vertex multiplicity in our data sample:

$$\frac{\epsilon^{iso}_{data}}{\epsilon^{iso}_{MC}} = \sum_i \frac{n_i}{n_{tot}} \frac{\epsilon(n_i)^{iso}_{data}}{\epsilon(n_i)^{iso}_{MC}},$$

where the sum goes over the number of vertexes, and $n_i$ and $n_{tot}$ are the number of events with $i$ number of vertexes, and the total number of events, respectively.

Tracks with $p_T > 1.0$ GeV from the underlying event and multiple interactions can contribute to track "multiplicity migration" if they are contained in the signal cone. We compare the number of additional tracks in a $10^o$ cone with respect to the

[1] Similar approach (using $Z \to ee$) has been previously applied in the study of tau efficiency in the first $72pb^{-1}$ [32].

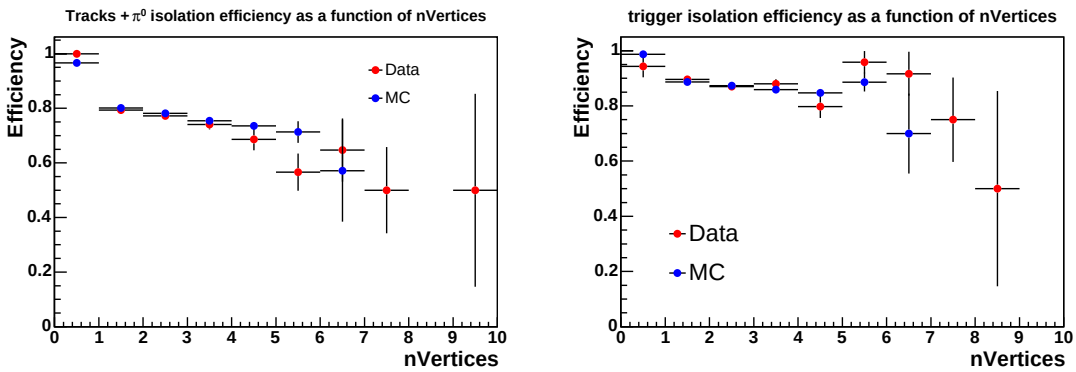


(a) L3 track isolation requirement

(b) Track and $\pi^0$ $\tau$ ID isolation

Figure 6.1: *Efficiency of isolation requirements for data and MC vs number of primary vertexes in the event.*

muon direction and find an average of $0.025 \pm 0.013$ additional tracks in the data, and $0.027 \pm 0.003$ in the MC. This corresponds to an uncertainty in tau selection efficiency due to "multiplicity migration" of 1.3%.

Hadronic scale uncertainty in the MC affects tau acceptance through the requirement on minimum tau cluster energy, tau seed tower $E_T$ threshold, and the $\xi'$ cut. We vary the hadronic energy by 6% and observe change in efficiency of 2%.

The effect of the cut on the mass of the hadronic tau decay products $m(trks{+}\pi^0\text{'s}) <$ 1.8 GeV on data and MC is examined using a sample of taus from W decays. The data is selected with the "tau+MET" trigger (dataset $etau0d$). Tau ID is the same as for the Higgs search. To suppress multi-jet backgrounds we impose tight event cuts: $\not{E}_T > 25$ GeV, no extra jets with $E_T > 5$ GeV. Backgrounds from EW processes are estimated using MC samples. The number of residual $jet \rightarrow \tau$ fakes is obtained by performing a fraction fit of the track multiplicity distribution with templates from MC and jet samples.

Figure 6.2 shows the track multiplicity and mass distributions for data, $W \rightarrow \tau\nu$ MC, and the contributing backgrounds. The mass cut efficiency is $0.968 \pm 0.006$ for data and $0.953 \pm 0.008$ in the MC. From here we determine $\epsilon^{m\ cut}_{data}/\epsilon^{m\ cut}_{MC} = 1.016 \pm 0.010$.

The determination of the tau energy scale is a challenging undertaking.

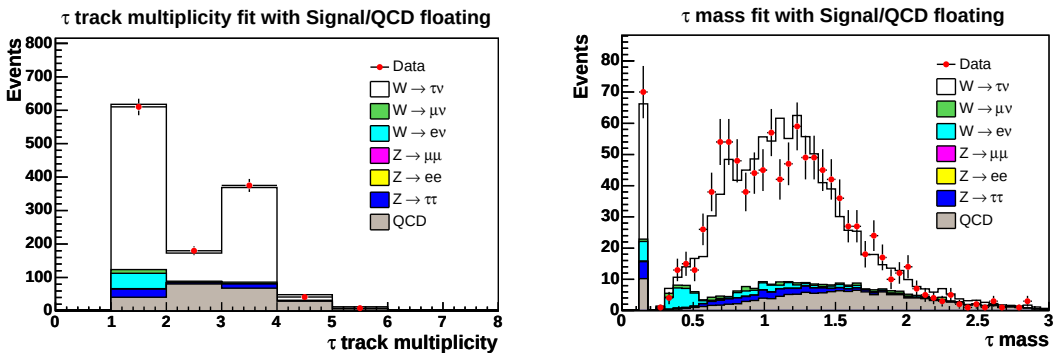


(a) Track multiplicity of tau candidates

(b) Mass of the hadronic decay products

Figure 6.2: *Track multiplicity and $m(trks + \pi^0\text{'s})$ for tau candidates. Contributions from $W \to \tau\nu$ and various backgrounds are included as shown in the Legend.*

In this case, however, the absolute energy scale (although desirable) is not absolutely needed. What is important is to have the data/MC agree on the prediction of the reconstructed $p_T(trks + \pi^0$ 's). If we do not attempt to extract absolute measurements of quantities such as Z or Higgs mass, absolute energy scales (and the associated uncertainties) do not have large impact. What really matters is the relative data/MC energy scale. This simplifies the problem, but does not eliminate all hurdles. The missing energy due to neutrinos still prevent us from making comparisons of distributions produced on tau-by-tau basis.

Here we use a comparison of the data and MC $p_T$ distributions of reconstructed taus in $W \to \tau\nu$ decays from independent samples[2]. To avoid trigger effects, we applied a higher threshold for the tau seed track ($p_T^{seedtrk} > 10$ GeV). As can be seen in Figure 7.2, the fraction of selected taus for the Higgs search with $p_T^{seedtrk} < 10$ GeV is small.

Figure 6.3 shows the observed and predicted $p_T$ spectra of tau candidates. The consistency of the shapes is checked using a Kolmogorov-Smirnov (KS) test. We vary the energy scale of the MC, and for each shifted energy scale plot the KS probability. The results are presented in Figure 6.4. We see no indication of significant energy scale difference between observation and prediction.

The sensitivity of the KS test is determined by pseudo-experiments. We generated

[2]For the selection of $W \to \tau\nu$, we use data selected from TAU_MET trigger

10,000 templates of the $p_T$ distribution using the nominal MC and background samples. We then performed the KS tests with shifted distributions. Figure 6.5 shows the most probable shift for each test. The distribution has a Gaussian shape with $\sigma = 0.37\%$. Since the QCD($jet \rightarrow \tau$ fake background) component is taken from data, it does not need possible data/MC energy scale. However, since the amount of QCD in our sample is uncertain, in principle we must adjust our KS tests for the presence of QCD. In practice, we account for possible effects from the estimated QCD background by varying the contribution by $\pm 1, 2\sigma$ and using shapes from multi-jet, di-jet, $\gamma$+jet, conversion+jet samples. Since the QCD background is small less than 10%, the impact is small. All these variations affect the shift by $< 0.5\%$. We add this in quadrature with 0.4% (sensitivity of the KS tests) and assign total uncertainty on data/MC tau energy scale of 0.6%.

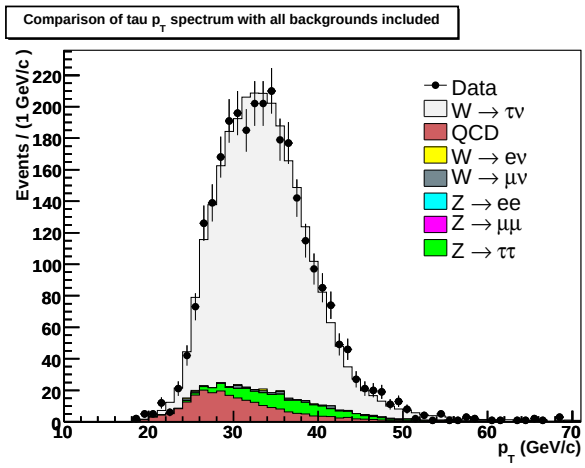


Figure 6.3: *$p_T$ spectrum of taus from W decays.*

## 6.2 Parton distribution function

The Parton Distribution Functions (PDFs) are not precisely known, and this uncertainty leads to a corresponding uncertainty in the predicted cross sections, as well as the acceptance. We are mainly interested in how the acceptance varies with varying PDFs. The proper way to carry out this study — generating separate sets of Monte

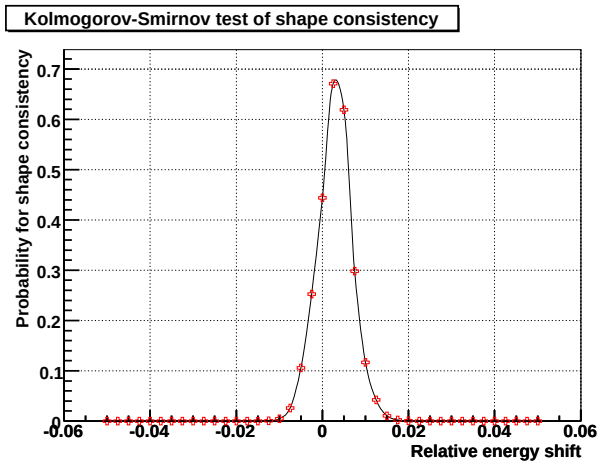


Figure 6.4: *Kolmogorov-Smirnov tests of the observed tau $p_T$ spectrum and simulated shifts in the MC.*

Carlo events for each PDF set one wanted to investigate – would be prohibitive. Instead, we follow the prescription advocated by the Top Quark group [3] and reweight the same set of generated events with different PDF sets, and observe the cross section and acceptance changes.

We generated the processes $gg \rightarrow A$ and $b\bar{b} \rightarrow A$ separately. However, since the PDF systematics for the two processes are similar – $b\bar{b}$ pairs come from gluon splitting – we can simply take the mean.

We use Pythia 6.216 for all our Monte Carlo generation, which uses CTEQ5L PDFs. We investigated 41 CTEQ6 eigenvectors.

We calculate the acceptance by requiring the visible decay products of the $\tau$ to have $|\eta| < 1.1$, and then require the sum of energies of these particles to be greater than 10 GeV.

We calculate two components of the PDF acceptance systematic: the difference between CTEQ5L (used by Pythia) and CTEQ6M, and the difference between CTEQ6M and the 41 CTEQ6 eigenvectors. The former are summarized in table 6.2. The differences get slightly larger with A mass. However, for this study we take an average of

[3] Stephen Miller, private communication

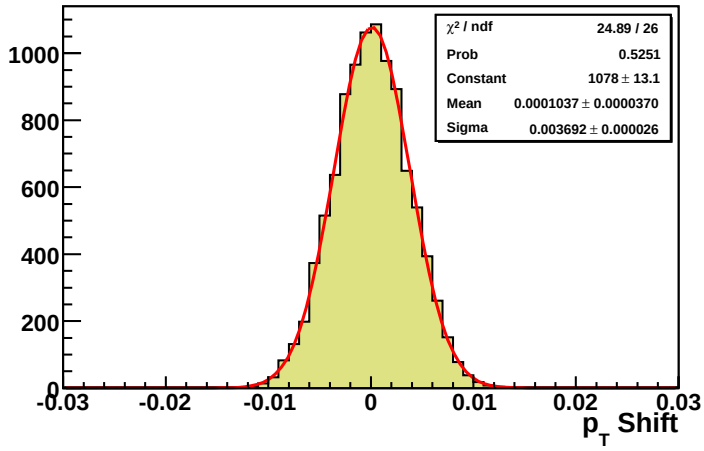


Figure 6.5: *Distributions of most probable shifts determined from 10k pseudo-experiments.*

these values, and get 3.1% as the uncertainty for CTEQ6M to CTEQ5L.

| Mass | $gg \to A$ | $b\bar{b} \to A$ |
|---|---|---|
| 115 | 1.7 | 2.9 |
| 140 | 2.2 | 2.7 |
| 160 | 3.0 | 4.2 |
| 180 | 3.5 | 4.4 |

Table 6.2: *Difference in acceptance between CTEQ5L and CTEQ6M (%).*

The largest contribution to the PDF acceptance uncertainty comes from the CTEQ6 eigenvector ± 15, which control the gluon content of the proton. Figure 6.2 shows the acceptance ratios for CTEQ6M vs. the various eigenvectors. The largest excursions, approximately 4.5%, are in bins 35, 36, which correspond to the eigenvectors ± 15. We average the excursions (positive and negative) for the various mass values and production mechanisms and derive 4.8% for the uncertainty due to eigenvector 15 of CTEQ6. The uncertainty due to other eigenvectors is negligible on this scale. We get 3.1% from the CTEQ5L-6M difference and 4.8% from the CTEQ6 eigenvector difference and add them in quadrature to arrive at a total PDF uncertainty of 5.7%.

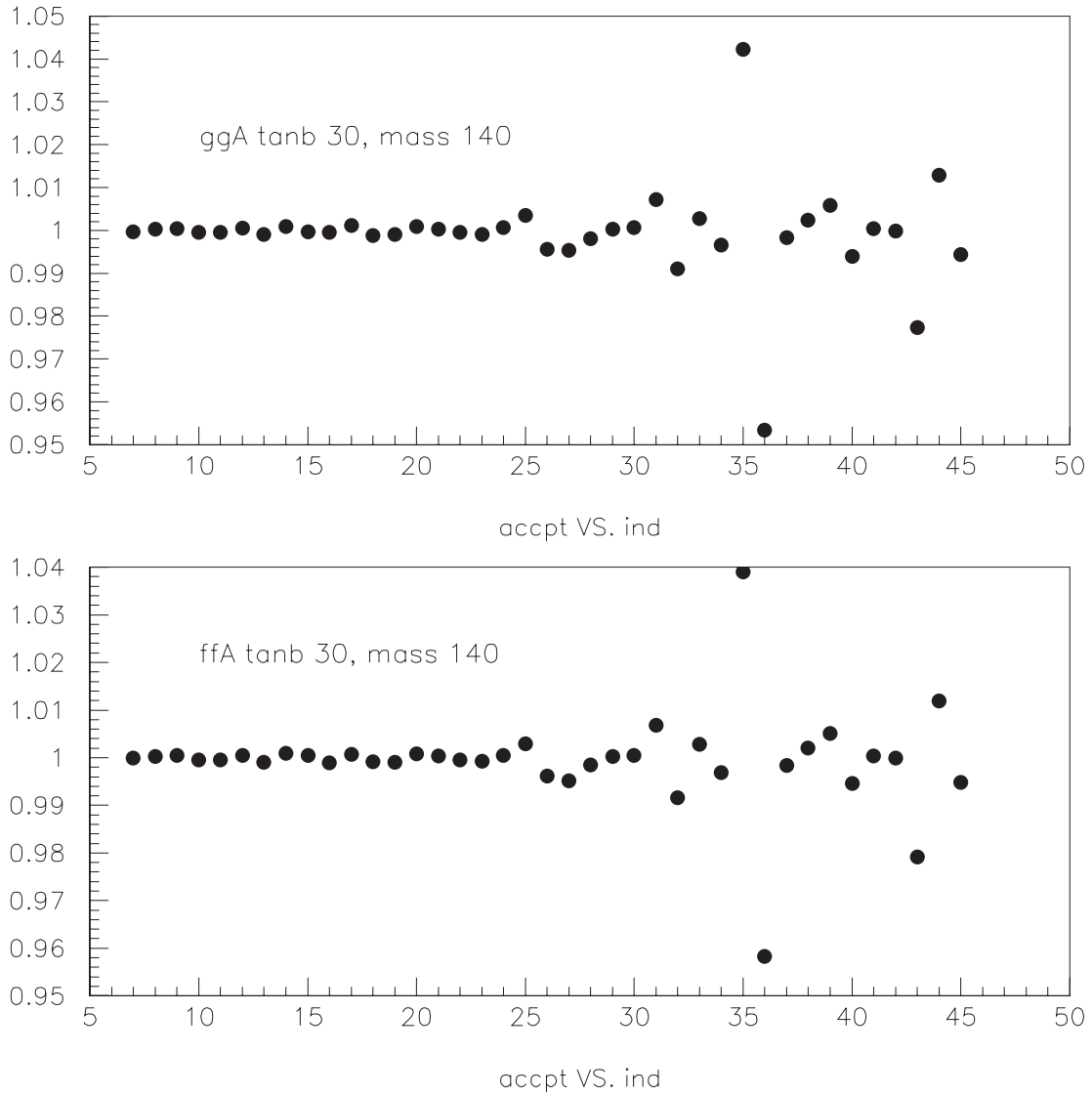


Figure 6.6: *Acceptance variations comparing for the 41 CTEQ6 eigenvectors. The events are* $A \to \tau\tau$ *mass=140 GeV/*$c^2$ *with a* $\tan\beta$ *= 30. Bins 35,36 correspond to CTEQ6 eigenvectors* $\pm$ *15, which control the gluon content.*

## 6.3 XFT rescale

The requirements for the XFT part of the trigger changed slightly during data taking. A detailed report of the changes and the their effects on the efficiencies can be found in CDF Note 6234. In this note, the data is broken down into 6 separate periods, and the XFT efficiency is calculated separately for each period.

The trigger efficiency used in this analysis is documented in CDF note 6257, 6358. The data used in these studies came from Periods 1 - 3 as defined in note 6234. Therefore, we do not (re)correct for the XFT efficiency in these ranges.

From Table 9 in CDF note 6234, we determine that the XFT efficiency for Periods 1 - 3 was 97.0 %. We correct as follows:

- Periods 1,2,3: 1.0 (by definition)
- Period 4: 96.4/97.0 = 99.4
- Period 5: 96.0/97.0 = 99.0
- Period 6: 94.7/97.0 = 97.6

The error incurred in calculating the XFT scale factors are small. The majority of the XFT changes, including going from requiring 3 superlayers to 4, and 10 hits to 11, as well as the turning off of a section of one superlayer, all occurred within Periods 1 - 3.

As a result, we apply additional scaling factor of $0.987 \pm 0.009$ on top of the measured XFT trigger efficiency.

# Chapter 7

# Observed Events

Now we compare all known backgrounds with real data and search for the Higgs signals. We can confirm that our data sample is primarily ditau events by observing the track multiplicity of the hadronic tau candidate. Figure 7.1 shows the nice enhancement in the first and third track bin. These are the only plots where track multiplicity ($N_{trk} = 1, 3$) and opposite charge ($Q_{\tau_l} Q_{\tau_h} = -1$) requirements are not applied. Subsequent plots show distributions for events with track multiplicity and opposite charge requirement applied. The plots show data along with expected backgrounds as indicated on the plots. The electron and muon channels are plotted separately. This presentation scheme is used in all plots. The MC samples are normalized to the respective measured cross-sections. Trigger efficiency and data/MC scaling factors accounting for differences between data and MC particle reconstruction and ID are included. The $jet \rightarrow \tau$ fakes are determined using the described procedure with no additional scaling or adjustments.

The predicted backgrounds and observed events in data summarized in individual channels are shown in Table 7.1. The combined results are shown in Table 7.2.

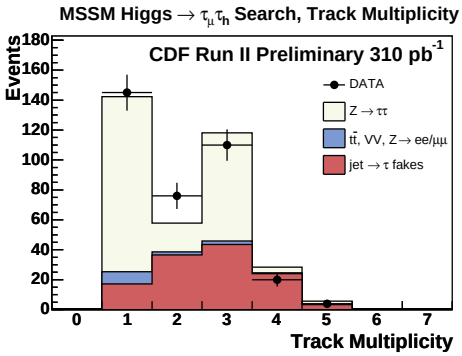


(a) $\tau_\mu \tau_h$

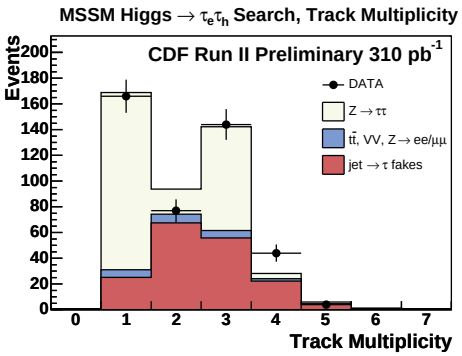


(b) $\tau_e \tau_h$

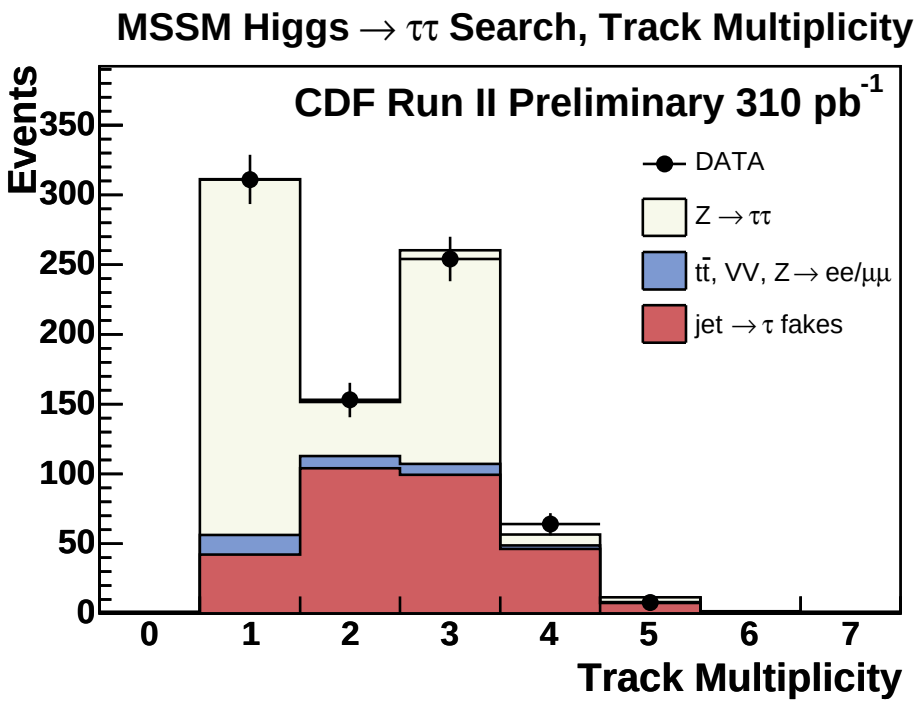


(c) $\tau_\mu \tau_h + \tau_e \tau_h$

Figure 7.1: *Track multiplicity for tau candidates in the $\tau_\mu \tau_h$ and $\tau_e \tau_h$ channels.*

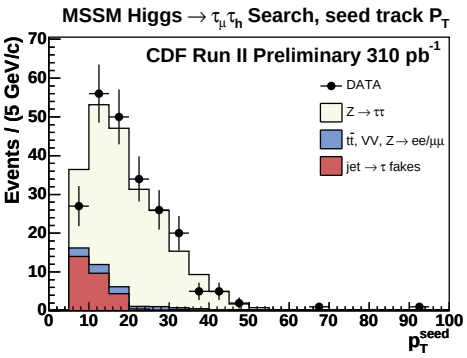


(a) $\tau_\mu\tau_h$

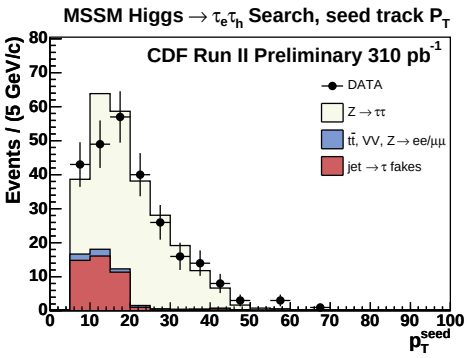


(b) $\tau_e\tau_h$

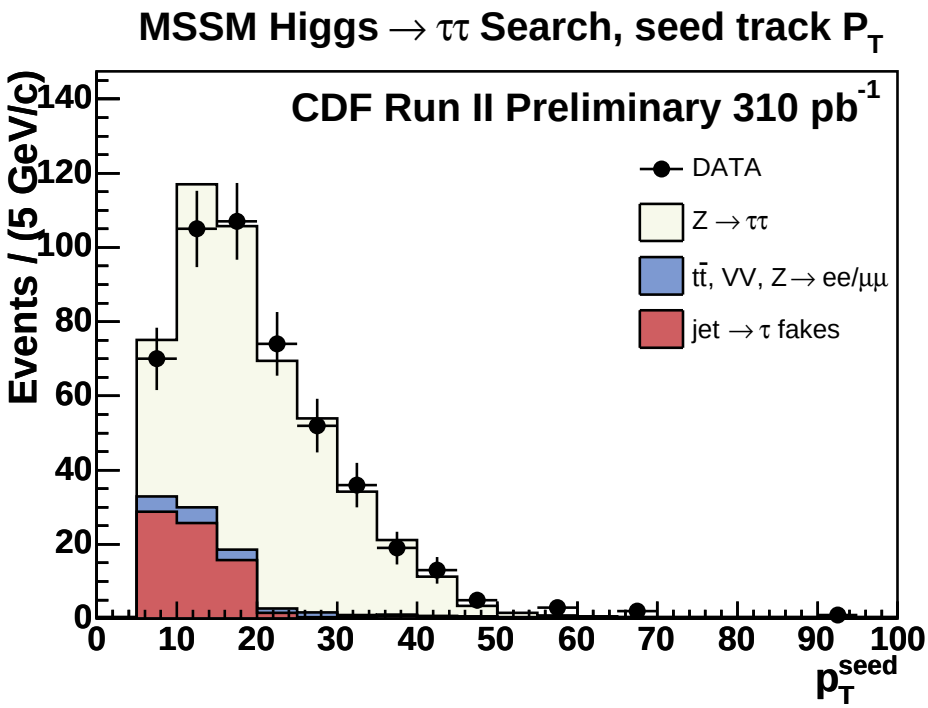


(c) $\tau_\mu\tau_h + \tau_e\tau_h$

Figure 7.2: *Seed track$p_T$ for tau candidates in the $\tau_\mu\tau_h$ and $\tau_e\tau_h$ channels.*

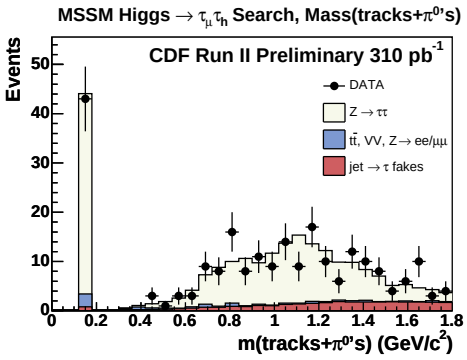


(a) $\tau_\mu\tau_h$

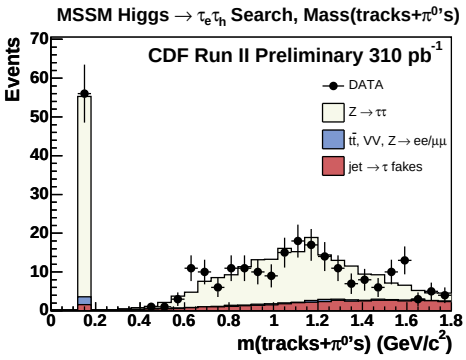


(b) $\tau_e\tau_h$

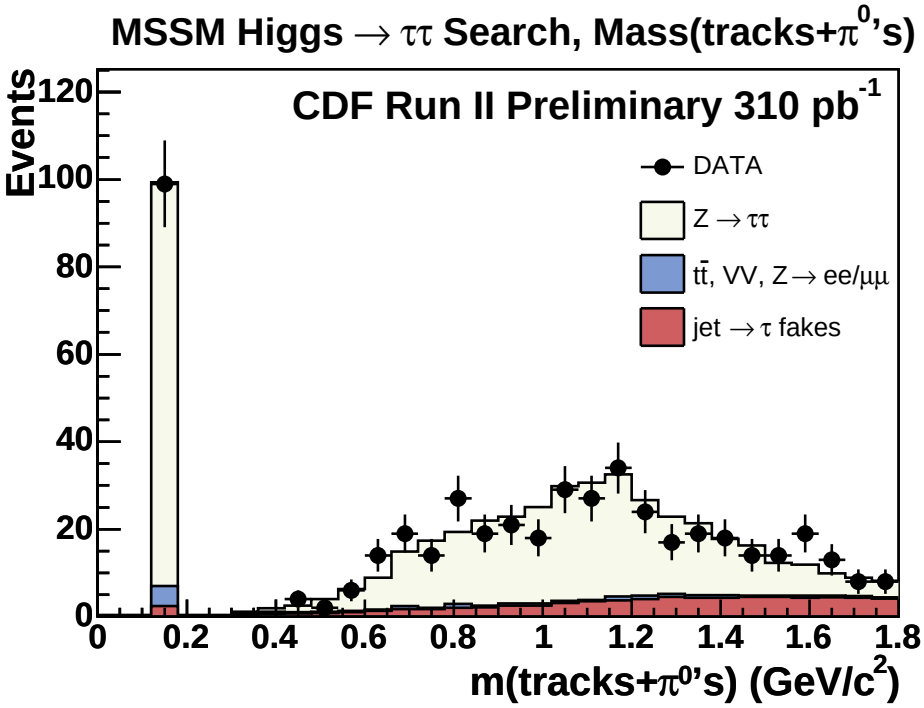


(c) $\tau_\mu\tau_h + \tau_e\tau_h$

Figure 7.3: *Hadronic system mass for tau candidates in the $\tau_\mu\tau_h$ and $\tau_e\tau_h$ channels.*

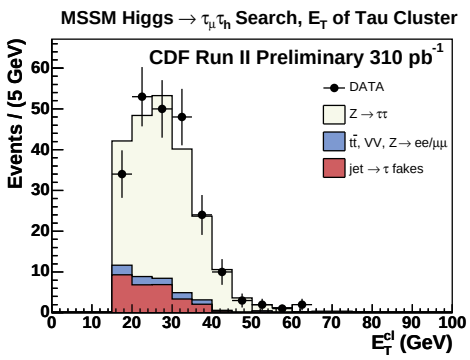


(a) $\tau_\mu\tau_h$

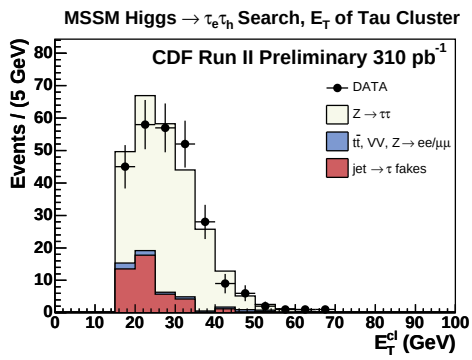


(b) $\tau_e\tau_h$

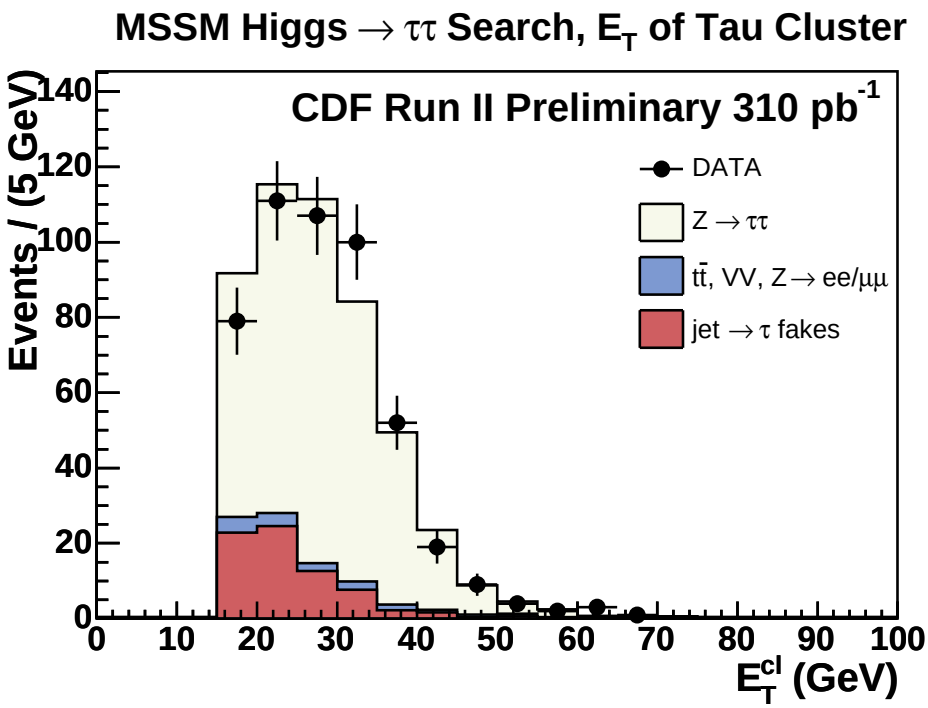


(c) $\tau_\mu\tau_h + \tau_e\tau_h$

Figure 7.4: *Tau cluster energy for tau candidates in the $\tau_\mu\tau_h$ and $\tau_e\tau_h$ channels.*

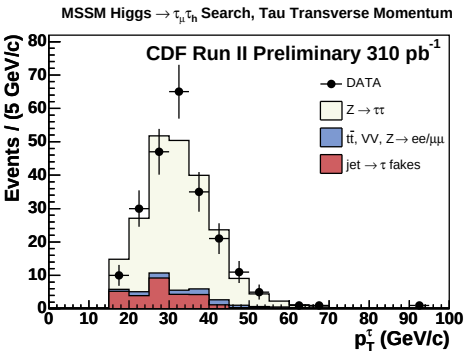


(a) $\tau_\mu \tau_h$

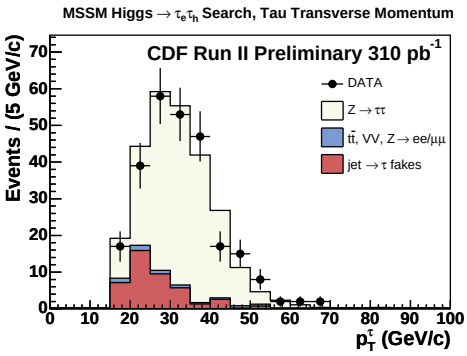


(b) $\tau_e \tau_h$

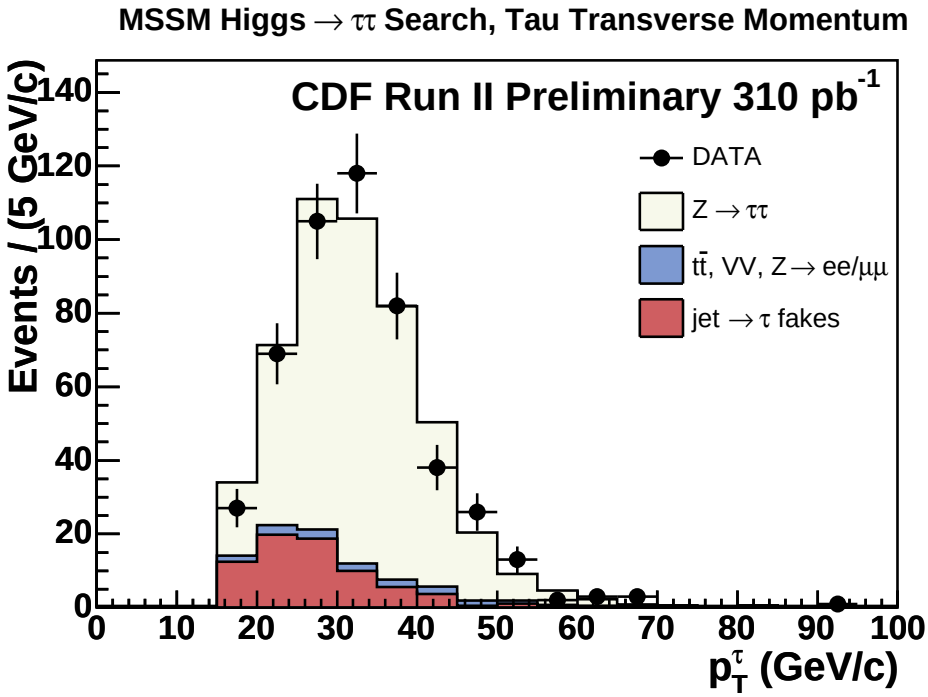


(c) $\tau_\mu \tau_h + \tau_e \tau_h$

Figure 7.5: *Transverse momentum of tau candidates in the $\tau_\mu \tau_h$ and $\tau_e \tau_h$ channels.*

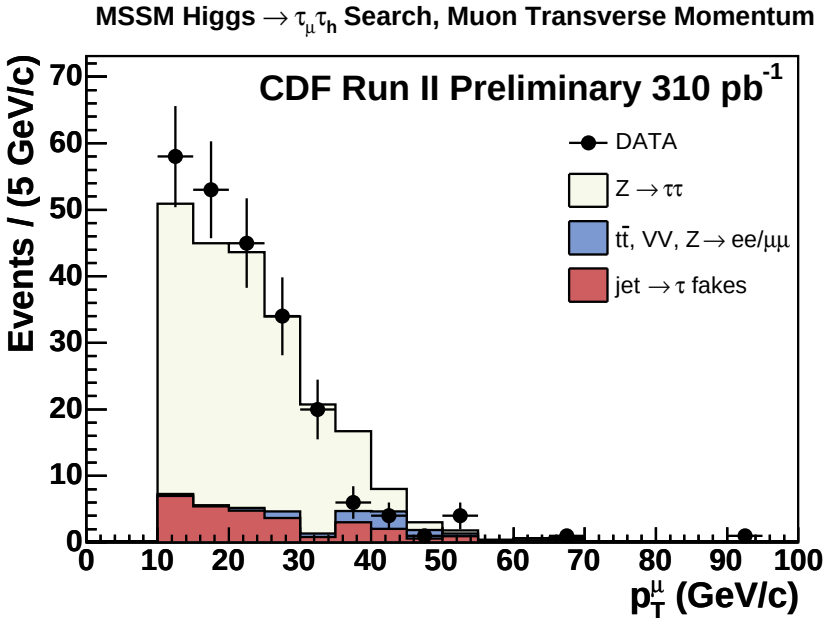


(a) $\tau_\mu \tau_h$

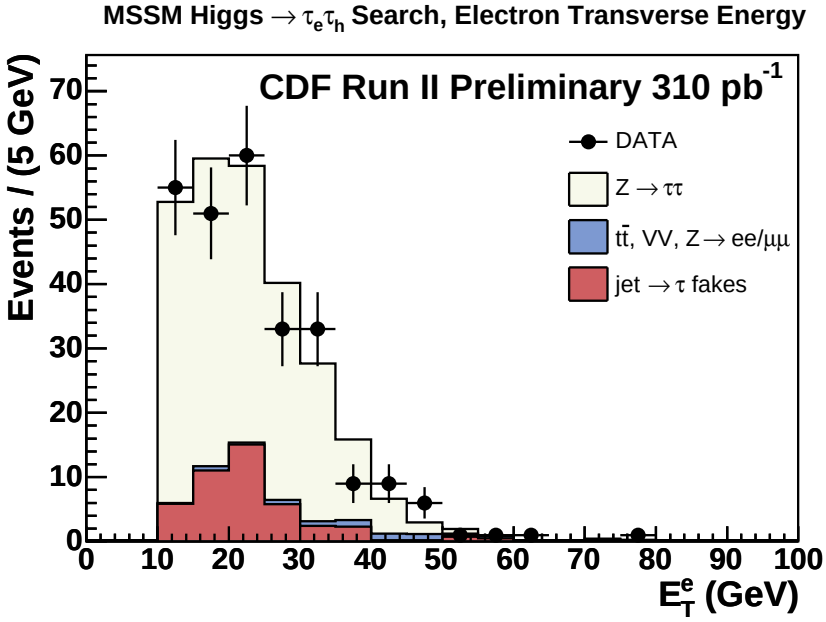


(b) $\tau_e \tau_h$

Figure 7.6: *Transverse momentum of the lepton (e or $\mu$) candidates in the $\tau_\mu \tau_h$ and $\tau_e \tau_h$ channels.*

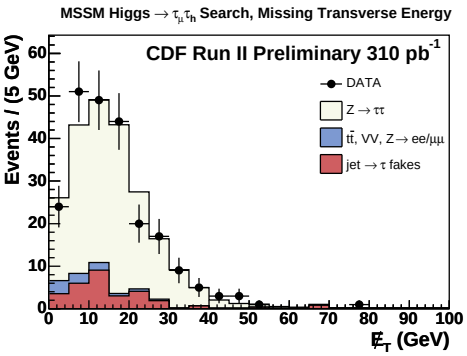


(a) $\tau_\mu\tau_h$

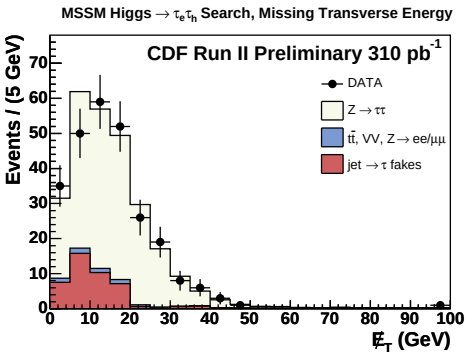


(b) $\tau_e\tau_h$

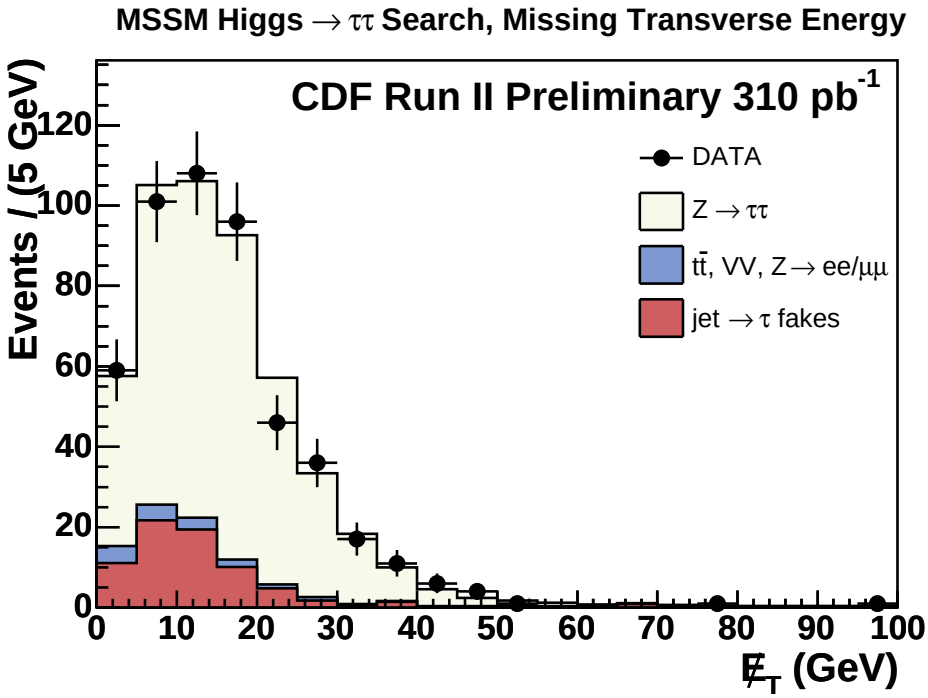


(c) $\tau_\mu\tau_h + \tau_e\tau_h$

Figure 7.7: *Missing transverse energy in the event in the $\tau_\mu\tau_h$ and $\tau_e\tau_h$ channels.*

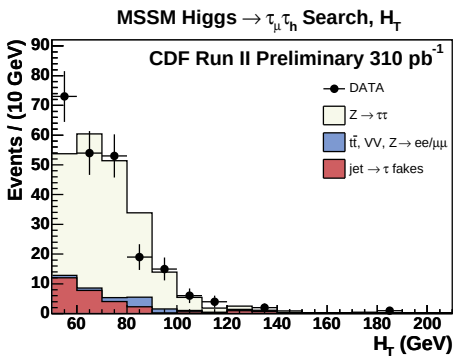


(a) $\tau_\mu \tau_h$

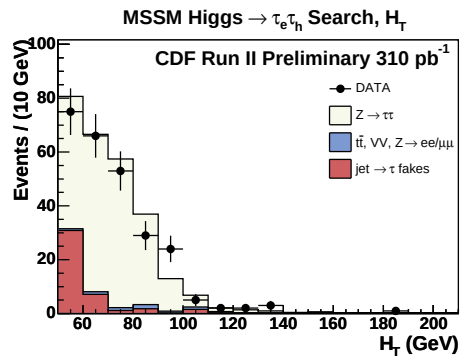


(b) $\tau_e \tau_h$

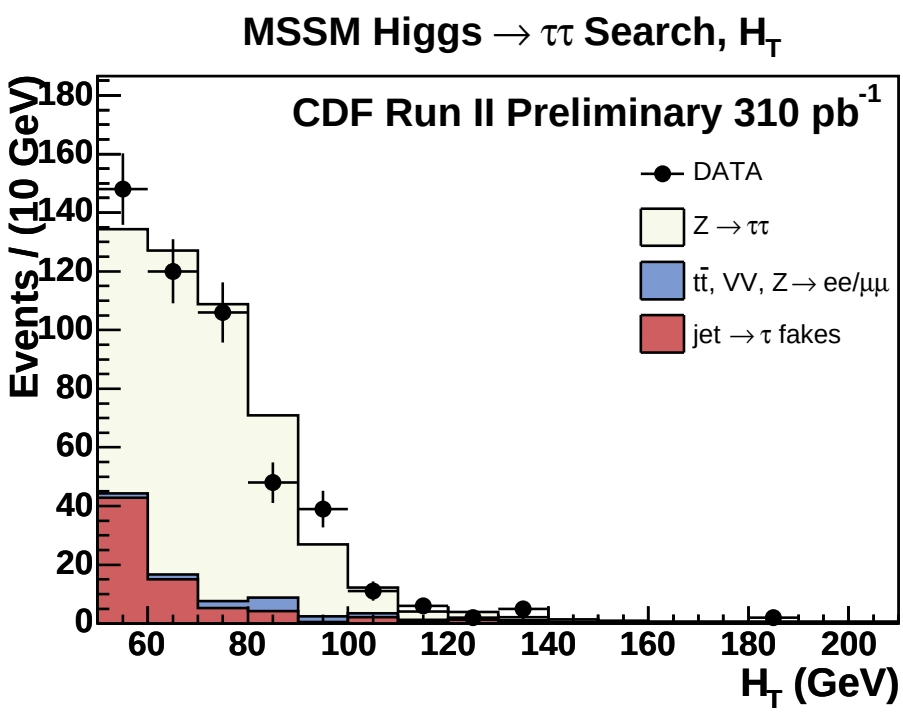


(c) $\tau_\mu \tau_h + \tau_e \tau_h$

Figure 7.8: $\tilde{H}_T$ *in the* $\tau_\mu \tau_h$ *and* $\tau_e \tau_h$ *channels.*

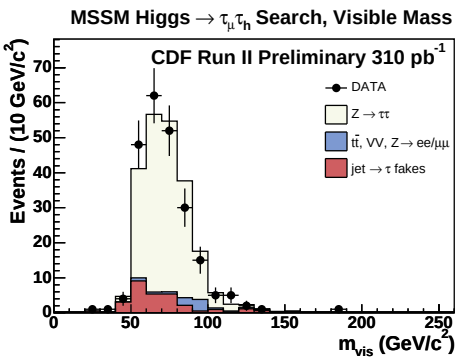


(a) $\tau_\mu\tau_h$

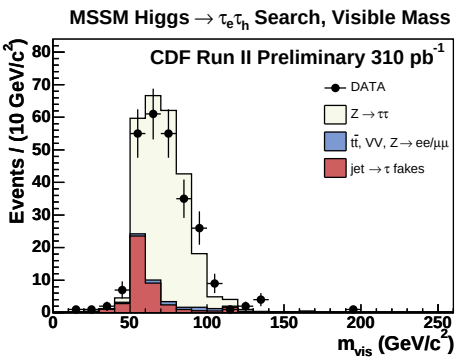


(b) $\tau_e\tau_h$

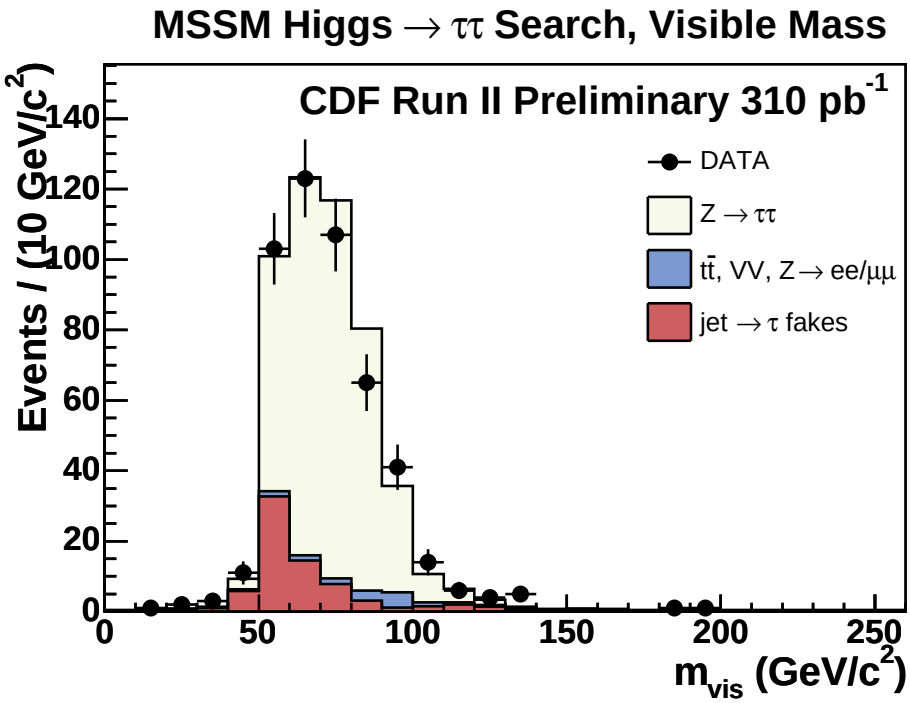


(c) $\tau_\mu\tau_h + \tau_e\tau_h$

Figure 7.9: *$m_{vis}$ in the $\tau_\mu\tau_h$ and $\tau_e\tau_h$ channels.*

| source | $\tau_h\tau_e$ | $\tau_h\tau_\mu^{CMUP}$ | $\tau_h\tau_\mu^{CMX}$ | all muons |
|---|---|---|---|---|
| $Z \to \tau\tau$ | 217.2 ± 3.9 ± 12.7 | 123.2 ± 2.9 ± 8.6 | 64.1 ± 2.1 ± 4.6 | 187.3 ± 3.6 ± 11.9 |
| $Z \to ll$ | 5.9 ± 0.5 ± 0.3 | 4.7 ± 0.6 ± 0.3 | 3.7 ± 0.5 ± 0.3 | 8.4 ± 0.8 ± 0.5 |
| $t\bar{t}, VV$ | 1.0 ± 0.1 ± 0.1 | 0.6 ± 0.1 ± 0.0 | 0.2 ± 0.0 ± 0.0 | 0.9 ± 0.1 ± 0.1 |
| $jet \to \tau$ | 44.6 ± 0.1 ± 8.9 | 17.1 ± 0.1 ± 3.4 | 13.6 ± 0.1 ± 2.7 | 30.8 ± 0.2 ± 6.2 |
| Sum BG | 268.7 ± 3.9 ± 15.5 | 145.7 ± 3.0 ± 9.3 | 81.7 ± 2.2 ± 5.3 | 227.3 ± 3.7 ± 13.4 |
| DATA | 260 | 147 | 80 | 227 |

Table 7.1: *Predicted backgrounds and observed events in the $\tau_e\tau_h$ and $\tau_\mu\tau_h$ after applying all selection cuts.*

| source | $\tau_e\tau_h + \tau_\mu\tau_h$ |
|---|---|
| $Z \to \tau\tau$ | 404.5 ± 5.3 ± 23.2 |
| $Z \to ll$ | 14.3 ± 0.9 ± 0.8 |
| $t\bar{t}, VV$ | 1.9 ± 0.1 ± 0.1 |
| $jet \to \tau$ | 75.4 ± 0.2 ± 15.1 |
| Sum BG | 496.1 ± 5.4 ± 27.7 |
| DATA | 487 |

Table 7.2: *Predicted backgrounds and observed events in $\tau_e\tau_h + \tau_\mu\tau_h$ after applying all selection cuts.*

# Chapter 8

# Results & Interpretations

## 8.1 Results

We wish to determine the observed rate of MSSM Higgs production in our sample, and either measure a cross section or set an upper limit on its value. The presence of neutrinos in the final state, combined with lack of information on the center of mass energy and longitudinal component of the missing energy, does not allow exact mass reconstruction for Higgs bosons (or $Z$'s) decaying to tau pairs. Instead, we use "visible mass" (Figure 8.1)

formed from the visible tau decay products and $\not{E}_T$ in the event. We define a four vector of $\not{E}_T$ as follows.

$$\vec{\not{E}} = (\not{E}_X, \not{E}_Y, 0, \not{E}_T)$$

Once we define a four vector of $\not{E}_T$, then we can calculate a kind of invariant mass of the system which is called $m_{vis}$.

$$m_{vis} = \sqrt{(\sum E_\alpha)^2 \ - \ (\sum \vec{p}_\alpha)^2}$$

where, $\alpha$ stands for two $\tau$ and $\not{E}_T$. This is a mass-like quantity that allows some discrimination between $Z$ and heavier Higgs bosons. It does not peak at the real mass of the particle and is used only as a discrimination variable.

With increasing mass the separation between Higgs and $Z$ improves (although at a slower rate). Detection efficiency also improves with mass. These factors work in favor of setting better limits for heavier Higgs bosons, however, the production cross sections are expected to be lower. The width of $m_{vis}$ is much larger than the mass-width of the

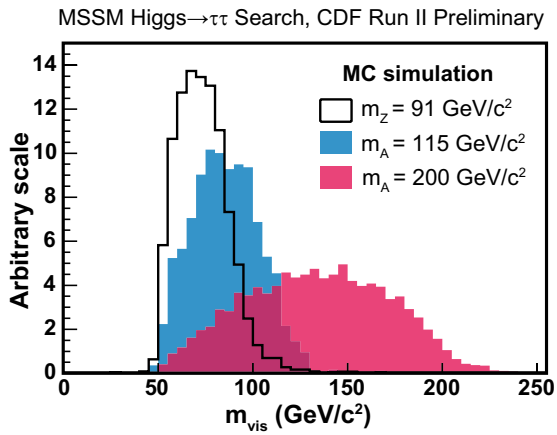


Figure 8.1: *Visible mass distributions for Z and Higgs bosons (normalized to the same area).*

Higgs bosons, even at large $\tan\beta$. Figure 8.2 shows the acceptance for $\phi \to \tau\tau$.

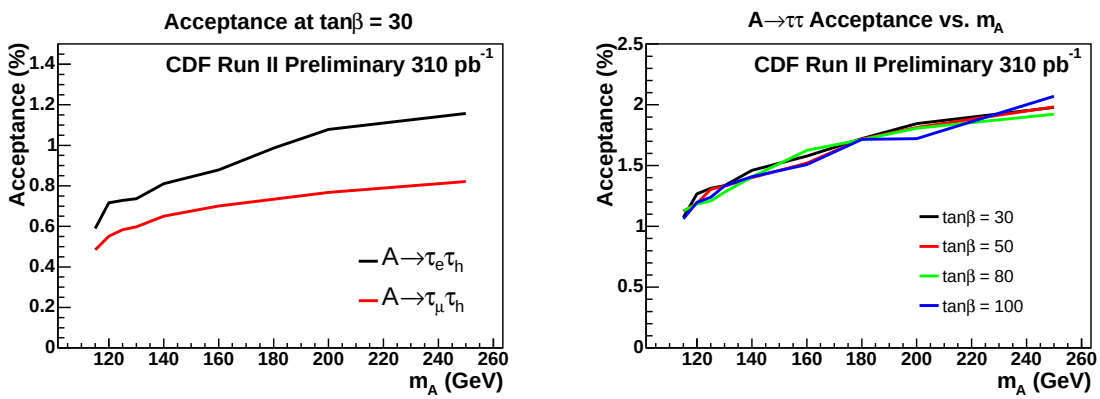


(a) Acceptance for $\tau_e\tau_h$ and $\tau_\mu\tau_h$, $\tan\beta = 30$

(b) Acceptance for $\tau_e\tau_h + \tau_\mu\tau_h$

Figure 8.2: *Acceptance for $\phi \to \tau\tau$*

### 8.1.1 Likelihood

We employ a binned likelihood method using the visible mass distribution. We combine all channels in the final distribution. Then, if we observe $n_i$ events in each bin $i$ of $m_{vis}$, and we expect $\mu_i$ events from signal and background sources, we can write the likelihood as the product of the individual bin Poisson probabilities:

$$\mathcal{L} = \prod_i \frac{\mu_i^{n_i} e^{-\mu_i}}{n_i!} \tag{8.1}$$

The number expected in each bin is given by the sum over various sources, indexed by $j$:

$$\mu_i = \sum_j L_j \sigma_j \epsilon_{ji} \tag{8.2}$$

where $L_j$ is the integrated luminosity, $\sigma_j$ is the cross section, and $\epsilon_{ji}$ is the efficiency for source $j$. Sources include the Higgs signal, Drell-Yan backgrounds, QCD fake background, etc.

### 8.1.2 Treatment of Systematic Errors

The quantity in which we are interested is in fact the cross section for the signal, which we can take to be $\sigma_1$ for example. All other parameters in the likelihood are treated as nuisance parameters, and to the extent that they are unknown they represent systematic errors present in the analysis.

We deal with the uncertainties on these parameters by introducing Gaussian constraints into the likelihood. For example, if we let $\sigma_2$ represent the cross section of, say, $Z \to \tau\tau$ production, and we believe its value is $\sigma_2 = 254 \pm 5.4$ pb, we write the likelihood as

$$\mathcal{L} = \prod_i \frac{\mu_i^{n_i} e^{-\mu_i}}{n_i!} \times G(\sigma_2, \tilde{\sigma}_2, \Delta\sigma_2)$$

where G is a Gaussian function with mean $\tilde{\sigma}_2 = 254$ pb and width $\Delta\sigma_2 = 5.4$ pb.

Then the question arises as to how to treat the Gaussian constraints. There are two main methods used commonly in CDF: marginalization and profiling. In marginalization one simply integrates the likelihood with respect to the nuisance parameter:

$$\mathcal{L} = \int_0^\infty \prod_i \frac{\mu_i^{n_i} e^{-\mu_i}}{n_i!} \times G(\sigma_2, \tilde{\sigma}_2, \Delta\sigma_2) d\sigma_2$$

Often one refers to this as "smearing the likelihood". This calculation is best performed by Monte Carlo integration when there are many such parameters and the integral becomes multidimensional.

In profiling, one simply maximizes the likelihood with respect to the nuisance parameters. This is typically what is done when one is making a measurement (as opposed

to setting a limit). One usually minimizes $-\ln\mathcal{L}$ using MINUIT or some other function minimization package; these are very efficient and rapid to use.

We choose the profiling method here. Studies have indicated that for complex problems such as a binned likelihood fit, the two approaches give indistinguishable results. [24]

There are additional parameters that encode systematic errors other than the appearing in the equations above. Most enter as multiplicative factors; for example the data/MC scale factors for lepton and tau ID multiply the appropriate terms in the $\mu_I$. Other factors lead to a net "smearing" of the signal cross section and are treated by an overall additive term applied to the signal cross section.

The techniques described here only work in the case where the errors are reasonably small, less than about 20% [25]. For larger errors the Gaussian terms tend to cause the likelihood to reach an asymptotic minimum at some value as the signal cross section increases. This means that the integral of the likelihood diverges, and one cannot set a limit using the usual Bayesian method of finding the cross section beyond which 5% of the likelihood integral lies.

The uncertainties in the Higgs cross section resulting from uncertainties in data/MC energy scale are accounted for by an additive parameter subject to a constraint. We generate shifted $m_{vis}$ templates and study the effect on hypothetical Higgs cross-sections. The shifted templates are produced with energy scales of particles used in $m_{vis}$ calculations varied by $1\sigma$. Figure 8.3 shows an example of the average deviation in the observed cross section as a function of the "true" Higgs cross section, as estimated from these pseudo-experiments. The largest shift obtained from these comparisons is used to assign uncertainty due to the energy scale.

Once this uncertainty is determined, we have to decide on the type of constraint that should be applied. The question is whether a Gaussian truly represents what we believe about this uncertainty. The choice of the worst combination of energy scale uncertainties used to determine the uncertainty represents more of an upper limit on the possible shift, as opposed to a $1\sigma$ Gaussian uncertainty. Previously we used a

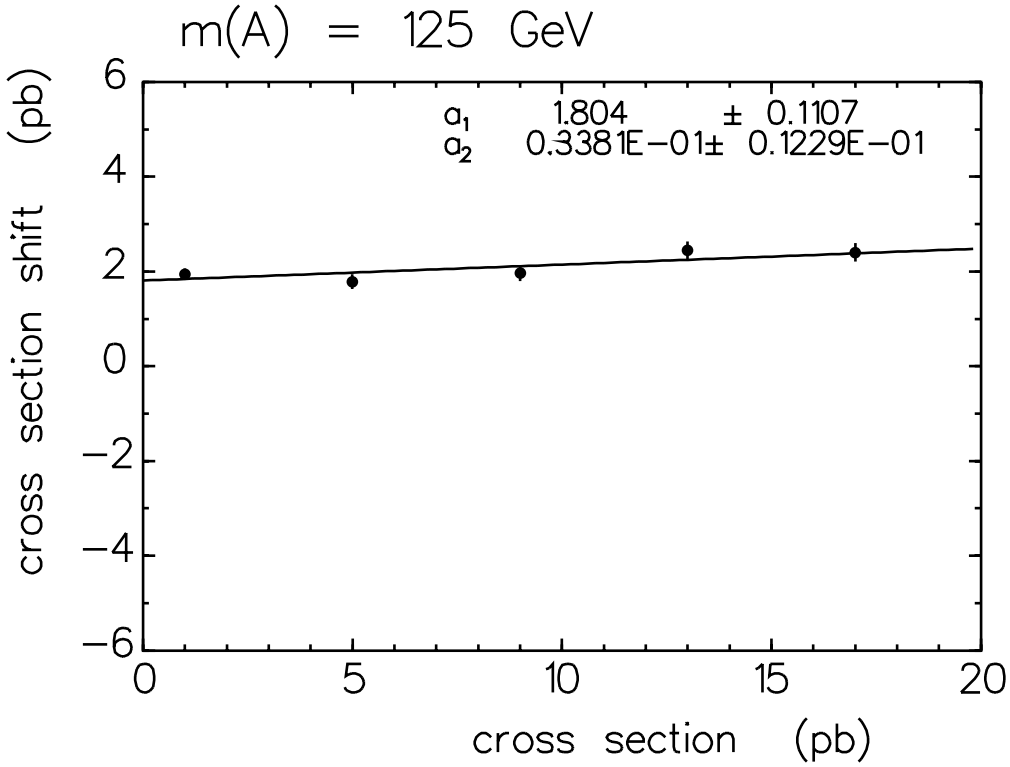


Figure 8.3: *Average shift in apparent Higgs cross section due to shifted templates, as a function of true Higgs cross section. This is the shift for a Higgs mass of 125 GeV/$c^2$ and shows that energy scale mismatches between data and MC could lead to a shift of 2 pb in the measured cross section. So if a 10 pb Higgs with mass 125 GeV/$c^2$ existed in our data, energy scale mismatches could cause us to measure a 12 pb cross section.*

quartic constraint of the form

$$Q(\Delta\alpha) = \frac{e^{(-2\Delta\alpha^4/\sigma_\alpha^4)}}{\sigma_\alpha} \tag{8.3}$$

Here $\Delta\alpha$ represents the deviation in the additive parameter from zero. This function has a flatter shape in the central region, and cuts off rapidly beyond $\Delta\alpha = \sigma_\alpha$. In general, and in our case in particular, this type of constraint gives better expected limits. In this analysis we sacrificed some sensitivity in favor of using a Gaussian constraint that seems to be better received by our colleagues.

### 8.1.3 Upper Limits on Higgs Cross section

We estimated the sensitivity of the analysis for luminosity 310 $pb^{-1}$ ($\tau_e\tau_h + \tau_\mu\tau_h$ channels) by performing pseudo-experiments for each Higgs mass point (assuming no Higgs events in the pseudo-data) and taking into account all systematic errors.

We perform the limit-setting procedure using the real data for each of the hypothetical Higgs mass points. An example fit is shown in Figure 8.4. We see no evidence of a signal and calculate 95% CL upper limits $\sigma(p\bar{p} \to \phi) \times \mathcal{B}(\phi \to \tau\tau)$.

Figure 8.5 shows a plot of the limits versus Higgs mass, together with the predicted limits from the pseudo-experiments. For closer inspection, these results are also tabulated in Table 8.1.

## 8.2 Interpretation of the Limits

We use our observed limits @95% CL on $\sigma(p\bar{p} \to \phi) \times \mathcal{B}(\phi \to \tau\tau)$ to exclude regions in the $\tan\beta$ *vs* $m_A$ plane, where $\tan\beta$ is the ratio of the vacuum expectation values for the Higgs fields that couples to the up- and down-type fermions; $m_A$ is the mass of the $CP$-odd neutral Higgs boson.

The MSSM parameter space is quite large. For the interpretation, we take two benchmarks [26] that have become the standard in the field - the $m_h^{\max}$ and the no-mixing scenarios.

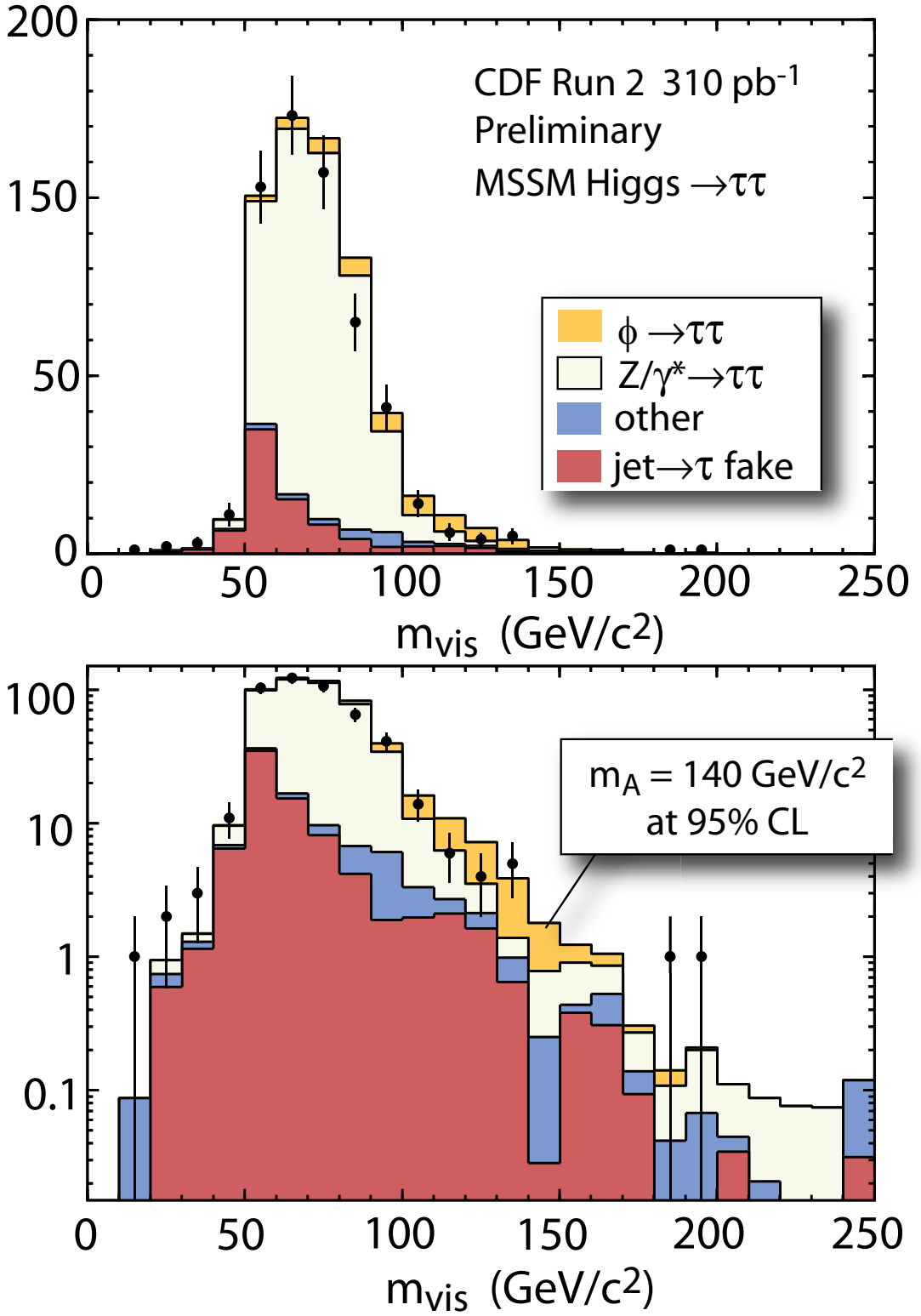


Figure 8.4: *Example fit for $m_A$=140 GeV. Signal and all background contributions are set to levels corresponding to the 95% CL upper limit.*

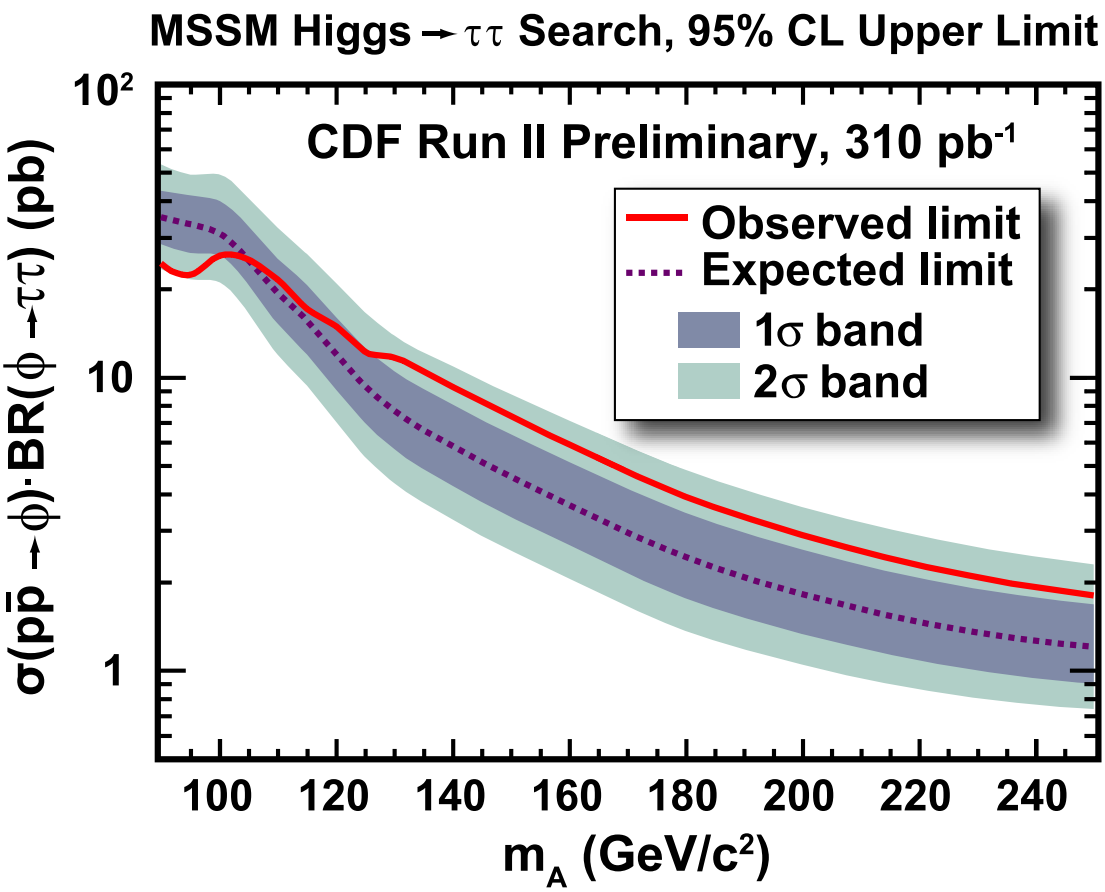


Figure 8.5: *Expected and observed limits for neutral MSSM Higgs production.*

| | limit(pb) | |
|---|---|---|
| $m_A$ (GeV) | expected | observed |
| 90 | 35.06 | 24.40 |
| 95 | 32.56 | 22.20 |
| 100 | 31.73 | 25.90 |
| 110 | 19.36 | 21.58 |
| 115 | 15.36 | 17.13 |
| 120 | 11.93 | 14.86 |
| 125 | 9.29 | 12.26 |
| 130 | 7.66 | 11.64 |
| 140 | 5.78 | 9.27 |
| 160 | 3.67 | 5.85 |
| 180 | 2.44 | 3.91 |
| 200 | 1.84 | 2.91 |
| 250 | 1.19 | 1.80 |

Table 8.1: *Upper limits at 95% CL on MSSM Higgs cross section times branching ratio to tau pairs as a function of Higgs mass.*

The $m_h^{\max}$ scenario has parameters chosen such that the maximum possible Higgs mass as a function of $\tan\beta$ is obtained. The no-mixing scenarios additionally assumes no mixing in the stop-squark sector. The common SUSY parameters for these benchmarks are Higgs mixing parameter $\mu = +0.2$ TeV, $SU(2)$ gaugino mass parameter $M_2$=0.2 TeV. The difference is in the choice of the SUSY mass scale $M_{SUSY}$, the squark mixing parameter $X_t$, and gluino mass $m_{\tilde{g}}$. For $m_h^{max}$, $M_{SUSY}$=1 TeV, $X_t^{\overline{MS}} = \sqrt{6}M_{SUSY}$. The corresponding values for no-mixing are $M_{SUSY}$=2 TeV and $X_t = 0$. In both cases $m_{\tilde{g}} = 0.8M_{SUSY}$. In all calculations we used top quark mass $m_t$=178.0 GeV/c$^2$ (using $m_t$=174.0 GeV/c$^2$ has negligible effect on the results).

As discussed in Chapter 1, the MSSM neutral Higgs sector has three bosons, the pseudo-scalar $A$, and the scalar $h$ and $H$. One of the scalars (either $h$ or $H$) is nearly degenerate in mass and production cross-section with the $A$. For a given value of $\tan\beta$ in a given scenario, there is a "crossover mass" below which the $h$ shadows the $A$ and above which it is the $H$. In the $m_h^{\max}$ scenario the crossover point is at m=130 GeV.

**Production Cross-section Calculations**

There are two production modes that are relevant for our search. Gluon fusion, $gg \to \phi$, and $b\bar{b}$ annihilation, $b\bar{b} \to \phi$, where $\phi$ is $A, H, h$. For the former we use the HIGLU program by M. Spira [28]. A somewhat dated manual can be found at hep-ph/9510347. This program (recently upgraded to use CTEQ6 PDFs) calculates the NLO cross-sections for $gg \to A, H, h$. The various MSSM parameters such as $\tan\beta$, $\mu$, M-SUSY, and the stop and sbottom tri-linear couplings are taken as input parameters. We ran HIGLU for both MSSM scenarios and tabulated the results.

The full MSSM production cross-sections for $b\bar{b} \to \phi$ has not been calculated. However, this process has been calculated to NLO and NNLO for the Standard Model Higgs [27]. From the calculated cross sections for $b\bar{b} \to \phi$ in the Standard Model, we could naively apply a factor of $\tan^2\beta$ [1]. However, this would not take into account radiative

[1] Scott Willenbrock, private communication

| | $b\bar{b}$ | | $gg$ | |
|---|---|---|---|---|
| $m_A$ | $A$ | $H/h$ | $A$ | $h/H$ |
| 100 | 76.8 | 75.8 | 74.1 | 73.1 |
| 120 | 34.5 | 34.3 | 24.5 | 24.4 |
| 140 | 16.7 | 16.4 | 9.3 | 9.2 |
| 180 | 4.6 | 4.6 | 1.8 | 1.8 |
| 200 | 2.6 | 2.6 | 0.9 | 0.9 |

Table 8.2: *Production cross-sections (pb) for $b\bar{b} \to \phi$ and $gg \to \phi$ (no mixing scenario, $\tan\beta = 60$).*

effects [2].

To do this properly we use the FeynHiggs program by S. Heinemeyer [29]. This program takes MSSM parameters as input and outputs the cross sections and branching ratios for the SM and MSSM Higgses. We take the ratio $\Gamma^{\rm MSSM}_{\phi\to bb}/\Gamma^{\rm SM}_{\phi\to bb}$ and multiply the SM production cross section of Kilgore et el. to get the $b\bar{b} \to \phi$ production cross section in the MSSM. Here $\Gamma^{\rm MSSM}_{\phi\to bb}$, $\Gamma^{\rm SM}_{\phi\to bb}$ are the partial widths of $\phi \to b\bar{b}$ in MSSM and SM calculated by FeynHiggs. The $\Delta m_b$ correction to $\tan\beta$ changes the coupling of the Higgs to b, and therefore to $\tau$ as well. We cannot ignore the effect of $\Delta m_b$ on the branching ratio, since as the coupling of the Higgs to b goes down (up), the corresponding coupling to $\tau$ goes up (down). Therefore, we use the values of Higgs to $\tau\tau$ branching ratio output by the FeynHiggs program. We show some values for the $m_h^{\rm max}$ case, $\tan\beta = 60$ in Table 8.2.

**Excluded region in** $\tan\beta$ *vs* $m_A$

Figure 8.6 shows the excluded parameter region in the $\tan\beta$ *vs* $m_A$ plane, along with the results from LEP 2. The D0 Collaboration has set limits for MSSM Higgs production in association with one (or two) $b$-quarks and subsequent Higgs decay to $b\bar{b}$ [30]. It is interesting to note that their observed limits are about $1\sigma$ lower than the expected, while in our case the observed limits are higher. We do not have enough information on

[2] Marcela Carena, Sven Heinemeyer private communication

the D0 result to make a strict comparison of the expected $\tan\beta$ limits for various masses. The comparison is further complicated by their choice of $\mu = -0.2$ TeV, contrary to the suggested benchmark scenarios for hadron colliders discussed above. There is a speculation by theorists that choosing $\mu = +0.2$ TeV will significantly weaken $\tan\beta$ exclusion from $p\bar{p} \to \phi b(b) \to b\bar{b}b(b)$ [3]. The LEP 2 limits have weak dependence on the choice of the sign of $\mu$ [4].

**PDF Uncertainties**

The effects of PDF uncertainties on the $b\bar{b} \to \phi$ cross section have been studied by Alexander Belyaev [31]. These results have not been published yet and are not taken into account in the $\tan\beta$ exclusion plots (however, the effect of PDF uncertainties on the acceptance has been incorporated in the limits on $\sigma(p\bar{p} \to \phi) \times \mathcal{B}(\phi \to \tau\tau)$). We are investigating the net effect of the PDF uncertainties and the initial results indicate that there is a negative correlation between the production cross section and signal acceptance.

## 8.3 Conclusions

In the technical aspect, we have achieved the deep understanding of the tau particle response in the CDF detector. This includes several sophisticated tau selections and better energy measurement using $\pi^0$. Also we took a lot of effort to understand QCD background from the source of $jet \to \tau$ misidentification and we established the excellent method to estimate it. This requires understanding on triggers and jet behavior in the CDF detector.

In terms of physics, this analysis proves that the ditau decay channel is very competitive to the $b\bar{b}$ channel which is known as the golden channel in MSSM Higgs searches. Unlike the $b\bar{b}$ channel, the ditau channel also allows us to have sensitivity in the $\mu > 0$ case. It is an additional benefit of this channel. If we consider that one of the main

[3] See Georg Weiglein's talk at the CDF meeting in Barcelona on May 31, 2005.

[4] Tom Junk, private communication. Official updated LEP 2 limits are expected at the end of Summer '05.

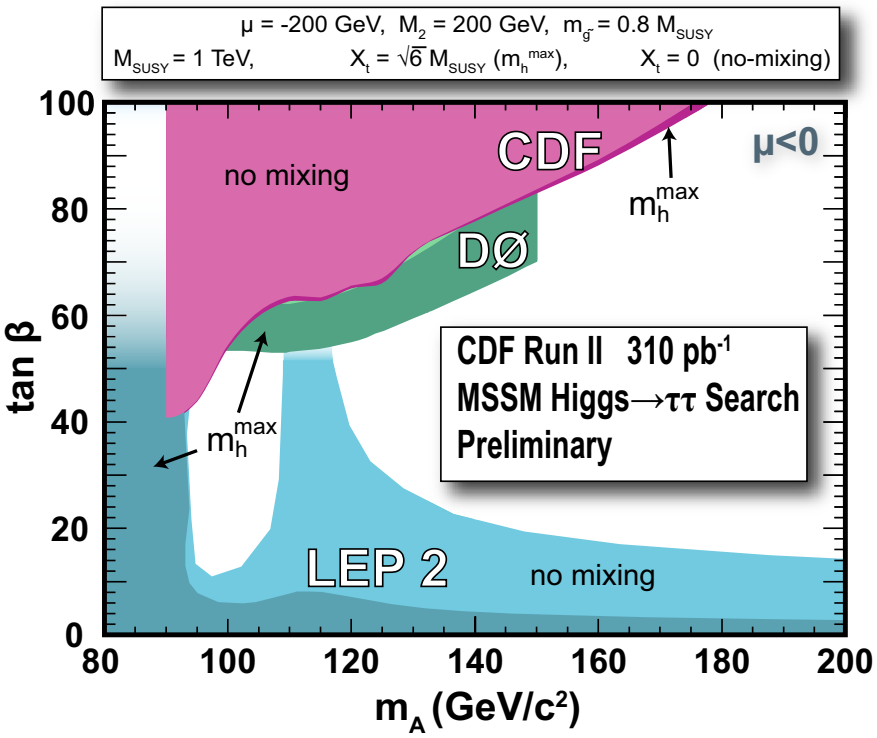


(a) negative $\mu$

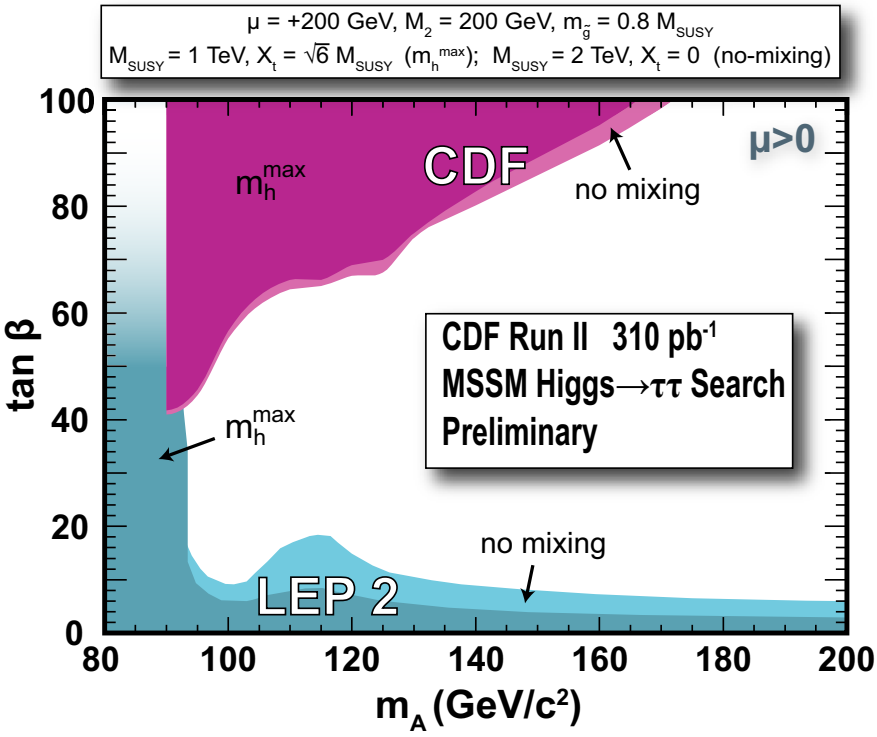


(b) positive $\mu$

Figure 8.6: $\tan\beta$ *vs* $m_A$ *exclusion contours for the no-mixing and* $m_h^{max}$ *scenarios with negative* $\mu$ *(a) and positive* $\mu$ *(b).*

physics goals in Run II is to explore the Higgs and exotic particles beyond the Standard Model. this analysis (the searches for neutral MSSM Higgs bosons in the di-$\tau$ decay channel) produces successful satisfaction. The current results from this analysis exclude $\tan\beta \sim 60$ at $m_A$=120 GeV/c$^2$ for the $m_h^{max}$ and no-mixing benchmark scenarios. This excludes significant area in the $\tan\beta$ vs. $m_A$ parameter space and will guide the future studies of MSSM Higgs searches at LHC. The results are statistics limited and will benefit from larger data samples and the addition of the $\tau_e\tau_\mu$ and $\tau_h\tau_h$ detection channels.

# Appendix A

# Glossary

**CDF:** Collider Detector at Fermilab

**CEM:** Central ElectroMagnetic calorimeter

**CES:** Central Electromagnetic Showermax detector

**CHA:** Central HAdronic calorimeter

**CLC:** Cherenkov Luminosity Counter

**CMU:** Central MUon detector

**CMUP:** CMU + CMP

**CMP:** Central Muon uPgrade detector

**CMX:** Central Muon eXtension detector

**CPR:** Central Preshower Radiate detector

**CSP:** Central Scintillation counter uPgrade

**CSX:** Central Scintillation counter eXtension

**DAQ:** Data Acquisition

**fiducial region:** detectable region at CDF. Most of cases, it refers the region with $|\eta| < 1$

**HEP:** High Energy Physics

**L1:** Level 1 trigger. Hardware. Reduction rate is from 2.5 MHz to 20 kHz or less.

**L2:** Level 2 trigger. Hardware. Reduction rate is 300 Hz or less.

**L3:** Level 3 trigger. Software. Reduction rate is 75Hz or less.

**LEP:** the Large Electron Positron collider at CERN.

**Lepton+Track:** The combination of electron + track trigger and muon + track trigger

**MIP:** Minimum Ionizing Particle

**MSSM:** Minimal Supersymmetric Standard Model

**PDF:** Parton Distribution Function

**PEM:** Plug ElectroMagnetic calorimeter

**PES:** Plug Electromagnetic Showermax detector

**PHA:** Plug HAdronic calorimeter

**SM:** Standard Model

**SUSY:** Supersymmetry model

**TAU+MET:** tau + missing $E_T$ trigger that requires at least one tau and 20 GeV missing $E_T$

**Tevatron:** proton-antiproton accelerator at Fermi National Accelerator Laboratory

**VEV:** vacuum expectation value

**WHA:** endWall HAdronic calorimeter

# References


[1] S. Weinberg, Phys. Rev. Lett. **19**, 1264 (1967); S. Weinberg, Phys. Rev. **D5**, 1412 (1972); A. Salam, in *Nobel Symposium No. 8*, ed. N. Svartholm (Almqvist and Wiksell, Stockholm, 1968); S.L. Glashow, Nucl. Phys. **22**, 579 (1961); D.J. Gross and F. Wilczek, Phys. Rev. **D8**, 3633 (1973); D.J. Gross and F. Wilczek, Phys. Rev. **D9**, 980 (1974); H.D. Politzer, Phys. Rept. **14**, 129 (1974).

[2] B.W.Lee, C.Quigg, and H. Thacker. Phys.Rev.D, 16:1519, 1977.

[3] Report of the Tevatron Run 2 Higgs Working Group, hep-ph/0010338.

[4] A Supersymmetry Primer, hep-ph/9709356, Stephen P. Martin, April, 1999

[5] A. Connolly, CDF note 6806.

[6] A. Anastassov *et al.*, "Search for Neutral MSSM Higgs Boson(s) in the tau tau Decay Channel", CDF7027 (2004)

[7] F. Abe *et al.*, The CDF detector: an overview, Nucl.Instrum.Meth.A271:387-403, 1988

[8] The CDF IIb Collaboration, The CDF IIb Detector technical design report, September 2002

[9] S. Baroiant *et al.* "Update on the Lepton+Track Trigger in Run II - Definition and Physics Goals", CDF6325 (2003).

[10] CDF Good Run List group : http://www-cdf.fnal.gov/internal/dqm/goodrun/good.html

[11] M. Coca, E. Halkiadakis " Central Electron Identification Efficiencies for the 200 $pb^{-1}$ Run2 Dataset", CDF6580 (2004).

[12] V. Martin, L. Cerrito "Muon Cuts and Efficiencies for 4.11 Analyses", CDF6825 (2004).

[13] Physics Letters B, Review of Particle Physics, 2004. (Known as "Particle Data Book")

[14] Anton Anastassov *et al.* "Tau Reconstruction Efficiency and QCD Fake Rate for Run 2", CDF6308 (2003).

[15] Zongru Wan, A Search for New Physics with High Mass Tau Pairs in Proton–Antiproton Collisions at $\sqrt{s} = 1.96$ TeV at CDF, 2005

[16] Leslie Stevan Groer, A Search for Charged Higgs Boson Decays of the Top Quark using Hadronic Decays of the Tau Lepton in Proton-Antiproton Collisions a $\sqrt{s}$ = 1.8 TeV at CDF, 1998

[17] S. Baroiant *et al.* "Energy Measurement for Hadronic Taus", CDF6654 (2003)

[18] Anton Anastassov, "Non-isolated $\pi^0/\gamma$ Reconstruction", CDF6688 (2003).

[19] Colin Jessop, "A Search for the Top Quark Decaying to the Charged Higgs Boson in $p\bar{p}$ Collisions at $\sqrt{s} = 1.8$ TeV", PhD Thesis, Harvard University (1993).

[20] J. Conway *et al.*, "Tau Identification", CDF3545 (1997).

[21] http://www-cdf.fnal.gov/internal/physics/exotic/tau/

[22] S. Baroiant *et al.* "$Z^0 \to \tau\tau$ Cross-Section Measurement", CDF6552 (2004).

[23] Pasha Murat, Talk given at the Simulation Meeting on July 31, 2003.

[24] See John Conway's presentation from the February 2004 CDF Statistics Meeting, available on request.

[25] Private communication from Statistics Committee.

[26] M. Carena, S. Heinemeyer, C.E.M. Wagner, and G. Weiglein "Suggestions for Benchamark Scenarios for MSSM Higgs Boson Searches at Hadron Colliders", hep-ph/0202167 (2002).

[27] F. Maltoni, Z. Sullivan, S. Willenbrock, "Higgs-Boson Production via Bottom-Quark Fusion", hep-ph/0301033 (2003).

R.V. Harlander, W.B. Kilgore, "Higgs boson production via bottom quark fusion in next-to-next-to-leading order", hep-ph/0304035 (2003).

[28] M.Spira, http://people.web.psi.ch/spira/higlu

[29] http://www.feynhiggs.de contains all code and references

[30] The D0 Collaboration, "Search for neutral supersymmetric Higgs bosons in multijet events at $\sqrt{s} = 1.96$ TeV, hep-ex/0504018 (2005).

[31] Alexander Belyaev, Talk at DIS'05, (2005).

[32] S. Baroiant *et al.*, Measurement of Tau ID Efficiencies for the First $72pb^{-1}$ of Run II Data, CDF7013 (2004).

# Curriculum Vita

**Dongwook Jang**

| | |
|---|---|
| **1989-1996** | B.S. in Physics,<br>Yonsei University, Seoul, Republic of Korea |
| **1996-1998** | M.S. in Physics,<br>Yonsei University, Seoul, Republic of Korea |
| **1996-1998** | Teaching Assistant, Physics Department<br>Yonsei University, Seoul, Republic of Korea |
| **1999-2006** | Ph.D. in Physics,<br>Rutgers, the State University of New Jersey,<br>New Brunswick, New Jersey, USA |
| **1999-2000** | Teaching Assistant, Department of Physics & Astronomy,<br>Rutgers, the State University of New Jersey,<br>New Brunswick, New Jersey, USA |
| **2000-2006** | Research Assistant, Department of Physics & Astronomy,<br>Rutgers, the State University of New Jersey,<br>New Brunswick, New Jersey, USA |